

PROCESS MONITORING FOR TEMPORAL-SPATIAL
MODELING OF LASER POWDER BED FUSION (L-PBF) BASED
METAL ADDITIVE MANUFACTURING

By

ANIMEK SHAURYA

A thesis submitted to the

School of Graduate Studies

Rutgers, The State University of New Jersey

In partial fulfillment of the requirements

For the degree of

Master of Science

Graduate Program in Industrial and Systems Engineering

Written under the direction of

Tuğrul Özel

And approved by

New Brunswick, New Jersey

May 2018

ABSTRACT OF THE THESIS

PROCESS MONITORING FOR TEMPORAL-SPATIAL

MODELING OF LASER POWDER BED FUSION (L-PBF) BASED

METAL ADDITIVE MANUFACTURING

by ANIMEK SHAURYA

Thesis Director:

Dr. Tuğrul Özel

Laser powder bed fusion (L-PBF) is an additive manufacturing process which can produce nearly fully dense parts with complex geometry by using laser power which follows layer-to-layer scanning strategies on powder material with pre-specified powder layer thickness. In L-PBF, the powder material is fully melted and then solidified to achieve the above target. It offers high flexibility in manufacturing complex shapes reducing high tooling cost with its simple and quick setup and providing wide range of high strength alloys to work with. The parts fabricated through L-PBF are widely used for industrial applications such as in automobile, aerospace and medical industries. Various process parameters and scan strategies affect the build quality and structural integrity of the finished parts. In-process data analytics and statistical monitoring techniques are required to detect

melt pool area, localize material spatter and control the process. High speed video imaging provides some process insight for identifying melt pool and spatter and can be integrated into process monitoring and control for L-PBF advanced manufacturing process.

In this thesis, we studied the use of high speed camera videos for in-situ monitoring of L-PBF of nickel alloy 625 to detect melt pool, spatter, and over melting regions to improve the process control capability. The quantities that can be measured via in-situ sensing can be referred to as process signatures and can represent the source of information to detect possible defects. The video images are processed for temporal-spatial analysis by using principal component analysis and T^2 statistics for identifying the history of pixel intensity levels through the process monitoring. These results are correlated as over melting and spatter regions. The results obtained from these studies will provide information about the process parameters which can be used for further validation of modelling studies or for industrial purposes.

TABLE OF CONTENTS

ABSTRACT.....	ii
TABLE OF CONTENTS	iv
LIST OF TABLES	vii
LIST OF FIGURES	viii
CHAPTER 1 INTRODUCTION	1
1.1 Metal Additive Manufacturing.....	4
1.2 Rationale and Motivation	8
1.3 Research Objectives.....	9
CHAPTER 2 LASER POWDER BED FUSION PROCESS	10
2.1 L-PBF Process Parameters	10
2.1.1 Laser Power.....	11
2.1.2 Scan Strategy	11
2.1.3 Scan Velocity	14
2.1.4 Hatch Distance	14
2.1.5 Powder Bed	15
2.2 L-PBF Process signatures	16
2.2.1 Meltpool Geometry	16
2.2.2 Meltpool Shape Analysis	17
2.2.3 Material Spatter	19
CHAPTER 3 MATERIAL AND EXPERIMENTAL SETUP.....	20
3.1 Material	20
3.2 Experimental Setup	20
3.3 In-situ Process Monitoring	23

CHAPTER 4	STATISTICAL PROCESS MONITORING OF L-PBF PROCESS	25
4.1	Statistical monitoring of product attributes	27
4.2	Statistical Monitoring of Process Signatures.....	27
4.3	High Speed Camera Videos	28
4.3.1	Frames per Second (FPS).....	29
4.3.2	Image Resolution.....	29
4.3.3	Integration Time.....	30
CHAPTER 5	METHODOLOGY	31
5.1	Image Types	32
5.1.1	Binary Image.....	32
5.1.2	Grayscale Image.....	33
5.1.3	True Color Image.....	33
CHAPTER 6	TEMPORAL AND SPATIAL ANALYSIS OF IMAGE STREAMS	34
6.1	Temporal Principal Component Analysis	34
6.1.1	Process Flow for Temporal Principal Component Analysis	36
6.1.2	Additional Processing	38
6.2	Spatial Principal Component Analysis	41
6.3	Spatial Mapping	42
CHAPTER 7	RESULTS.....	43
7.1	Temporal Principal Component Analysis	43
7.2	Meltpool Area Analysis	53
7.3	Spatial Principal Component Analysis	70
CHAPTER 8	CONCLUSIONS AND FUTURE SCOPE.....	78
8.1	Conclusion.....	78

8.2	Future Scope	79
APPENDIX.....		81
REFERENCES.....		87

LIST OF TABLES

Table 1	Chemical composition of nickel alloy 625	20
Table 2	Parameters of high-speed camera.....	23
Table 3	Parameters of the high-speed camera videos	28

LIST OF FIGURES

Figure 1	The laser powder bed fusion system by EOS GmbH.....	2
Figure 2	Additively fabricated metal parts (a) Hip socket made on Arcam PBF machine, (b) Dental crowns and bridges on EOS PBF machine.....	3
Figure 3	Technology readiness levels of additive manufacturing applications.....	4
Figure 4	Classification of additive manufacturing technologies. Source: ASTM International Committee F42 on Additive Manufacturing Technologies.....	5
Figure 5	L-PBF terminology (Criaes et al. 2017).....	11
Figure 6	Schematics of stripes and hatching pattern. Source: insidemetaladditivemanufacturing.com.....	12
Figure 7	Schematics chessboard scanning and hatching patterns. Source: insidemetaladditivemanufacturing.com.....	13
Figure 8	Schematics of islands and other hatching patterns. Source: insidemetaladditivemanufacturing.com.....	13
Figure 9	Views of surfaces generated with L-PBF process in nickel alloy IN625 (P=195 W, vs=800 mm/s, h=0.1 mm). (a) XY top view (b) YZ side view (Criaes et al. 2017).....	16
Figure 10	Definition of Type-I and Type-II meltpools (Criaes et al. 2017)	17
Figure 11	Meltpool shape definition (Criaes et al. 2017).....	18
Figure 12	Melt pool dynamic model (Khairallah & Anderson 2014)	19
Figure 13	(a) Build platform layout, (b) Image of a built cube (Özel et al. 2017).....	21
Figure 14	Schematic of a stripe scan pattern with 90° (left) and 67° (right) CCW rotation between consecutively built layers (Özel et al. 2017)	22
Figure 15	High speed camera set-up: (a) Side-view of the L-PBF machine, custom door, and high-speed camera,	

	(b) CAD solid model of L-PBF machine build chamber and custom viewport, (c) optical axis, plane of focus and vertical iFoV projected on the build plane. (Criales et al. 2017).	24
Figure 16	Representation of video frames in time and pixel space (Repossini et al. 2017).....	30
Figure 17	Statistical analysis methodology for temporal PCA.....	34
Figure 18	Representation of temporal PCA	35
Figure 19	Statistical analysis methodology for spatial PCA	42
Figure 20	The run sequence plot obtained from temporal PCA.....	44
Figure 21	The run sequence plot obtained from temporal PCA.....	44
Figure 22	The run sequence plot obtained from temporal PCA for Type-I and Type-II tracks.....	45
Figure 23	Statistical analysis of Type-I tracks.....	46
Figure 24	Statistical analysis of Type-II tracks.....	47
Figure 25	The run sequence plot obtained from temporal PCA.	48
Figure 26	The run sequence plot obtained from temporal PCA.....	49
Figure 27	The run sequence plot obtained from temporal PCA for Type-I and Type-II tracks.....	49
Figure 28	Statistical analysis of Type-I tracks.....	50
Figure 29	Statistical analysis of Type-II tracks.....	50
Figure 30	The run sequence plot obtained from temporal PCA.....	51
Figure 31	The run sequence plot obtained from temporal PCA.....	51
Figure 32	The run sequence plot obtained from temporal PCA for Type-I and Type-II tracks.....	52
Figure 33	Statistical analysis of Type-I tracks.....	52
Figure 34	Statistical analysis of Type-II tracks.....	53

Figure 35	Comparison of Case 1 when RGB images were converted to gray images and BW images	54
Figure 36	Statistical analysis of Meltpool area in terms of # of pixels of Type-I Track 3.....	55
Figure 37	Statistical analysis of Meltpool area in terms of # of pixels of Type-I Track 5.....	55
Figure 38	Statistical analysis of Meltpool area in terms of # of pixels of Type-I Track 7.....	56
Figure 39	Statistical analysis of Meltpool area in terms of # of pixels of Type-I Track 9.....	56
Figure 40	Statistical analysis of Meltpool area in terms of # of pixels of Type-II Track 2.....	57
Figure 41	Statistical analysis of Meltpool area in terms of # of pixels of Type-II Track 4.....	57
Figure 42	Statistical analysis of Meltpool area in terms of # of pixels of Type-II Track 6.....	58
Figure 43	Statistical analysis of Meltpool area in terms of # of pixels of Type-II Track 8.....	58
Figure 44	Statistical analysis of Meltpool area in terms of # of pixels when frames having laser off time included	59
Figure 45	Statistical analysis of Meltpool area in terms of # of pixels when frames having laser off time not included	59
Figure 46	Statistical analysis of Meltpool area in terms of # of pixels of Type-I Track 3.....	60
Figure 47	Statistical analysis of Meltpool area in terms of # of pixels of Type-I Track 5.....	60
Figure 48	Statistical analysis of Meltpool area in terms of # of pixels of Type-I Track 7.....	61
Figure 49	Statistical analysis of Meltpool area in terms of # of pixels of Type-II Track 2.....	61
Figure 50	Statistical analysis of Meltpool area in terms of # of pixels of Type-II Track 4.....	62

Figure 51	Statistical analysis of Meltpool area in terms of # of pixels of Type-II Track 6.....	62
Figure 52	Statistical analysis of Meltpool area in terms of # of pixels when frames having laser off time included.....	63
Figure 53	Statistical analysis of Meltpool area in terms of # of pixels when frames having laser off time not included.....	63
Figure 54	Statistical analysis of Meltpool area in terms of # of pixels of Type-I Track 3.....	64
Figure 55	Statistical analysis of Meltpool area in terms of # of pixels of Type-I Track 5.....	64
Figure 56	Statistical analysis of Meltpool area in terms of # of pixels of Type-I Track 7.....	65
Figure 57	Statistical analysis of Meltpool area in terms of # of pixels of Type-I Track 9.....	65
Figure 58	Statistical analysis of Meltpool area in terms of # of pixels of Type-I Track 11.....	66
Figure 59	Statistical analysis of Meltpool area in terms of # of pixels of Type-I Track 13.....	66
Figure 60	Statistical analysis of Meltpool area in terms of # of pixels of Type-II Track 2.....	67
Figure 61	Statistical analysis of Meltpool area in terms of # of pixels of Type-II Track 4.....	67
Figure 62	Statistical analysis of Meltpool area in terms of # of pixels of Type-II Track 6.....	68
Figure 63	Statistical analysis of Meltpool area in terms of # of pixels of Type-II Track 8.....	68
Figure 64	Statistical analysis of Meltpool area in terms of # of pixels of Type-II Track 10.....	69
Figure 65	Statistical analysis of Meltpool area in terms of # of pixels of Type-II Track 12.....	69
Figure 66	The plot of T^2 values against the pixel location obtained from Video#1	70

Figure 67	The plot of T^2 values against the pixel location obtained from Type-I meltpool for Video #1.....	72
Figure 68	The plot of T^2 values against the pixel location obtained from Type-II meltpool for Video #1.....	72
Figure 69	The plot of T^2 values against the pixel location obtained from Video #2	73
Figure 70	The plot of T^2 values against the pixel location obtained from Type-I meltpool for Video #2.....	74
Figure 71	The plot of T^2 values against the pixel location obtained from Type-II meltpool for Video #2.....	74
Figure 72	The plot of T^2 values against the pixel location obtained from Video #4	75
Figure 73	The plot of T^2 values against the pixel location obtained from Type-I meltpool for Video #4.....	76
Figure 74	The plot of T^2 values against the pixel location obtained from Type-II meltpool for Video #4.....	77

CHAPTER 1

INTRODUCTION

Laser Powder Bed Fusion (L-PBF) processes were among the first commercialized Additive Manufacturing (AM) processes. The Powder Bed Fusion (PBF) processes include the following commonly used printing techniques: Direct metal laser sintering (DMLS), Electron beam melting (EBM), Selective heat sintering (SHS), Selective laser melting (SLM) and Selective laser sintering (SLS). Laser Powder Based Fusion process (L-PBF) or commonly known as Selective laser melting (SLM) is a rapid prototyping, 3D printing, or Additive Manufacturing (AM) technique designed to use high power-density laser to melt and fuse metallic powders. A component is built by selectively melting and fusing powders within and between layers. This technique has been proven to produce near net-shape parts up to 99.9% relative density. This enables the process to build near full density functional parts and has viable economic benefits. According to the Wohler report published in 2017 the sale of additive manufacturing products and services have already passed US\$6 billion mark in 2016. The generalized process steps involved during the L-PBF process are as follows-

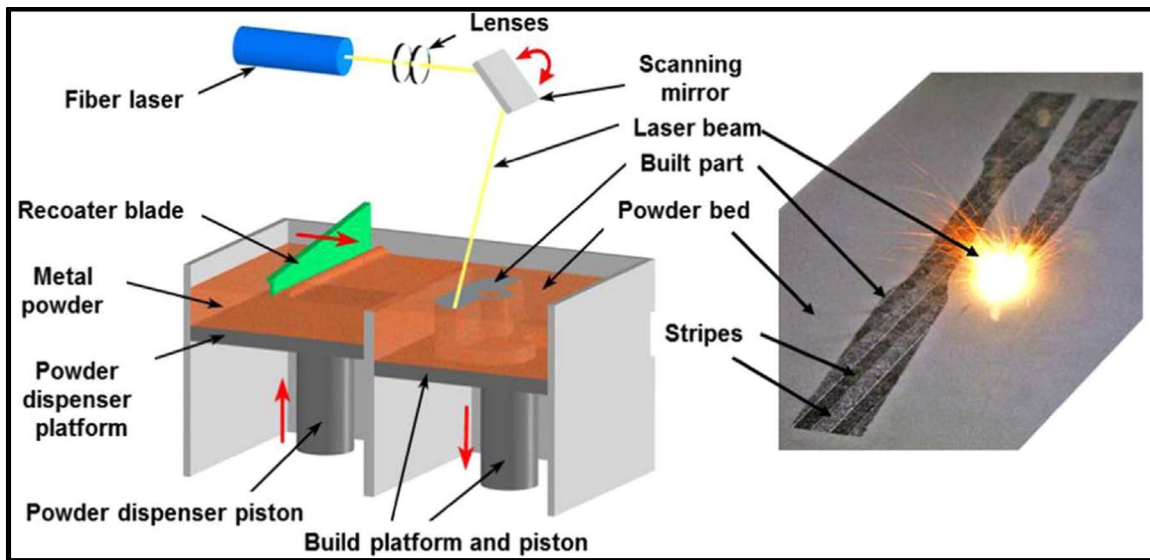
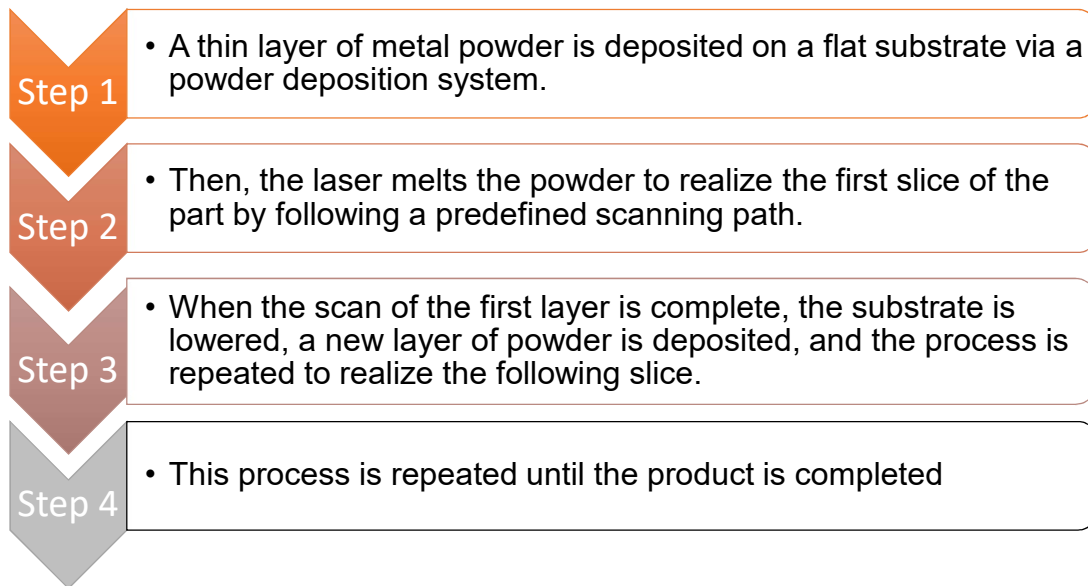


Figure 1: The laser powder bed fusion system by EOS GmbH.

Materials which can be processed through this process are stainless steel, titanium, aluminum, cobalt, nickel, copper, and tungsten. Recent developments of fiber optics and high-power lasers have also enabled L-PBF to process different metallic materials, ceramics, and composite materials.

This layer-by-layer process was first used to produce prototypes, but the trend is towards direct manufacture of components because of its ability to net-shape manufacture complex structures from a Computer Aided Design (CAD) model and a wide range of materials without the need of expensive tooling and machining so that the delay between design and manufacture is minimized. Another advantage is that the powder is melted only locally by the laser and the rest of the powder can be recycled for further fabrication. This method has been used to selectively melt nickel-based super alloys, titanium-based alloys, aluminum-based alloys and niobium-based alloys to fabricate components and structures for automotive and aerospace applications. This manufacturing method is used for the manufacturing of tools for the plastic injection molding and the die casting as well. It is also possible to produce very filigree structures for dental and human implants.



(a)

(b)

Figure 2: Additively fabricated metal parts (a) Hip socket made on Arcam PBF machine, (b) Dental crowns and bridges on EOS PBF machine.

1.1 Metal Additive Manufacturing

Metal Additive Manufacturing, also known as metal 3D printing, offers extensive design freedom with the ability to manufacture parts using a wide range of materials with a target to create complex parts without any design constraints which are quite common in traditional manufacturing processes. The use of Additive Manufacturing (AM) with metal powders is a new and still growing industry sector with many of its leading companies based in Europe. It has become a suitable process to produce complex metal final production shape parts, and not only prototypes, as before. Additive manufacturing now enables both a design and industrial revolution, in various industrial sectors such as aerospace, energy, automotive, medical, tooling and consumer goods.

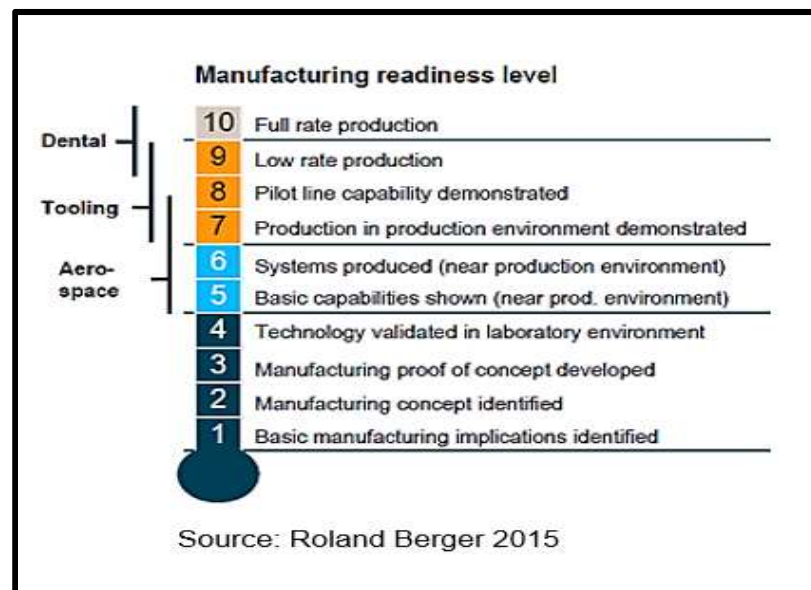


Figure 3: Technology readiness levels of additive manufacturing applications.

Looking at the report from Roland Berger published in 2015 it can be said that starting from prototypes, today's AM systems are not designed for series production. Process speed, material costs and process control have not been an issue for prototyping. AM needs to show that it can manufacture parts economically, in volume and with constant quality for several applications. Several technologies have been developed for additive manufacturing however powder bed fusion remains to be the leading technology for fabricating metal objects.








Additive manufacturing technologies				AM technologies for metal objects
TECHNOLOGY		MATERIALS	TYPICAL MARKETS	
 Powder bed fusion – Thermal energy selectively fuses regions of a powder bed		Metals, polymers	Prototyping, direct part	
 Directed energy deposition – Focused thermal energy is used to fuse materials by melting as the material is deposited		Metals	Direct part, repair	
 Sheet lamination – Sheets of material are bonded to form an object		Metals, paper	Prototyping, direct part	
 Binder jetting – Liquid bonding agent is selectively deposited to join powder material		Metals, polymers, foundry sand	Prototyping, direct part, casting molds	
 Material jetting – Droplets of build material are selectively deposited		Polymers, waxes	Prototyping, casting patterns	
 Material extrusion – Material are selectively dispensed through a nozzle or orifice		Polymers	Prototyping	
 Vat photopolymerization – Liquid photopolymer in a vat is selectively cured by light-activated polymerization		Photopolymers	Prototyping	

Figure 4: Classification of additive manufacturing technologies. Source: ASTM International Committee F42 on Additive Manufacturing Technologies.

AM has several advantages, with freedom of shape being the most important one, but also several drawbacks, especially slow build rates and feedstock availability.

The advantages and disadvantages can be summarized as following:

Advantages

1. Design complexity and freedom: proliferation of metal products which involve levels of complexity that simply could not be produced physically in any other way.
2. Speed of production: complex parts can be created within hours, with limited human resources and intervention.
3. Customization: 3D printing processes allow for customization of metal products which is the ability to personalize products according to individual needs and requirements such as biomedical products.
4. Tool-less production: For low to medium volume applications, industrial 3D printing or additive manufacturing can eliminate the need for tool production and, therefore, the costs, lead times and labor associated with it.
5. Extreme lightweight design: Metal additive manufacturing enables weight reduction via topological optimization.
6. No storage cost: Since it can “print” products as and when needed, and does not cost more than mass manufacturing, no expense on storage of goods is required.

Disadvantages

1. Support material removal: When production volumes are small, the removal of support material is usually not a big issue. When the volumes are much higher, it becomes an important consideration. Support material that is physically attached is of most concern.
2. Limitations of feedstock material: At present, 3D printers can work with approximately 100 different feedstock materials. This is insignificant when compared with the enormous range of feedstock materials used in traditional manufacturing processes.
3. Material cost: Today, the cost of most materials for additive systems (in powder form) is slightly greater than that of those used for traditional manufacturing.
4. Limitations of size: L-PBF printing technology is currently limited by size constraints. Very large objects are still not feasible when building using 3D printers.
5. Residual stresses: Induced by uneven heating and cooling phenomenon that may prove to be significant in high-precision processes.

1.2 Rationale and Motivation

Studies on in-situ process signatures in metal additive manufacturing such as spatter and over melting phenomenon can help to reduce defects and optimize layer structure with different layer thicknesses. Also, the study of melting regions can support the idea of introducing two and more laser systems (e.g. SLM Solutions) seems the most promising alternative to improve process capacity to overcome the application of energy (laser power) per focus point since it is limited by the process parameters. Process parallelization by simultaneous powder dispensing and laser melting can also be achieved depending upon the data obtained from Spatial mapping monitoring methods which focuses on controlling spatter during in-process and will eventually give user control over process stability using online monitoring systems.

Another area where this research would affect is the machine prices which can go up once this self-learning monitoring system is equipped with existing ones to improve quality of parts being produced. Increasing addition of process and quality control electronics as well as number of lasers will raise the machine price, partly offset by economies of scales.

Also, reliable systems will reduce effort for monitoring and troubleshooting techniques. This research will also help to reduce wastage of excess metal powder

in form of spatters happening during in-process as it will cut-off the process once amount of spatter reaches a preset value and asking user to re-adjust the process parameters.

1.3 Research Objectives

The objective of this research is to use of high speed camera videos for in-situ monitoring of L-PBF of nickel alloy 625 to detect spatter and over melting regions to improve the process control capability. The quantities that can be measured via in-situ sensing can be referred to as process signatures and can represent the source of information to detect possible defects. The video images are processed for temporal-spatial analysis by using principal component analysis and T^2 statistics for identifying the history of pixel intensity levels through the process monitoring. These results are correlated as over melting and spatter regions. The results obtained from these studies will provide information about the process parameters which can be used for further validation of modelling studies or for industrial purposes.

Another objective of this research is to study meltpool locations and their types which are being generated during over melting, normal melting and under melting phenomenon. Meltpool measurements can be obtained using filtering and denoising techniques incorporated with studies done by Criales et al. (2017).

CHAPTER 2

LASER POWDER BED FUSION PROCESS

2.1 L-PBF Process Parameters

To certify any new process and to understand various factors affecting the process and quality of products formed, it is relevant to carry out theoretical, experimental and mechanical testing investigations. These experimental investigations are affected by various process parameters which can be optimized for producing satisfactory parts using L-PBF processes. Therefore, the use of optimum process parameters is extremely important.

In L-PBF, process parameters can be consolidated into four major categories:

1. laser-related parameters e.g. laser power, laser-beam spot size
2. scan related parameters e.g. scan strategy, scan velocity, hatch distance
3. powder-related parameters e.g. powder size and layer thickness
4. meltpool geometry and spatter

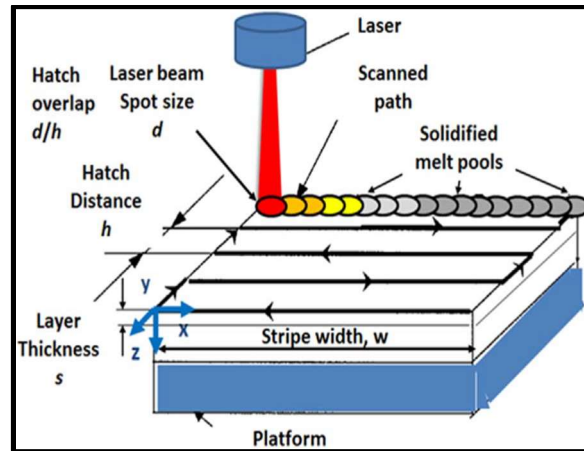


Figure 5: L-PBF terminology (Crales et al. 2017).

2.1.1 Laser Power

Laser is used as a primary energy source for melting and solidifying the powder material and manufacturing metallic products. Laser power is defined as power level that is transferred by the laser beam to the powder bed. It affects proper fusion of powder melt in powder bed to achieve fully dense part when laser scans the surface of the powder bed.

2.1.2 Scan Strategy

Scanning patterns have a major influence of various features e.g. porosity, microstructure, surface roughness and heat build-up in the products being formed by the L-PBF process. As mentioned in previous sections, L-PBF process flow consists of steps such as; components are digitalized into 3-d design using software, sliced and stacked into layers. Then, as per the algorithm in the software which is being used by the 3-D printing machine decides how to manage regions

by splitting it into various regions to control laser movement accordingly. The three main types of scanning patterns currently used are, stripe, checkerboard and islands patterns.

Stripe pattern: This pattern is defined by various process parameters such as stripe width, the hatching space between adjacent tracks and the scan direction as well as the overlap with the neighboring stripes (see Fig. 6).

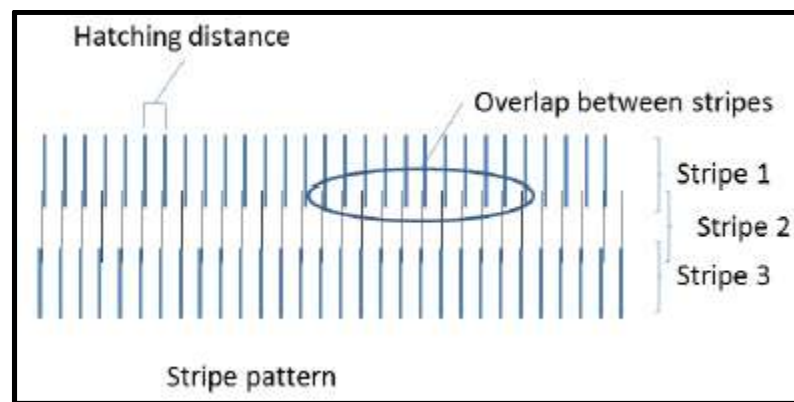


Figure 6: Schematics of stripes and hatching pattern.
Source: insidemetaladditivemanufacturing.com

Chess-board pattern: The chessboard pattern also known as checkerboard pattern – which is defined by individual squares placed on a chess board. This pattern is defined by the side length of the square, the hatching distance between adjacent tracks and the overlap between squares. The sequence of processing these individual squares are automatically selected by the machine depending upon the similarities between them (see Fig. 7).

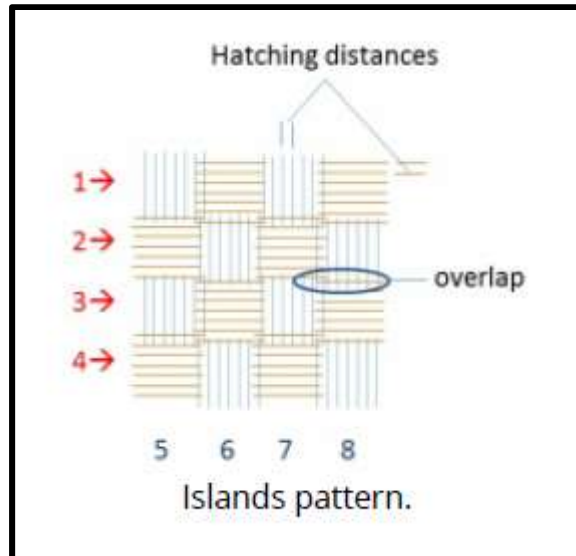


Figure 7: Schematics chessboard scanning and hatching patterns.
Source: insidemetaladditivemanufacturing.com

Islands pattern: This is just like chessboard pattern with an exception of squares being processed in random order. Here each square is printed randomly across the layer, in no order. Process parameters such as square side width, overlap and hatching distance ensure no powder is left unmelted (see Fig. 8).

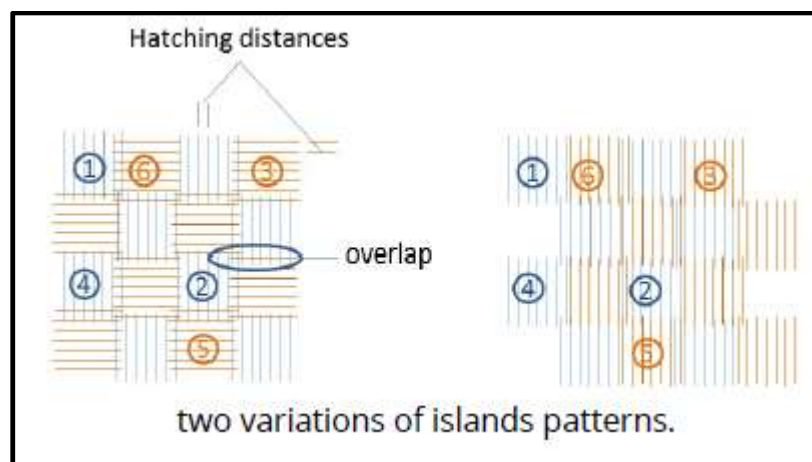


Figure 8: Schematics of islands and other hatching patterns.
Source: insidemetaladditivemanufacturing.com

2.1.3 Scan Velocity

According to study by Kamath et al. (2016) scan velocity is considered as the most important process parameters in L-PBF process. This study says that a higher scan velocity causes the interaction between material and the laser beam to be short, which allows the process to achieve narrow meltpool which also leads to surface roughness, whereas decreasing the scan velocity causes excessive heating and vaporization. Also, high value of scanning velocity when used during the process causes instability and droplet formation due to free cylindrical meltpool geometry and low values cause balling effect. Therefore, a tradeoff is required between the low and high values to achieve desired quality of products.

2.1.4 Hatch Distance

Hatch distance is the distance between two neighboring scan vectors, hatch lines. It is usually less than the laser beam diameter and can be varied. Some areas in the powder bed are exposed to multiple scanning. Cross section may not be fused, if the hatch spacing is too much.

2.1.5 Powder Bed

Powder shape, size, and its distribution strongly affect laser absorption characteristics as well as powder bed density, powder bed thermal conductivity, and powder spreading. Finer grain particles give greater surface area and help in absorbing laser energy more efficiently than coarser particles. Powder bed temperature, laser power, scan speed, and scan spacing must be balanced to provide the best tradeoff between meltpool size, dimensional accuracy, surface finish, build rate, and mechanical properties. The powder bed temperature should be kept uniform and constant to achieve repeatable results. Generally, high-laser-power/ high-bed-temperature combinations produce dense parts, but can result in part growth, poor recyclability, and difficulty cleaning parts. On the other hand, low-laser-power/ low-bed-temperature combinations produce better dimensional accuracy, but result in lower density parts and a higher tendency for layer delamination. High-laser-power combined with low-part-bed-temperatures results in an increased tendency for non-uniform shrinkage and the build-up of residual stresses, leading to curling of parts. The powder bed density, as governed by powder shape, size, distribution, and spreading mechanism, can strongly influence the part quality. Powder bed densities typically range between 50 and 60 % for most commercially available powders, but may be as low as 30 % for irregular ceramic powders. Generally, the higher the powder packing density, the higher the bed thermal conductivity and the better the part mechanical properties. Layer thickness is an important element in L-PBF process. Layer thickness is defined as

the depth that build platform is lowered between each layer. Layer thickness defines powder layer thickness to be fused with one process cycle. It takes longer time to build part if smaller layer thickness is used, but on the other hand smaller layer thickness can decrease surface roughness.

2.2 L-PBF Process signatures

2.2.1 Meltpool Geometry

There are basically two types of meltpool geometry data: a) meltpool dimensions (width and depth), b) meltpool shape among others such as length (see Fig. 9).

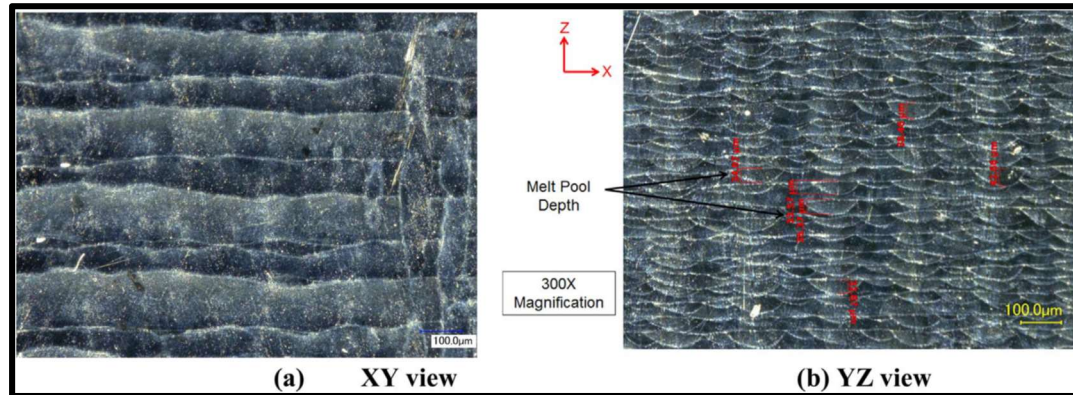


Figure 9: Views of surfaces generated with L-PBF process in nickel alloy IN625 ($P=195\text{ W}$, $v_s=800\text{ mm/s}$, $h=0.1\text{ mm}$). (a) XY top view (b) YZ side view (Criaes et al. 2017).

Also, the different types of meltpool created during the L-PBF process have different geometries as well. There are mainly two types of meltpool observed due to different laser scanning process;

1. Type-I meltpool: meltpool area being processed is still within the heat-affected zone of the previous hatch scanning (or track processing).
2. Type-II meltpool: meltpool area currently being processed is no longer affected by the heat from laser scanning of the previous track or hatch.

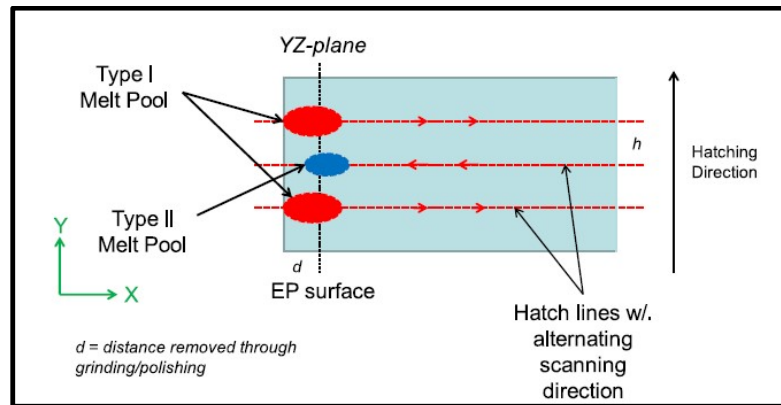


Figure 10: Definition of Type-I and Type-II meltpools (Criaes et al. 2017).

The size of the dynamic meltpool also depends on the scanning direction. Meltpool at a location at the beginning of the track will be larger (Type-I) and meltpool at a location at the end of a processed track will be smaller (Type-II). The difference in meltpool sizes can be attributed to the presence of a heat-affected zone (HAZ) and rapid cooling times. Digital optical microscopy imaging and thermal camera imaging were used to corroborate with these results by Criaes et al. (2017).

2.2.2 Meltpool Shape Analysis

Laser heating and heat affected zone produces a notable effect on the geometrical shape of the meltpool so that meltpool shape may not be symmetrical. For this

analysis, Criaes et al. (2017) considered the cross-sectional (YZ-plane) view of the meltpool as obtained from digital microscopy imaging. The meltpool width, w , and the distance from the edge of the meltpool farther away from the previous track to the location at which the maximum melted depth is observed, a , were measured (see Fig. 11). Then the measure for the meltpool shape was defined as follows,

$$\varphi(a, w) = \frac{a - w/2}{w/2} = \frac{2a - w}{w} \quad \text{Eq. (1)}$$

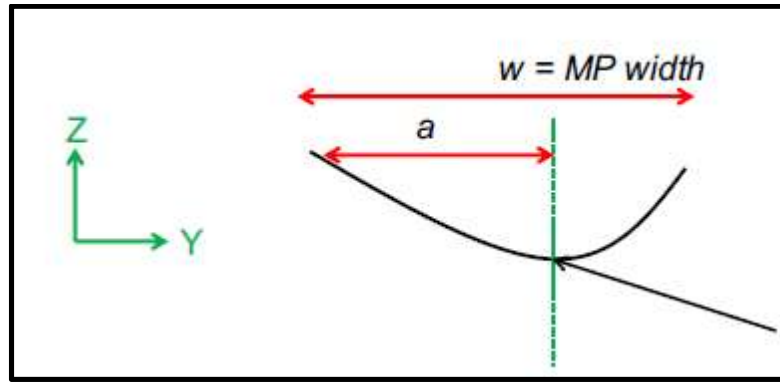


Figure 11: Meltpool shape definition (Criaes et al. 2017).

They made two kinds of observation: 1) If the meltpool is perfectly symmetrical about the z-axis, then $a=w/2$ and $\varphi=0$, or 0%. 2) On the completely skewed contrary, if the meltpool is completely skewed towards the previous processed hatch due to the heat-affected zone, then $a \rightarrow w$, in which case $\varphi \rightarrow 1$, or 100%. In summary, they suggested that this measure gives a value between 0 and 1 (or 0% and 100%) that quantifies how asymmetrical the melt pool geometry is.

2.2.3 Material Spatter

Strong temperature gradients below the laser generate temperature-dependent and complex hydrodynamic flows in the melt pool that generate spatter formation during laser processing of the powder material (Khairallah & Anderson 2014).

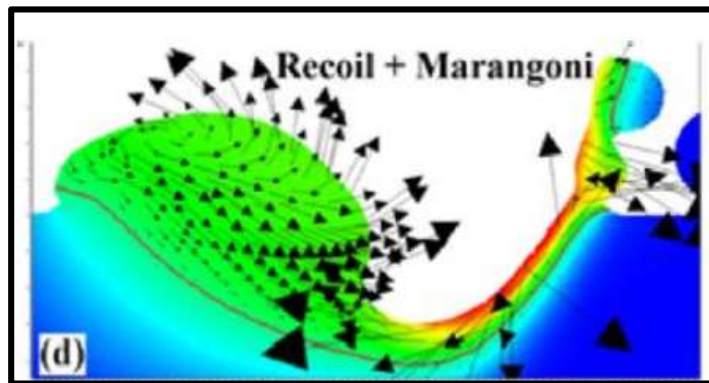


Figure 12: Melt pool dynamic model (Khairallah & Anderson 2014).

Among these effects, the surface tension gradient generates surface convection flows known as the Marangoni effect. It generally drives the melt flow from the hot laser spot toward the cold rear end of the track being processed. The result is an increase of the melt depth, recirculation of the melt flow and creation of spattering as high-speed surface liquid metal that may break away from the more viscous (cooler) body of the melt pool as explained in Khairallah & Anderson (2014). All of these complexities exist in L-PBF process which is not fully understood and requires much better in-situ process monitoring and analysis techniques.

CHAPTER 3

MATERIAL AND EXPERIMENTAL SETUP

3.1 Material

In L-PBF experiments, an adequate quantity of commercially available nickel alloy 625 powder which is produced by gas atomized process with the average particle size of 35 μm was used. This powder material has 325 mesh size (particles that measure less than 44 μm) and atomized spherical morphology that contains a particle size distribution of $D_{60\%}=29.4\ \mu\text{m}$, $D_{10\%}=13.5\ \mu\text{m}$, and $D_{90\%}=43.0\ \mu\text{m}$. The chemical composition of the powder material in weight % is given in Table 1.

Table 1: Chemical composition of nickel alloy 625.

Cr	Fe	Mo	Nb	C	Mn	Si	P	S	Al	Ti	Co	Ni
21.01	0.85	8.77	3.35	0.02	0.36	0.39	0.005	0.003	0.1	0.1	0.1	64.94
%	%	%	%	%	%	%	%	%	%	%	%	%

3.2 Experimental Setup

An EOS M270 Direct Metal Laser Sintering (DMLS) machine was utilized to carry out this experiment and build test coupons. This PBF machine has a single-mode, continuous wave (CW) ytterbium fiber laser with maximum power of 200 W. Nickel

alloy 625 powder was used and solid coupons in the shape of cubes (16 mm×16 mm×15 mm) were manufactured using in the DMLS machine under nitrogen gas ambience at the National Institute for Standards & Technology (NIST) facility located in Gaithersburg, Maryland, USA. Experiments were designed to establish a relationship between process parameters and part quality. The Box- Behnken design for three factors is based on considering process parameter combinations at the midpoints of the edges of the process space cube, as well as at the center (Criales et al. 2017). Therefore, three levels of each factor are considered. These low, medium, and high levels for each factor are defined as: P=169 W, 182 W, and 195 W, vs=725 mm/s, 800 mm/s, and 875 mm/s, and h=0.09 mm, 0.10 mm, and 0.11 mm. The energy density is defined as the amount of energy applied to the powder bed per unit volume and is a function of laser power (P), scan velocity (vs), hatch distance (h), and layer thickness (s), as given in Eq. (2).

$$E = \frac{P}{v_s \cdot h \cdot s}$$

Eq. (2)

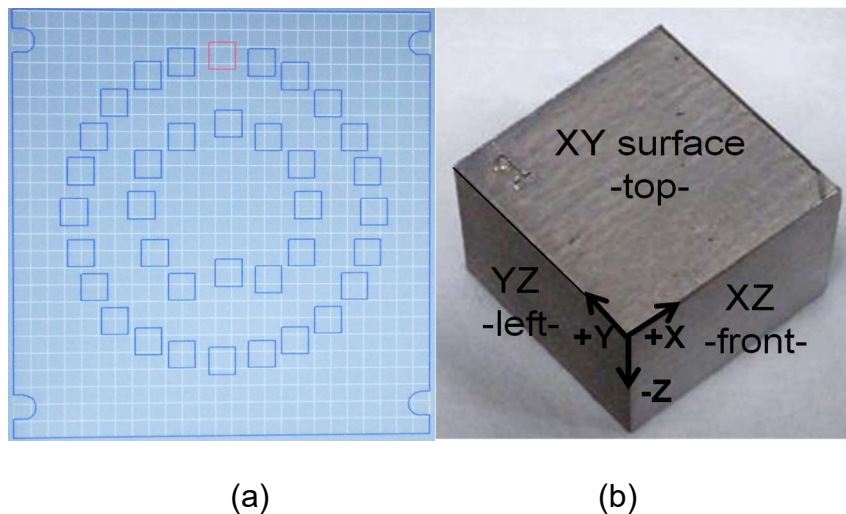


Figure 13: (a) Build platform layout, (b) Image of a built cube (Özel et al. 2017).

Criales et al. (2017) further describes their experimental studies as follows. The powder layer thickness is kept constant at $s=20\text{ }\mu\text{m}$. The test coupons fabricated using these parameter settings are $16\text{ mm}\times 16\text{ mm}$ at the base, and 15 mm in height. The final height of the coupons is less than 15 mm , as wire electrical discharge machining (w-EDM) is used to separate the built coupons from the platform, and some of the coupon remains attached to the platform. 16 mm was selected as the width and length of the coupons so that each processed layer of powder is composed of four 4-mm wide stripes. Stripe overlap, defined as the area of material in which laser scanning overlaps by consecutive stripes, is 0.1 mm . Therefore, total stripe width is 4.1 mm . At first, a set of 18 coupons were fabricated using 90° rotation in scanning direction (stripe orientation) between layers. A second set of coupons, following the same experimental design as the first set, was processed using the default scanning rotation (stripe orientation) setting of the L-PBF machine, which is estimated to be an approximately 67° rotation.

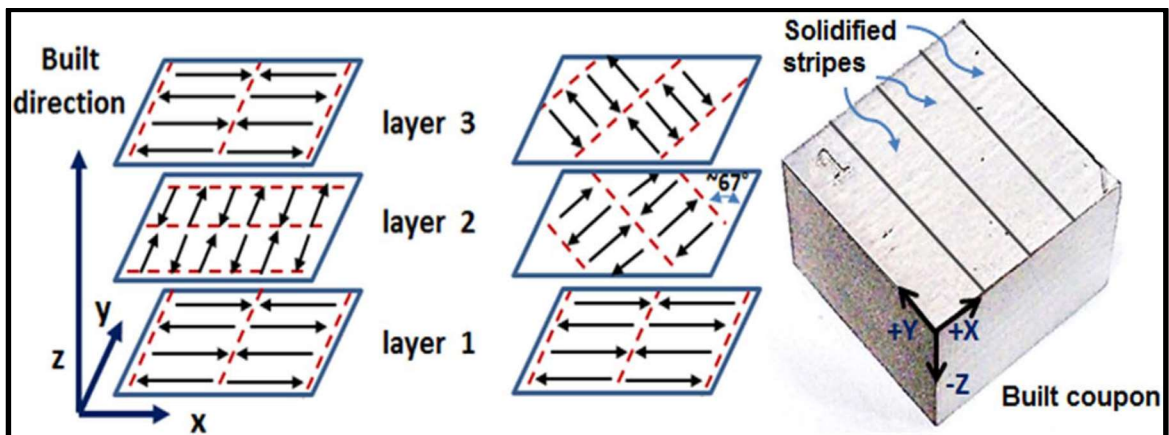


Figure 14: Schematic of a stripe scan pattern with 90° (left) and 67° (right) CCW rotation between consecutively built layers (Özel et al. 2017).

3.3 In-situ Process Monitoring

A high-speed camera was used for performing an in-situ process monitoring to quantitatively analyze melt pool size and understand spattering behavior and to analyze them. Video recordings of the process were obtained from a camera which was placed in the L-PBF process chamber (see Fig. 15). Due to the nature of the process, i.e., a laser beam moving at very high speeds, a high frame rate (HFR) camera is required. This setup was organized at the National Institute of Standards and Technology (NIST) facility in Gaithersburg MD, to observe a portion of the build area of an L-PBF machine, and the process has been recorded for a test coupon that was fabricated using $P=195$ W, $v_s=800$ mm/s, and $h=0.10$ mm.

Table 2. Parameters of high-speed camera.

High Speed Camera	Photron
Integration Time	0.1 ms - 0.5 ms
Frame Rate	2000 frames/s 10000 frames/s 24000 frames/s
Imaging window	512 pixels x 128 pixels 1024 pixel x 256 pixel

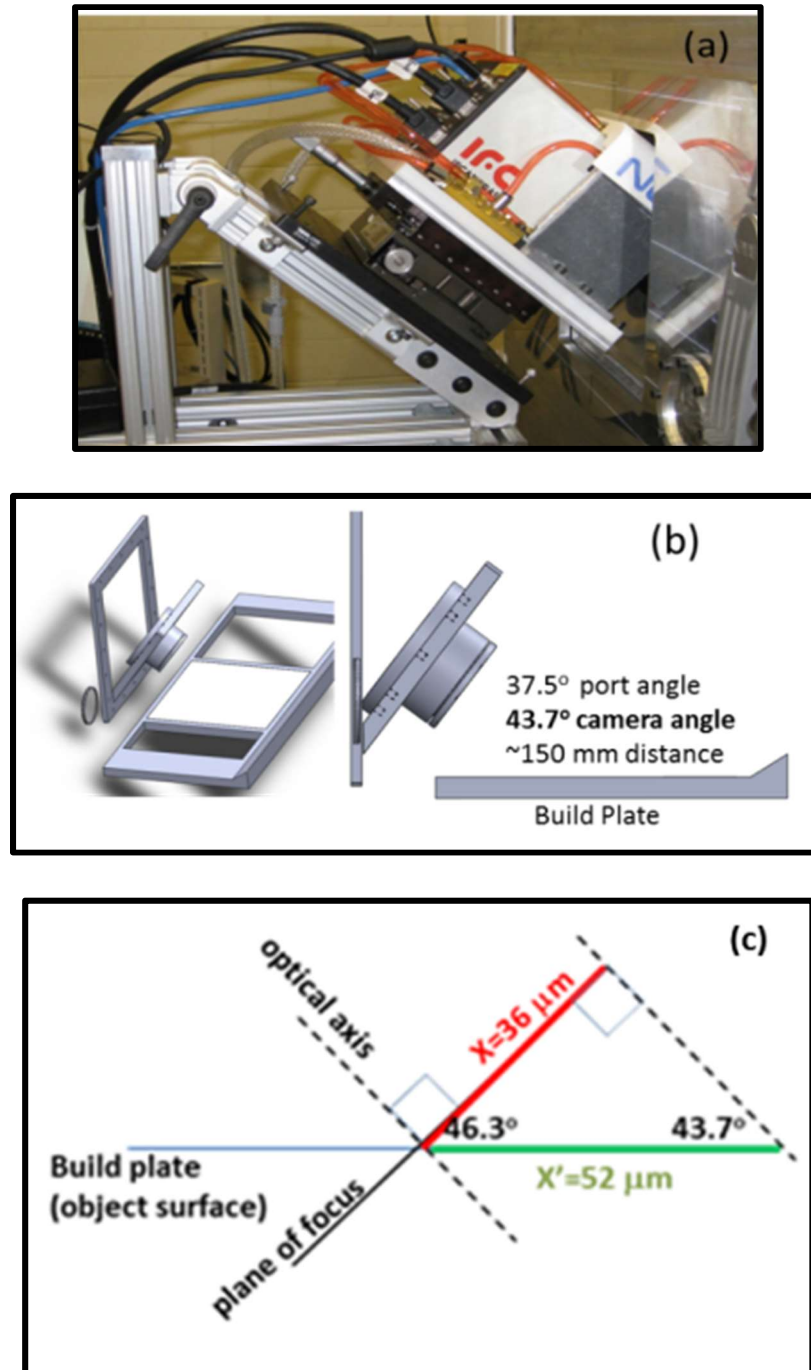


Figure 15: High speed camera set-up: (a) Side-view of the L-PBF machine, custom door, and high-speed camera, (b) CAD solid model of L-PBF machine build chamber and custom viewport, (c) optical axis, plane of focus and vertical iFoV projected on the build plane. (Criaes et al. 2017).

CHAPTER 4

STATISTICAL PROCESS MONITORING OF L-PBF PROCESS

Statistical process control (SPC) is a dynamic monitoring method where product quality is actively measured and simultaneously controlled while manufactured goods are being mass produced when compared to quality assurance methods which typically collect process evidence after a production process has been completed. Today due to continuous growth and advancement in additive manufacturing processes for metals, the complexity of these manufacturing processes and the amount of in-situ data obtained by using various statistical monitoring equipment lead to growing demands on the company to control process parameters to produce quality products (Akandea et al. 2016). To control and eliminate the production of waste and improve the quality of future products, statistical process control (SPC) techniques are designed and applied to monitor production processes (Grasso & Colosimo 2017). The emphasis is on the prevention of problems before they occur instead of simply revealing and correcting past mistakes. The problem of defected products obtained through various AMs are detected too late which needs to be controlled and optimized. A possible approach to confront with these challenges is the development of self-learning assistance systems, which would identify failures, anomalies happening during in-situ and would take statistical approach to identify and auto correct process parameters to achieve desired results. Different manufacturing systems can be synced with this assistance system to figure out various data acquisition

approaches and flexible methods for process monitoring, which can be adapted with model-learning approaches to changing process behavior. The assistance system comprises of data acquisition, process monitoring and anomaly detection in L-PBF processes. However, these approaches are not frequently used in industrial applications because they are not yet suitable for the required processing of big amounts of data.

The quality of L-PBF made parts is known to be influenced by process parameters and the quality of input material. Monitoring the quality of parts manufactured using AMs machines is to be done regularly. Products with benchmark measures should be designed and manufactured to track key quality characteristics of strength, bending stiffness, density and dimensional accuracy of parts made in multiple builds. Using data collected from the benchmark tests, correlation analysis and statistical process control (SPC) charts needs to be established. SPC is a useful tool that can provide L-PBF users with the mean of identifying possible changes in the process. Therefore, it can be used for process monitoring in L-PBF process to ensure consistency in part quality for long term production. Real time melt pool and spatter analysis can help control to achieve desired quality using feedback control system in L-PBF processing technology for metal parts was proposed by Grasso et al. Based on the SPC analysis informed decisions can be taken to maintain the quality of the product. SPC can therefore serve as the voice of the process and by associating it with various control charts and statistical indicators. Two major types of Statistical monitoring procedures currently being used in this

sector are; i) statistical monitoring of product attributes, ii) statistical monitoring of process signatures.

4.1 Statistical monitoring of product attributes

Statistical monitoring can be used for quality attributes of discrete products such as geometric deviations, dimensions, surface roughness, flatness, roundness, straightness, cylindricity etc. (Colosimo et al. 2008, Colosimo et al. 2014). These attributes are measured and sampled to be incorporated into statistical monitoring and quality control scheme by using univariate or multivariate control charts, univariate or multivariate time series models and are frequently used in industrial applications since they are suitable not requiring big amounts of data (Colosimo et al. 2015).

4.2 Statistical Monitoring of Process Signatures

On the other hand, statistical monitoring can also be used for quality attributes of process signatures of especially emerging technologies e.g. micromanufacturing, additive manufacturing combined with new inspection solutions (e.g., non-contact systems, X-ray computer tomography) and fast multi-stream high-speed sensors (e.g., videos and images; acoustic, thermic, power and pressure signals) are paving the way for a new generation of industrial big-data requiring novel modeling and monitoring approaches for zero-defect manufacturing (Kamath et al. 2016). These process signatures are continuously inspected after dimension reduction to

be incorporated into statistical monitoring and quality control scheme by multivariate control charts or multivariate time series models but not frequently used yet in industrial applications since they require processing of big amounts of data. The quantities that can be measured via in-process monitoring can be referred to as “process signatures”, and can represent the source of information to detect possible defects (Grasso & Colosimo 2017; Grasso et al. 2017; Grasso et al. 2018).

4.3 High Speed Camera Videos

The experimental setup mentioned in previous sections was used to capture videos of ongoing process in a single layer focusing on specified cross-sectional area. The video files collected have the configurations and parameters given in Table 3.

Table 3: Parameters of the high-speed camera videos.

Video #	Frames per second	Resolution (Pixels)	Duration (seconds)	Integration time	No of Frames	Zoom
1	10000	512 X 128	0.2231	1/10,000 s	2232	No
2	24000	512 X 128	0.1000292	1/10,000 s	2408	No
4	24000	512 X 128	2.077833	1/24,000 s	49869	Yes (X1)

Each video file was used to obtain stream of image frames for carrying out statistical monitoring methods to study spatter analysis and over melting

phenomenon. With the use of high spatial resolution camera and power lens, it is possible to obtain image stream for all layers. After obtaining these videos they were processed for removal of embedded logos inside them to prevent their effects on statistical descriptors.

4.3.1 Frames per Second (FPS)

FPS stand for frames per second, a measurement for how many unique consecutive images a camera can handle each second.

4.3.2 Image Resolution

Resolution is one of most commonly used ways to describe the image quantity of digital camera or other optical equipment. Images are usually represented in the spatial domain, and quantization is done for the brightness values. The domain of images is divided into N rows and M columns. The cross section of a row and a column is known as pixel and the value assigned to each pixel is the average brightness of the regions. The position of each pixel was described by a pair of coordinates (i, j) (see Fig. 16). The resolution of an image is the number of pixel is the number of pixel presented in the number of columns \times number of rows. For example, an image with a resolution of 640×480 means that it displays 640 pixels on each of the 480 rows.

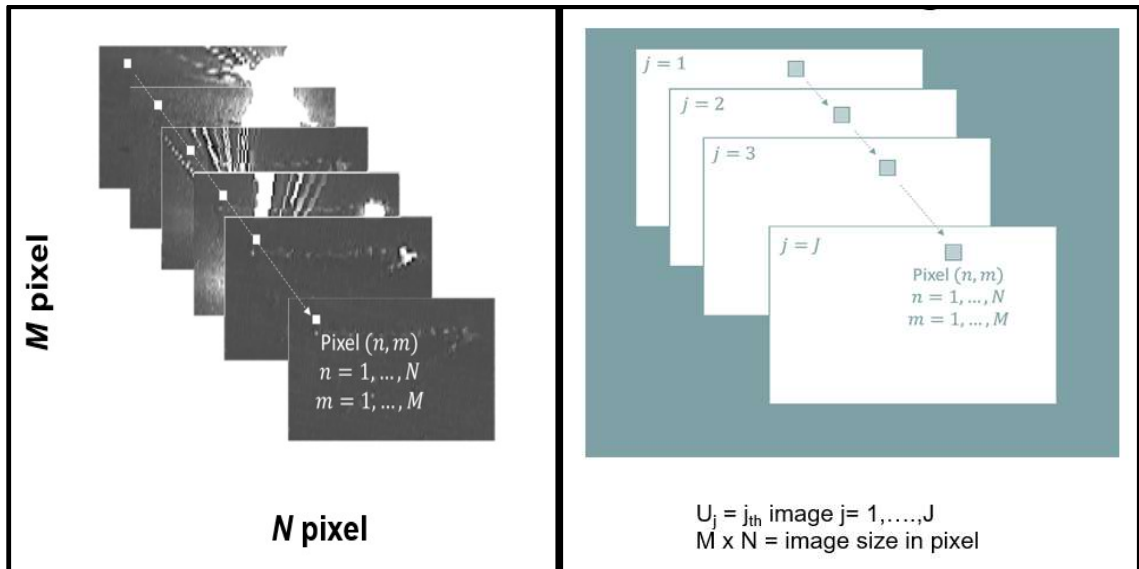


Figure 16: Representation of video frames in time and pixel space (Repossini et al. 2017).

4.3.3 Integration Time

Integration time is that time to process each frame to integrate into the video. If the integration time is greater than FPS then there is a possibility that some frames will be skipped. The captured frames will be integrated into the video, however there will no new frames capture until the integration is completed.

CHAPTER 5

METHODOLOGY

The methodologies used in analyzing the high-speed videos will be described in this chapter. These methodologies include image processing and statistical analysis techniques such as Principal Component Analysis (PCA). Principal component analysis is used for image data processing to provide a temporal analysis of the high-speed camera image streams and a statistical descriptor based upon Hotelling's T^2 distance is used for image data to provide a spatial analysis of the image streams in a video.

The following processing steps were followed for PCA of the image streams.

- 1) **Prepare the data:** Center the data i.e. subtract the mean from each variable. This produces a data set with mean value as zero.
- 2) **Calculate the covariance/correlation matrix**
- 3) **Calculate the Eigenvectors** (vectors which are fixed in direction under a given linear transformation) and the **Eigenvalues** (scaling factor of eigenvectors) of the covariance matrix.
- 4) **Choose Principal Components:** eigenvectors are ordered by eigenvalues from the highest to the lowest. The number of chosen eigenvectors will be the number of dimension of the new data set.
- 5) **Compute the new data set** based upon eigenvalues and eigenvectors.

According to Grasso et al. (2017) the videos acquired from the experimental setup consists of image streams which is represented as a three-dimensional array $\mathcal{U} \in \mathbb{R}^{J \times M \times N}$, where J is the total number of acquired frames from $j=1$ to J and (M X N) is the size in pixel of each frame. In other words, $(U_1, U_2 \dots U_J)$ represents stream of images where $U_j \in \mathbb{R}^{M \times N}$ is the j^{th} image of size (M X N) and $j= 1$ to J. The vectorized PCA is the most common way of applying PCA techniques to image data, which involves transformation of bi-dimensional samples (i.e. frames) into one dimensional vectors. This conversion process is also known as ‘unfolding’ operation. There are two types of PCA techniques which were used into this study:

- 1) Temporal Principal Component Analysis (Time dependent)
- 2) Spatial Principal Component Analysis (Space dependent)

5.1 Image Types

There are three types of images considered, which are described below.

5.1.1 Binary Image

It is a logical array of 0s and 1s, interpreted as black and white, respectively. Any array of 0s and 1s whose values are of data class, say, *uint8* is not considered a binary image in Matlab. A numeric array is converted to binary using function `logical`.

5.1.2 Grayscale Image

It is a data matrix whose values represent shades of gray. It is also known as an intensity, gray scale, or gray level image. Array of class *uint8*, *uint16*, *int16*, single, or double whose pixel values specify intensity values. For single or double arrays, values range from [0, 1]. For *uint8*, values range from [0,255]. For *uint16*, values range from [0, 65535]. For *int16*, values range from [-32768, 32767].

5.1.3 True Color Image

It is also known as an RGB image. A true color image is an image in which each pixel is specified by three values one each for the red, blue, and green components of the pixel scalar. M by-n-by-3 array of class *uint8*, *uint16*, single, or double whose pixel values specify intensity values. For single or double arrays, values range from [0, 1]. For *uint8*, values range from [0, 255]. For *uint16*, values range from [0, 65535].

CHAPTER 6

TEMPORAL AND SPATIAL ANALYSIS OF IMAGE STREAMS

6.1 Temporal Principal Component Analysis

Temporal PCA is performed on the stream of images $\mathcal{U} = \{U_1, U_2, \dots, U_3\}$. According to Grasso et al. (2017) three-dimensional array i.e. $\mathcal{U} \in \mathbb{R}^{J \times M \times N}$ is transformed into a matrix $X \in \mathbb{R}^{J \times p}$, where $p = M \times N$. Each row of matrix in here consists of a pixel intensity profile. Principal components generated through vectorized PCA associates a weight to each frame (see Fig. 17).

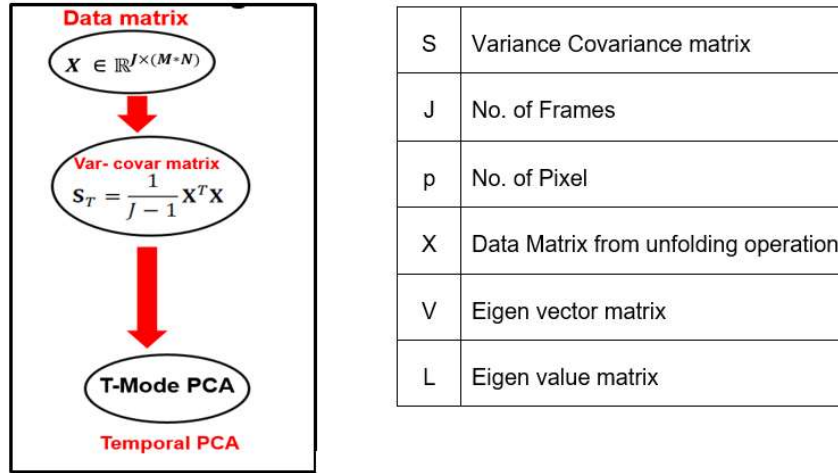


Figure 17: Statistical analysis methodology for temporal PCA.

Spectral decomposition of the variance covariance matrix $S \in \mathbb{R}^{J \times J}$, of the $p \times J$ data matrix is then done which is given by $V^T S V = L$. Extracted PCs are linear combination of frames from $j = 1$ to J . The relative importance of each PC i.e. the

amount of explained variance is represented by the value of the corresponding eigenvalue. Reduced number of principal components are used to represent the relevant information without any loss.

Then a graph for mean gray level values vs the frames from $j = 1$ to J in the video file is plotted. Gray level resolution refers to the predictable or deterministic change in the shades or levels of gray in an image. The number of different colors in an image is depends on the depth of color or bits per pixel (0 = black and 256 = White). The mathematical relation that can be established between gray level resolution and bits per pixel can be given as. $L = 2^k$ in this equation L refers to number of gray levels. It can also be defined as the shades of gray. And k refers to bpp or bits per pixel. In our approach, we are quantizing the gray level value from 0 to 256 on Y-axis against # of frames on X-axis (see Fig. 18).

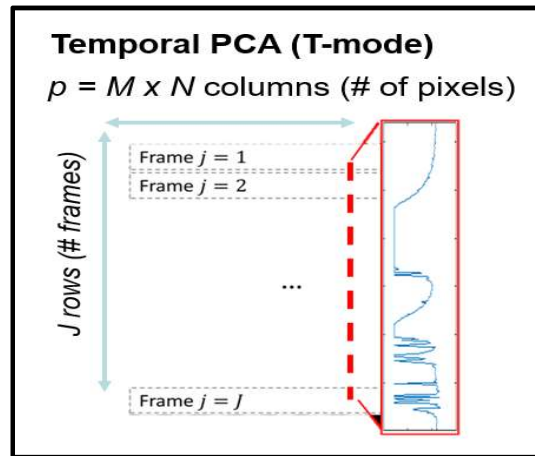
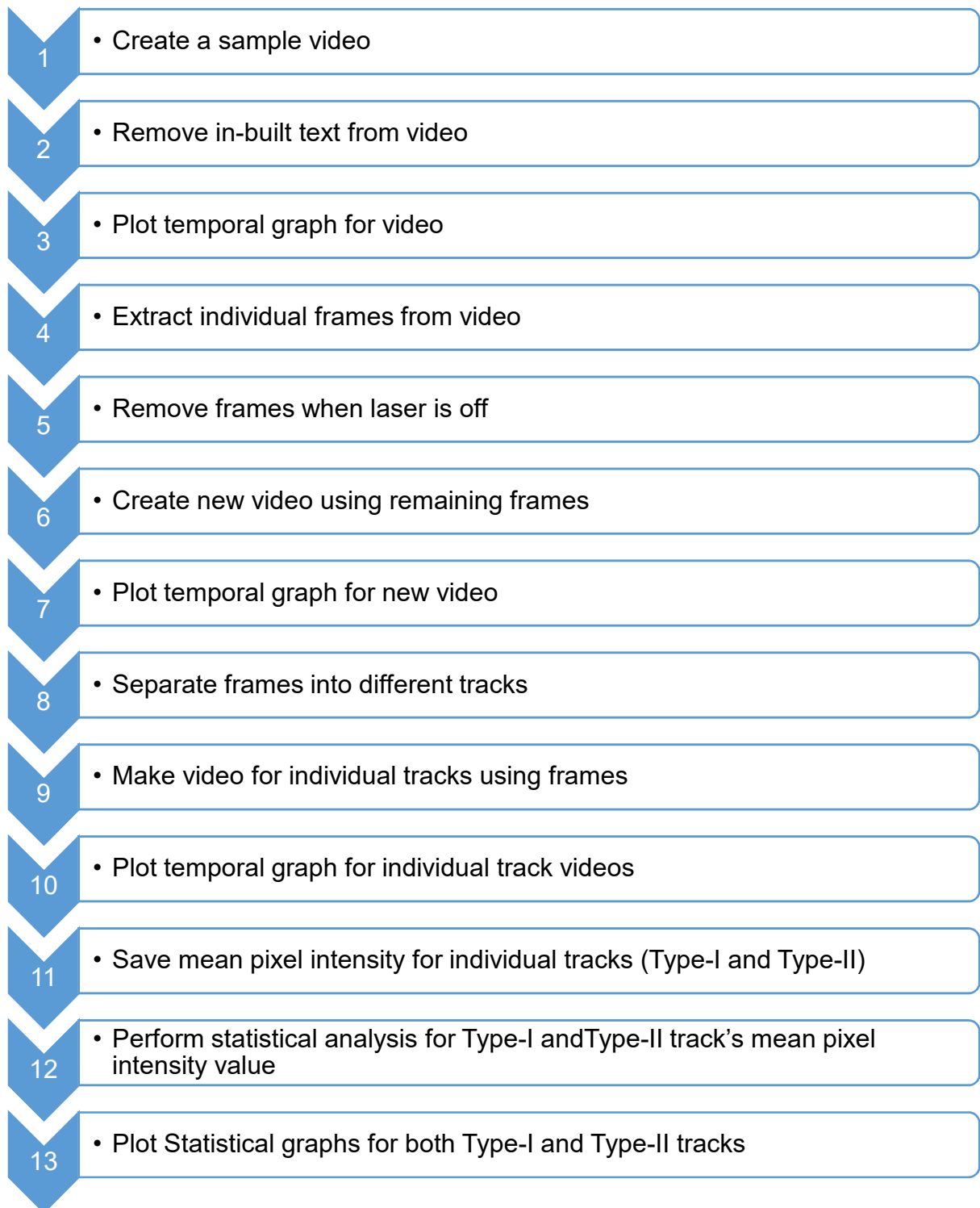


Figure 18: Representation of temporal PCA.

6.1.1 Process Flow for Temporal Principal Component Analysis



Step 1: First, we used video cutter software for cutting a small sample of video file so that it can be easily processed in Matlab.

Step 2: Then, we used Wondershare Filmora software to remove inbuilt text so that it does not affect the statistical results obtained after processing. We also cropped video to focus only on workspace area for laser. Then we saved this edited video sample.

Step 3: Then we used Matlab script *video.m* to perform temporal analysis and plot graph. This script processes video frame by frame (see Appendix). For each frame, we converted it from RGB image to gray scale intensity image mainly to make the image simpler for analysis, and reduce the amount of code to be written in Matlab. When an image is digitized or processed, a brightness levels that vary continuously must be quantized i.e. assigned a value on a scale between white and black and shades of grey in between: that value is the gray level. We collected average of the gray scale intensity values for all pixels in individual frames called mean gray level value and plotted it against time (frame).

Step 4: Then we used Matlab script *frameextraction.m* to segregate individual frames of the video sample and saved it in a separate folder (see Appendix).

Step 5: Then we identified frames which included the time for which laser is inactive while changing tracks. We removed these frames from the existing pool of frames.

Step 6: Then we used Matlab script *makevideo.m* to combine the remaining frames from above step to make a new video sample (see Appendix).

Step 7: Again, we used Matlab script *video.m* to perform temporal analysis and plot graph (see Appendix).

Step 8: Also, we separated frames obtained in step 5 into different tracks the laser follows during the process and saved it in different folders marked as track 1, track 2....and so on.

Step 9: We recombined the frames obtained for individual tracks to create video sample for individual tracks using Matlab script *makevideo.m* (see Appendix).

Step 10: Again, we used Matlab script *video.m* to perform temporal analysis and plot graph.

Step 11: One of the outputs of Matlab script *video.m* gives an array of mean gray level intensity values for each frame. We performed statistical analysis using these values by calculating mean and standard deviation of the mean gray level intensity values obtained for all tracks in Type-I and-II separately.

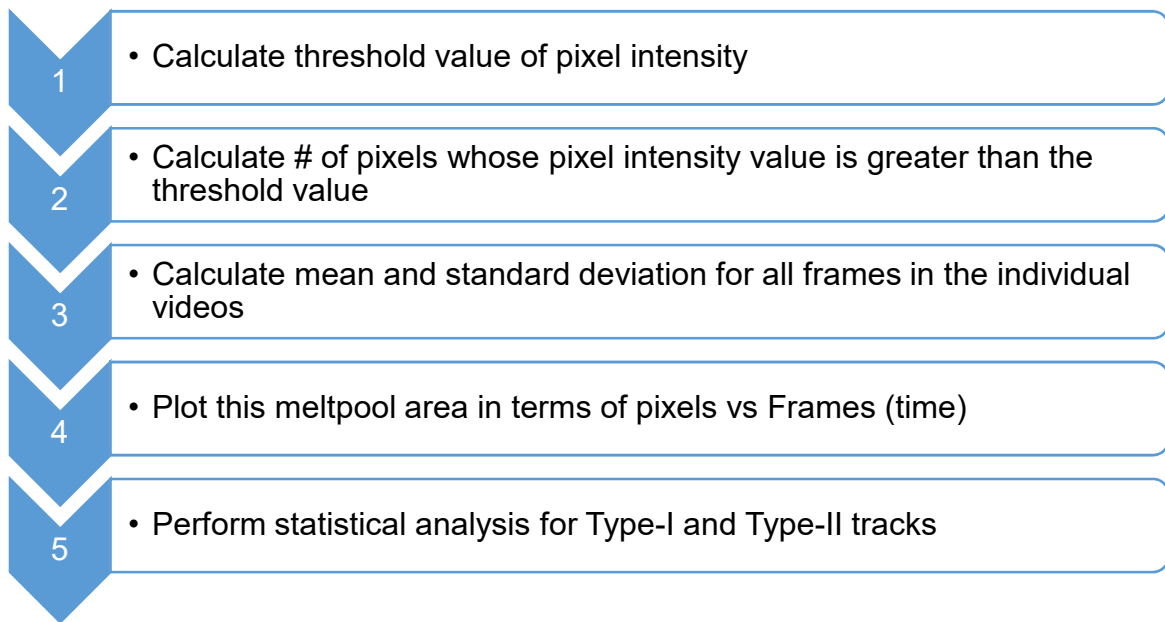
Step 12 and 13: Then we plotted a statistical analysis graph to study and understand the melt pool types formed during the process.

6.1.2 Additional Processing

Gray scale images have some flares coming out of meltpool. We can eliminate minor flares if we convert it to BW image. We also introduce a new variable called threshold value in this processing. It is obtained by taking average of the mean gray level values of each frame obtained using Matlab script *video.m*.

According to Matlab we can convert a gray Image to BW image by using following code:

- `BW = imbinarize(I)` creates a binary image from image `I` by replacing all values above a globally determined threshold with 1s and setting all other values to 0s. By default, `imbinarize` uses Otsu's method, which chooses the threshold value to minimize the intraclass variance of the thresholded black and white pixels. `imbinarize` uses a 256-bin image histogram to compute Otsu's threshold. `BW` is the output binary image.
- `BW = imbinarize (I, method)` creates a binary image from image `I`, using the thresholding method specified by `method`: 'global' or 'adaptive'.
- `BW = imbinarize (I, T)` creates a binary image from image `I`, using the threshold value `T`. `T` can be a global image threshold, specified as a scalar luminance value, or a locally adaptive threshold, specified as a matrix of luminance values.
- `BW = imbinarize (I, 'adaptive', Name, Value)` creates a binary image from image `I`, using name-value pairs to control aspects of adaptive thresholding.
- `J = imbinarize (V, ____)` binarizes volume `V`, using the same defaults as the syntax for grayscale images. `imbinarize` supports 3-D binary conversion for both global and adaptive thresholding. `J` is the output binary volume.



Step 1: As explained above, we used the Matlab script *video.m* to obtain mean gray level intensity values for each frame in an array format (J X 1) where J represents # of frames. We then calculated average value of all the mean gray intensity level for all frames and named it as threshold value.

Step 2: We used Matlab script *pixel.m* to first convert these gray images into BW images and count the number of pixels whose intensity values is greater than the threshold value for each frame. Then we stored this data into an array format for all frames.

Step 3 and 4: After that we calculated mean and standard deviation of the pixel count for each video. And plotted meltpool area in terms of pixels count exceeding the threshold value against Frames (time).

Step 5: We plotted similar graphs for individual tracks (Both Type-I and Type-II) segregated from the video file using the above steps. In this analysis we considered two cases:

- i. When frames where laser was off during the process have been included
- ii. When frames where laser was off during the process were not included

We also performed a separate analysis just for video 1 to show the effects when this method was applied directly to gray image (without converting to BW Image).

6.2 Spatial Principal Component Analysis

In spatial principal component analysis, the initial steps remain the same as temporal PCA. Transformation of a three-dimensional array i.e. $\mathcal{U} \in \mathbb{R}^{(M \times N) \times J}$ is transformed into a matrix $\in \mathbb{R}^{p \times J}$, where $p = M \times N$. Here each row of the matrix consists of a vectorized frame. Principal components generated through vectorized PCA associates a weight to each pixel (see Fig. 19).

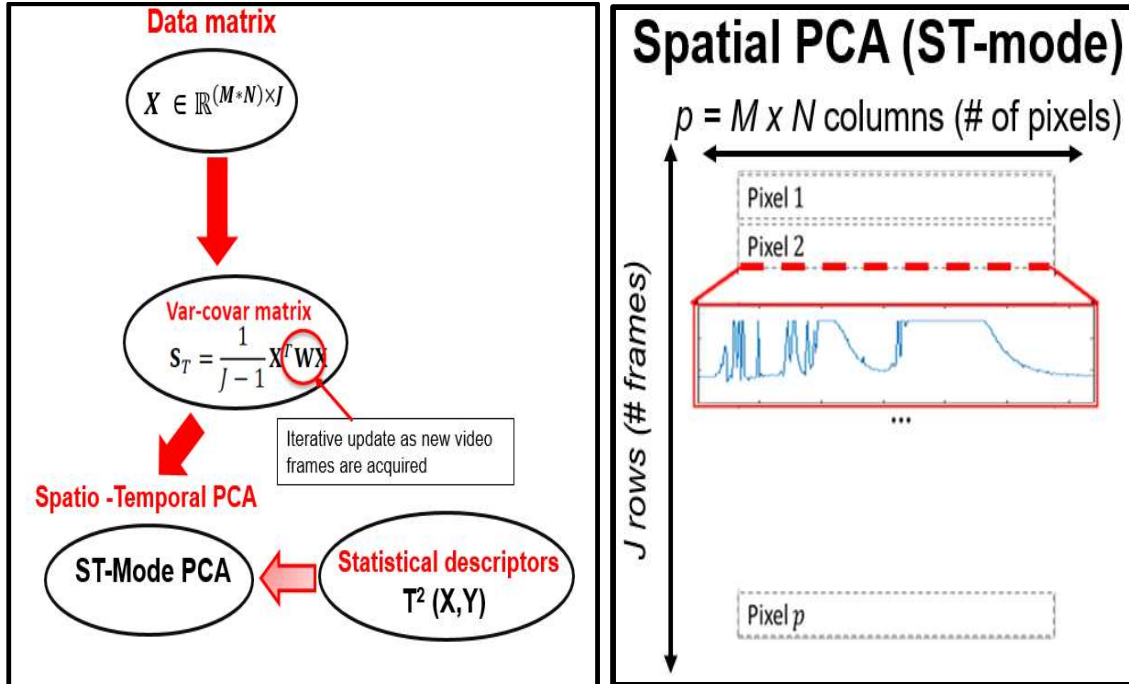


Figure 19: Statistical analysis methodology for spatial PCA.

A new term W is added while doing the spectral decomposition which represents the addition of frames as new videos are being recorded and added by using the experimental setup.

6.3 Spatial Mapping

A statistical descriptor based upon Hotelling's T^2 distance which is a spatial index i.e. a function $T^2(X, Y)$ of pixel location within the image which maps a T^2 value to each pixel is added. Then a three-dimensional map is plotted using this T^2 values against the pixel location. T^2 values are based upon all principal components but it can be restricted to a few Principal Components which contribute most to the video file without any loss of information.

CHAPTER 7

RESULTS

In this Chapter, we present the results obtained from temporal and spatial statistical analysis of high frame rate videos. At first the videos are analyzed without removing frames that represent “laser off condition”. That means that there are certain frames with no laser scanning was performed and as a result the mean gray levels were very low during laser off condition. Later, the frames with laser off conditions have been identified and removed from the videos so that the entire video represents laser scanning and processing during the L-PBF process.

7.1 Temporal Principal Component Analysis

The first set of results are for Video #1 that consisted of 2232 frames and 0.2232 seconds in length (10000 fps, 512 pixels x 128 pixels resolution, with no zoom).

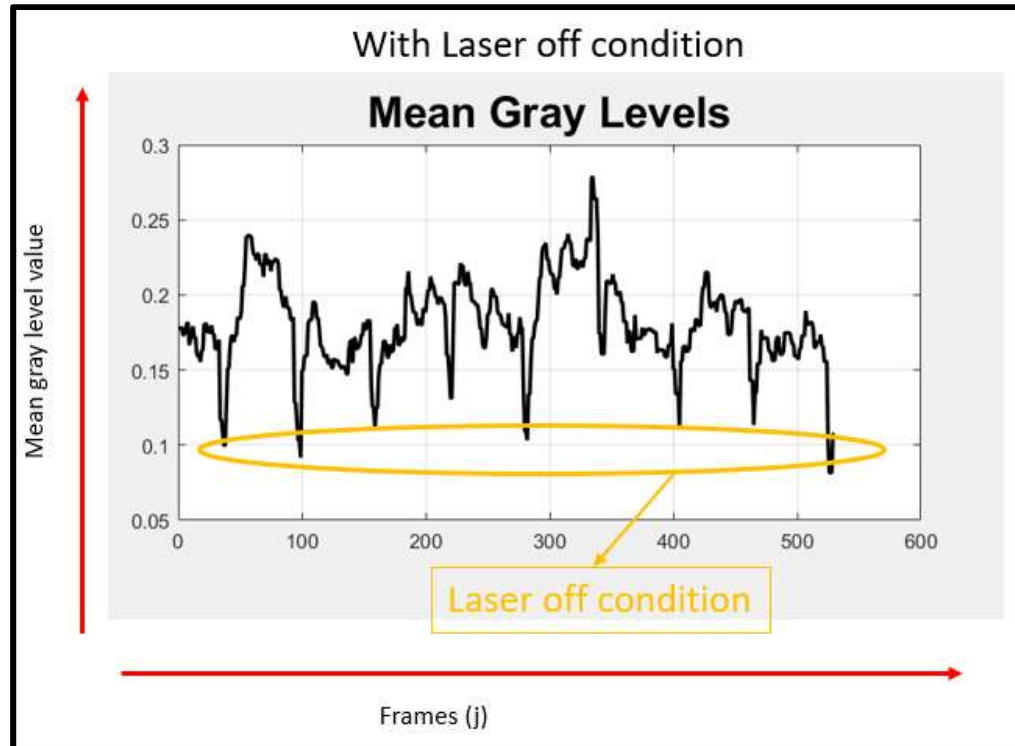


Figure 20: The run sequence plot obtained from temporal PCA.

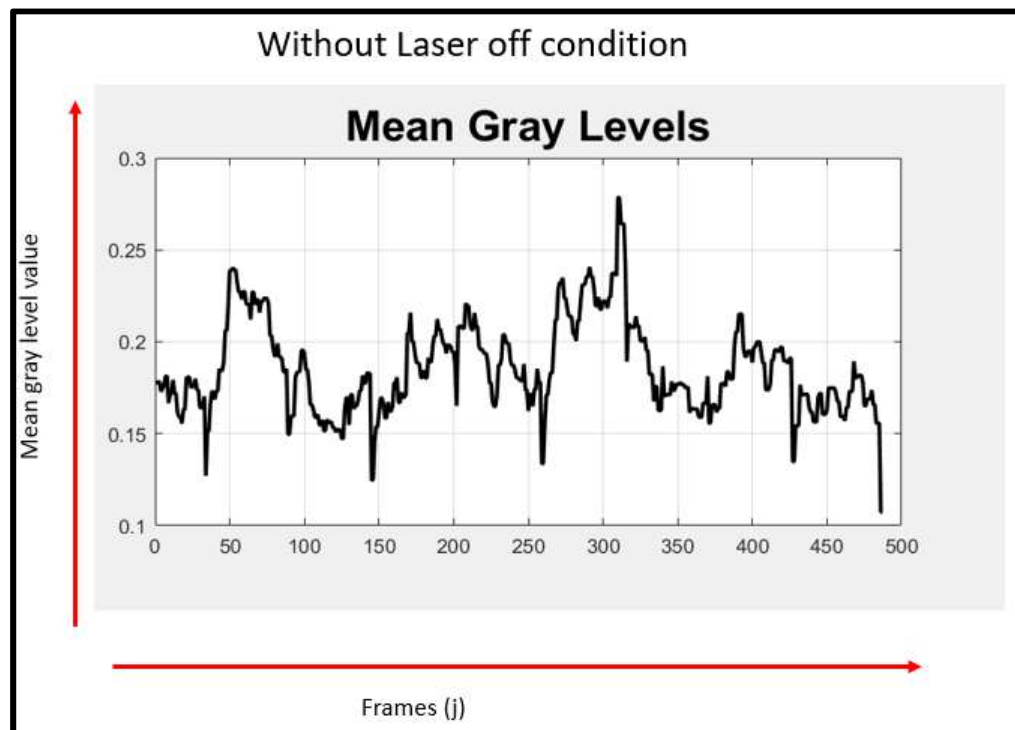


Figure 21: The run sequence plot obtained from temporal PCA.

The temporal PCA graph for two cases were performed for video #1.

1. When frames having laser off condition were include (Fig 20)
2. When frames having laser off conation were not included (Fig 21)

The mean gray level values in case 1 were going as low as 0.1 where as in case 2 it was going till 0.12. This states the fact that by removing the frames with laser off condition the data was cleaned and accurate results can be obtained from further analysis.

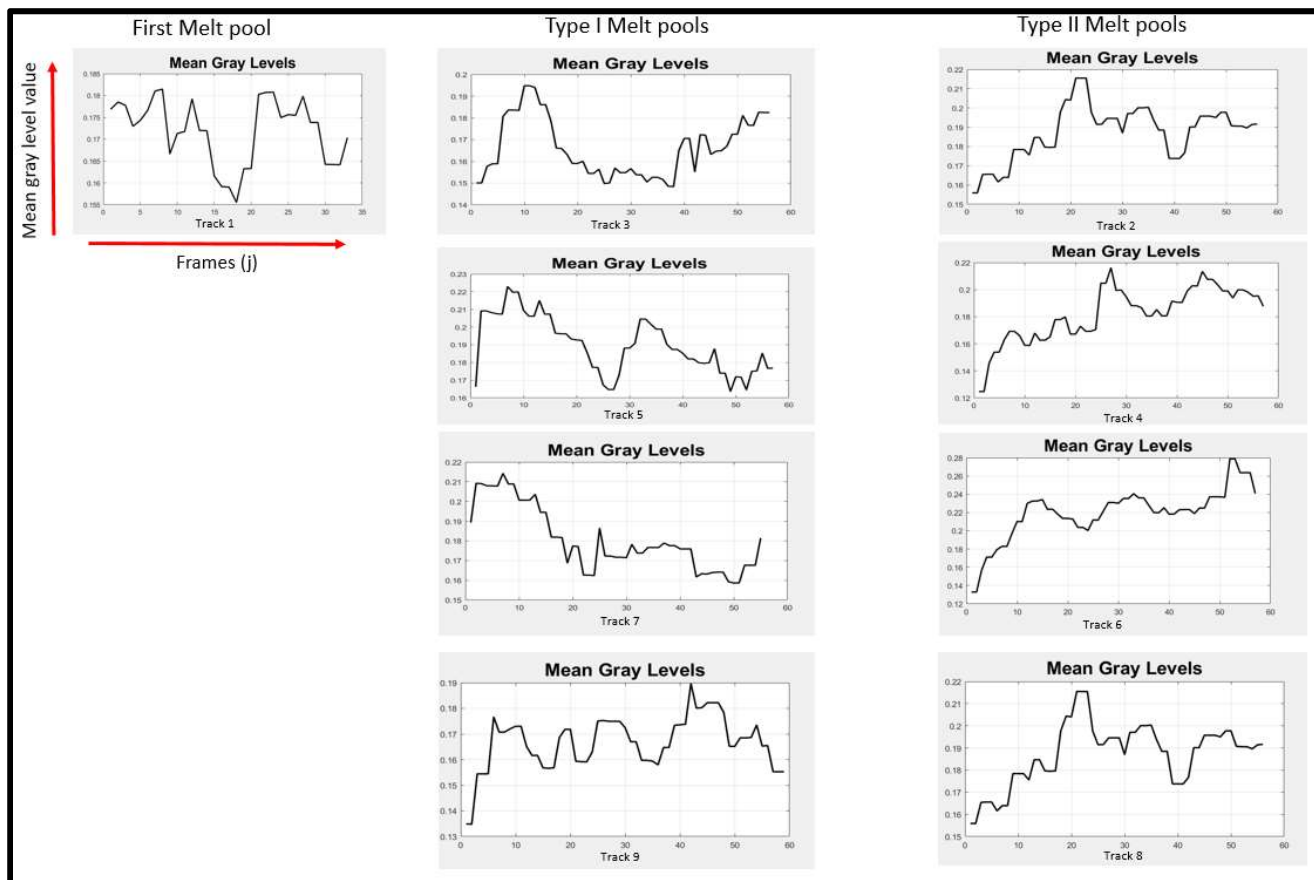


Figure 22: The run sequence plot obtained from temporal PCA for Type-I and Type-II tracks.

After segregating frames from the original video into different tracks and performing the Temporal analysis, the mean gray values for Type-I tracks started from a higher value and got reduced to a lower value as the laser moved, whereas the mean gray level values for Type-II tracks started from a lower value and increased later. This supports the fact that Type-I tracks were still within the heat-affected zone of the previous hatch scanning and Type-II tracks were no longer affected by the heat from laser scanning of the previous track or hatch during the process as stated by Criaes et al. 2017.

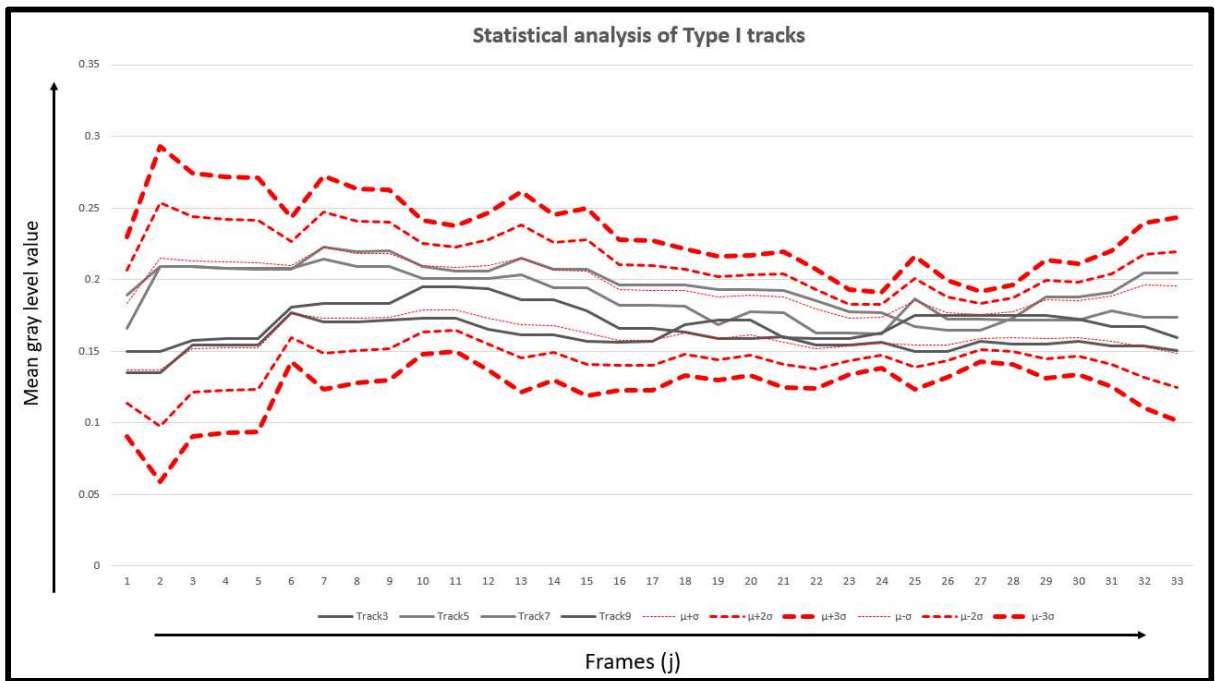


Figure 23: Statistical analysis of Type-I tracks.

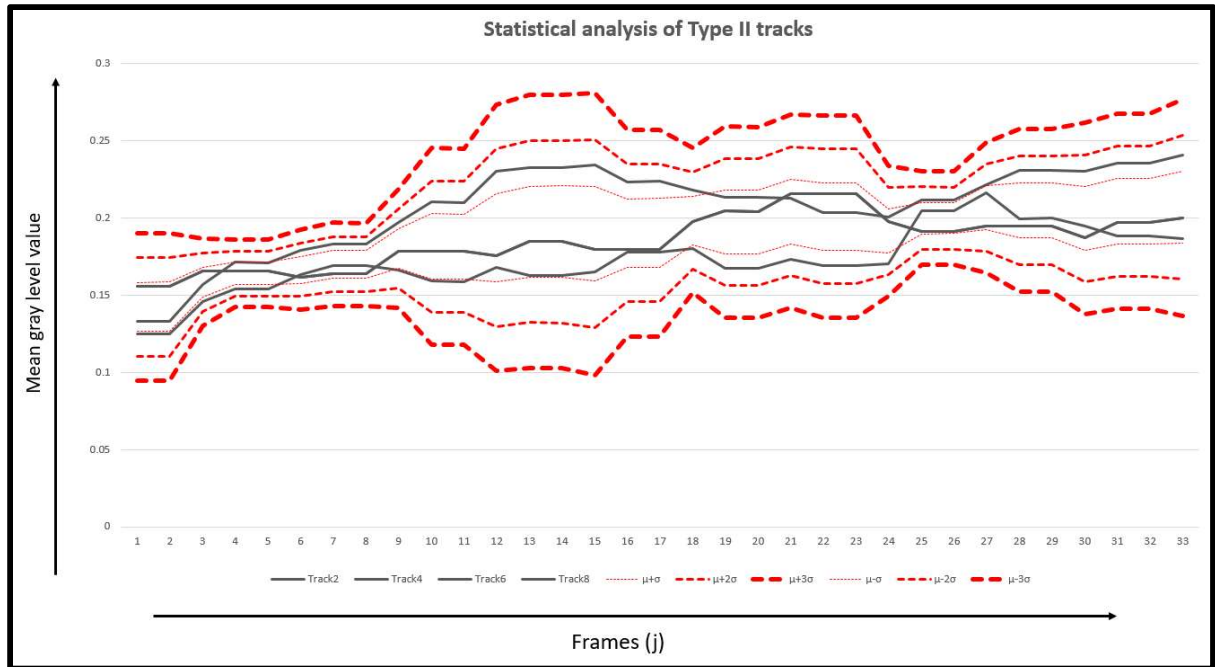


Figure 24: Statistical analysis of Type-II tracks.

Fig 23 and Fig 24 were results obtained after performing a statistical analysis of Type-I and Type-II tracks which includes calculation of mean and standard deviation of the mean gray level values as the laser processes each track. It can be inferred from these statistical graphs that the process goes out of control for the range between $\mu+\sigma$ and $\mu-\sigma$ whereas it remains within the limit for a range between $\mu+2\sigma$ and $\mu-2\sigma$. These results can be used for setting up control limits as an in-situ process monitoring technique which can in turn be used to identify defects and minimize them by altering the process parameters to obtain high quality products.

The results were also obtained for Video #2 and #4 to support this theory as shown in below figures.

The second set of results are for Video #2 that consisted of 2408 frames and 0.1003 seconds in length (24000 fps, 512 pixels x 128 pixels resolution, with no zoom). The temporal analysis results for Video #2 are given in Figs. 25-27.

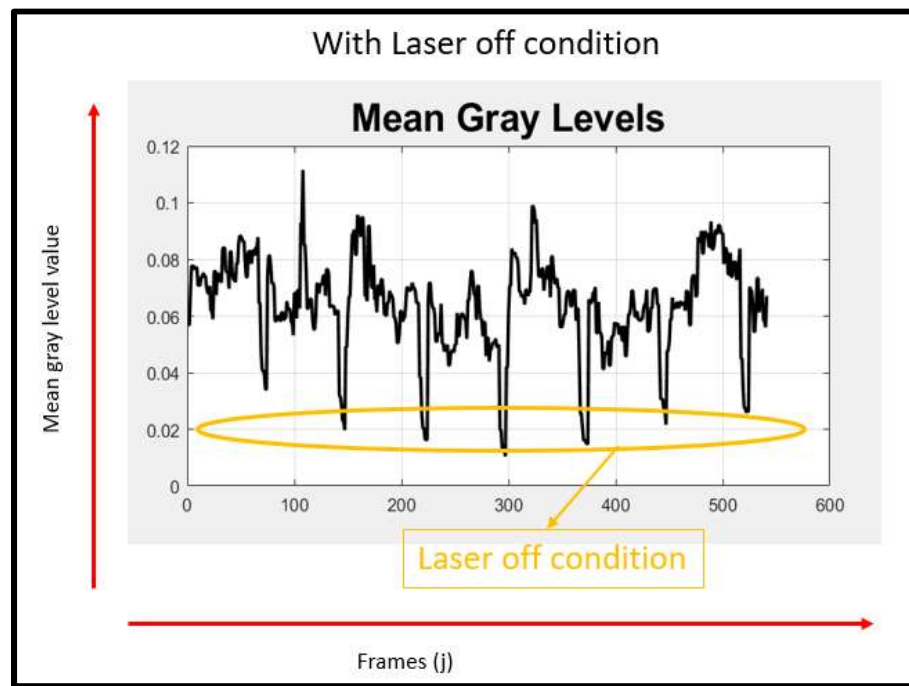


Figure 25: The run sequence plot obtained from temporal PCA.

Figure 10 displays nine line plots arranged in a 3x3 grid, showing the Mean Gray Levels (Y-axis) versus Frames (j) (X-axis) for different melt pool types. The plots are organized as follows:

- Top Row:**
 - First Melt pool (Track 1):** Shows a fluctuating mean gray level, generally increasing from approximately 0.055 to 0.085 over 70 frames.
 - Type I Melt pools (Track 3):** Shows a fluctuating mean gray level, generally increasing from approximately 0.05 to 0.09 over 70 frames.
 - Type II Melt pools (Track 2):** Shows a fluctuating mean gray level, generally increasing from approximately 0.06 to 0.11 over 70 frames.
- Middle Row:**
 - Type I Melt pools (Track 5):** Shows a fluctuating mean gray level, generally increasing from approximately 0.04 to 0.09 over 70 frames.
 - Type II Melt pools (Track 4):** Shows a fluctuating mean gray level, generally increasing from approximately 0.045 to 0.075 over 70 frames.
- Bottom Row:**
 - Type I Melt pools (Track 7):** Shows a fluctuating mean gray level, generally increasing from approximately 0.045 to 0.085 over 70 frames.
 - Type II Melt pools (Track 6):** Shows a fluctuating mean gray level, generally increasing from approximately 0.045 to 0.075 over 70 frames.

A red arrow on the left indicates the 'Mean gray level value' increasing upwards. A red arrow at the bottom indicates 'Frames (j)' increasing to the right.

Figure 27: The run sequence plot obtained from temporal PCA for Type-I and Type-II tracks.

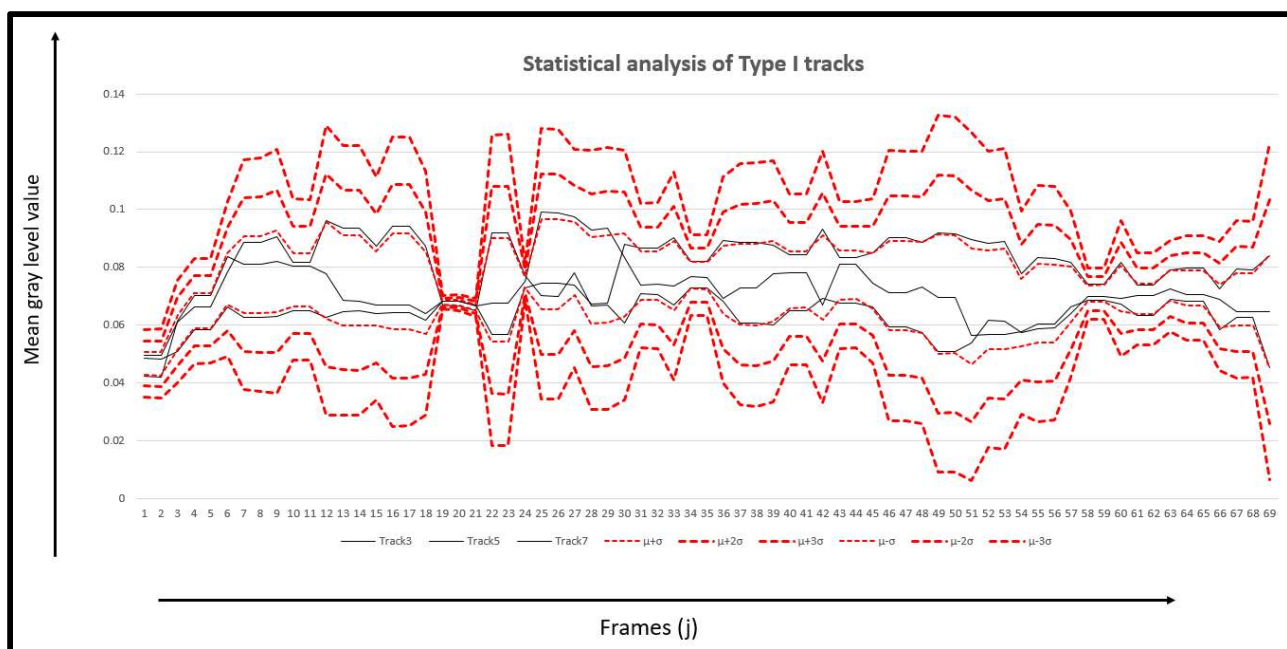


Figure 28: Statistical analysis of Type-I tracks.

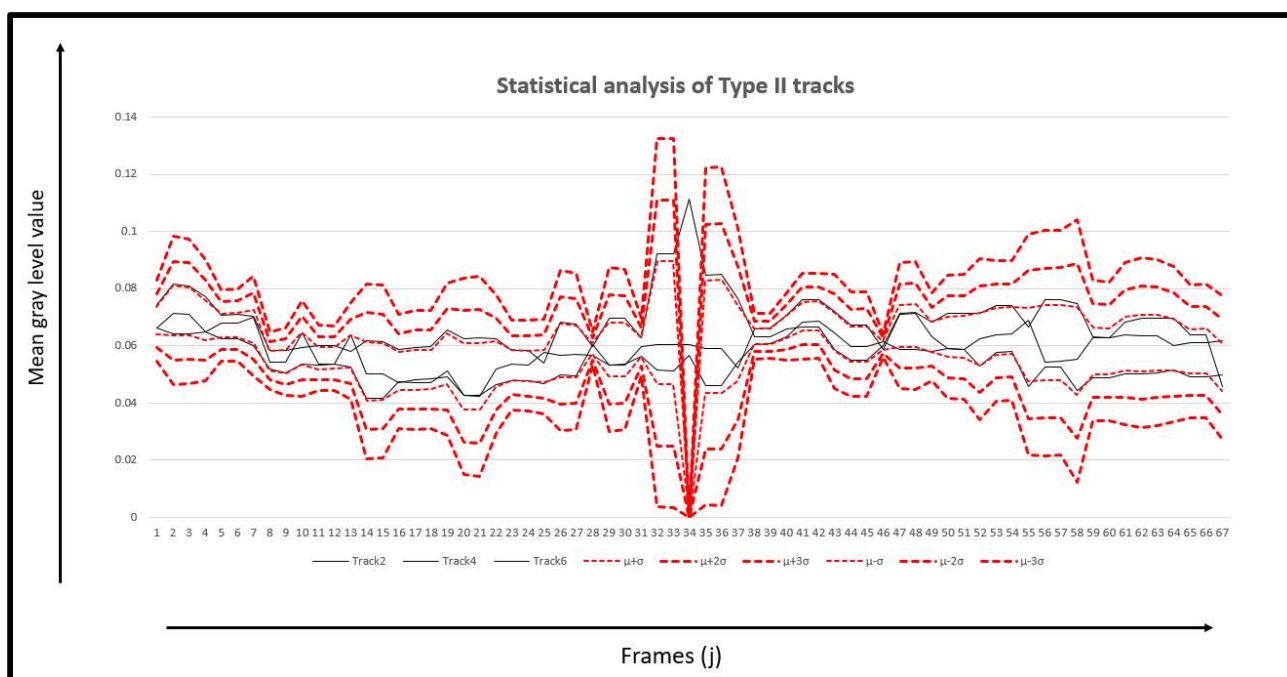


Figure 29: Statistical analysis of Type-II tracks.

The third set of results are for Video #4 that consisted of 49869 frames and 2.0779 seconds in length (24000 fps, 512 pixels x 128 pixels resolution, with X1 zoom).

The results of temporal analysis for Video #4 are given in Figs. 30-32.

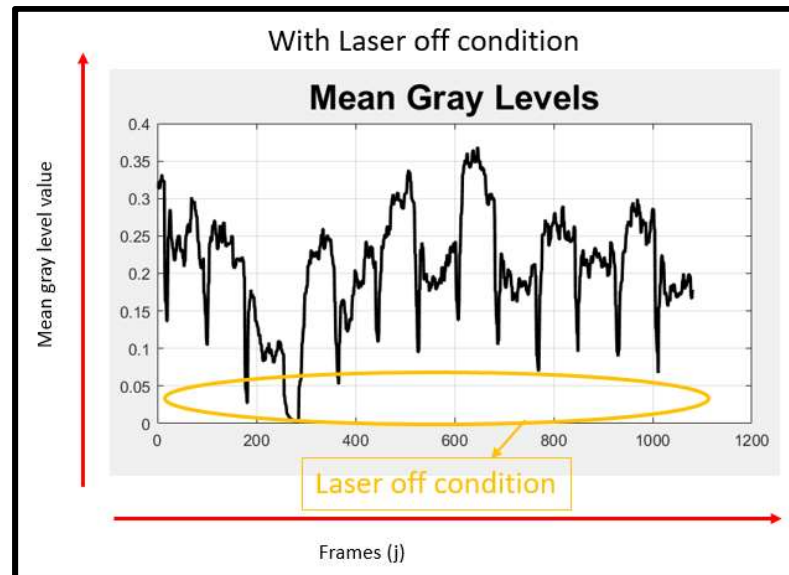


Figure 30: The run sequence plot obtained from temporal PCA.

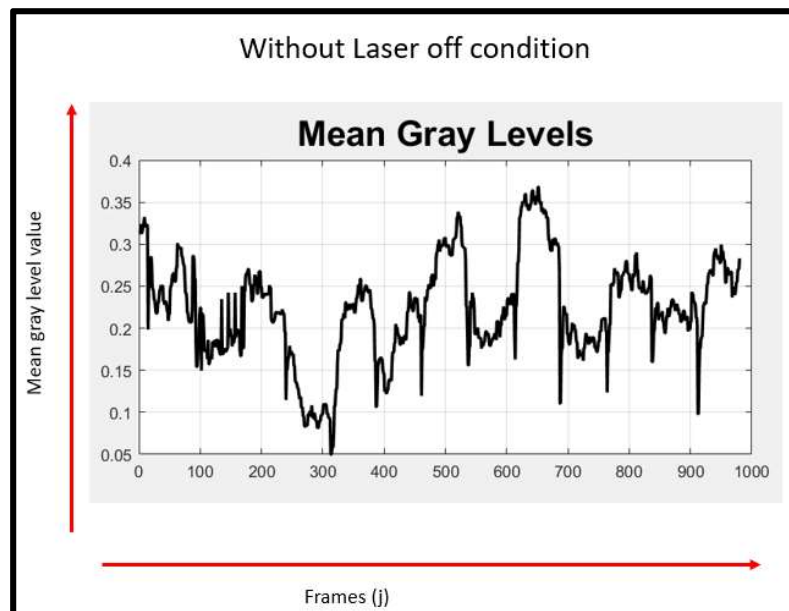


Figure 31: The run sequence plot obtained from temporal PCA.

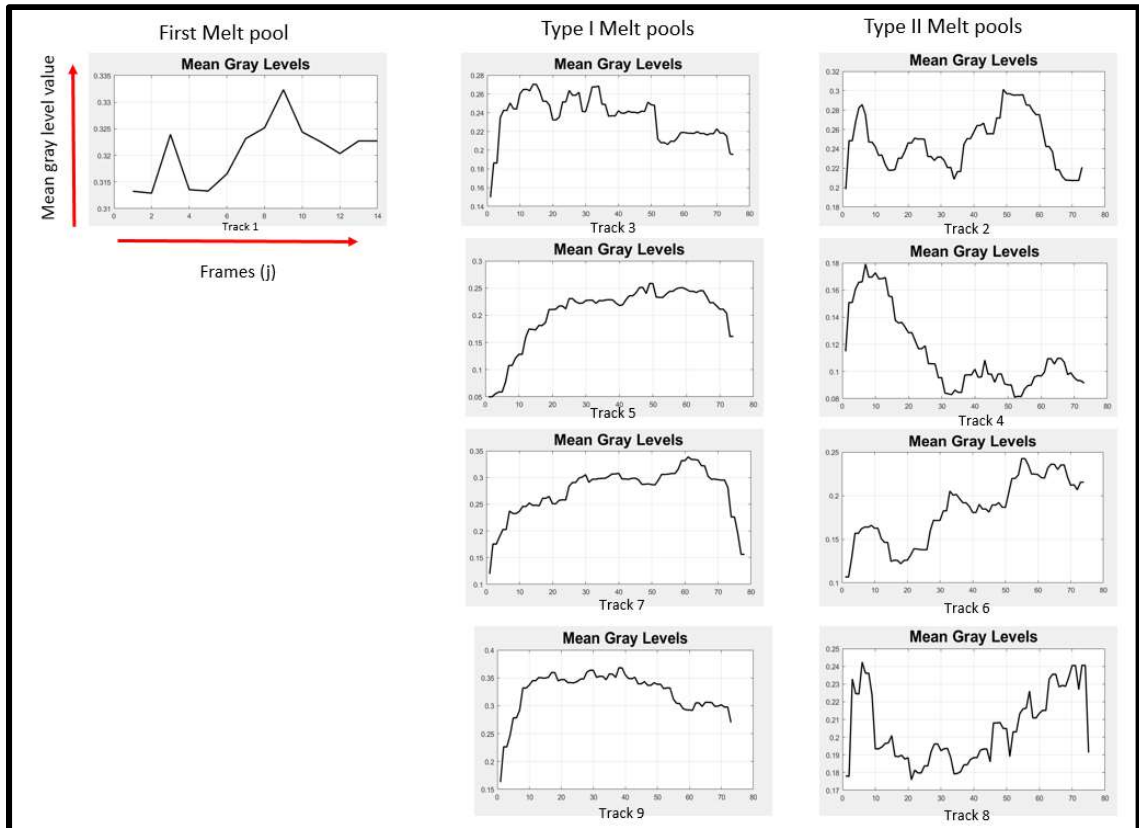


Figure 32: The run sequence plot obtained from temporal PCA for Type-I and Type-II tracks.

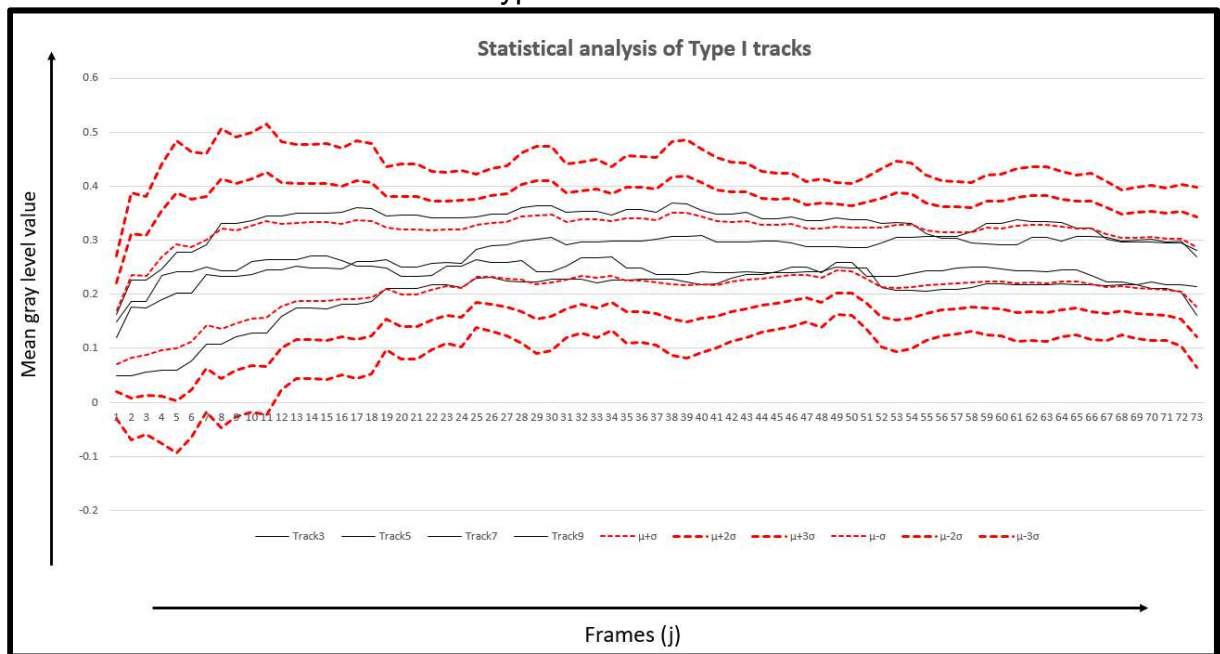


Figure 33: Statistical analysis of Type-I tracks.

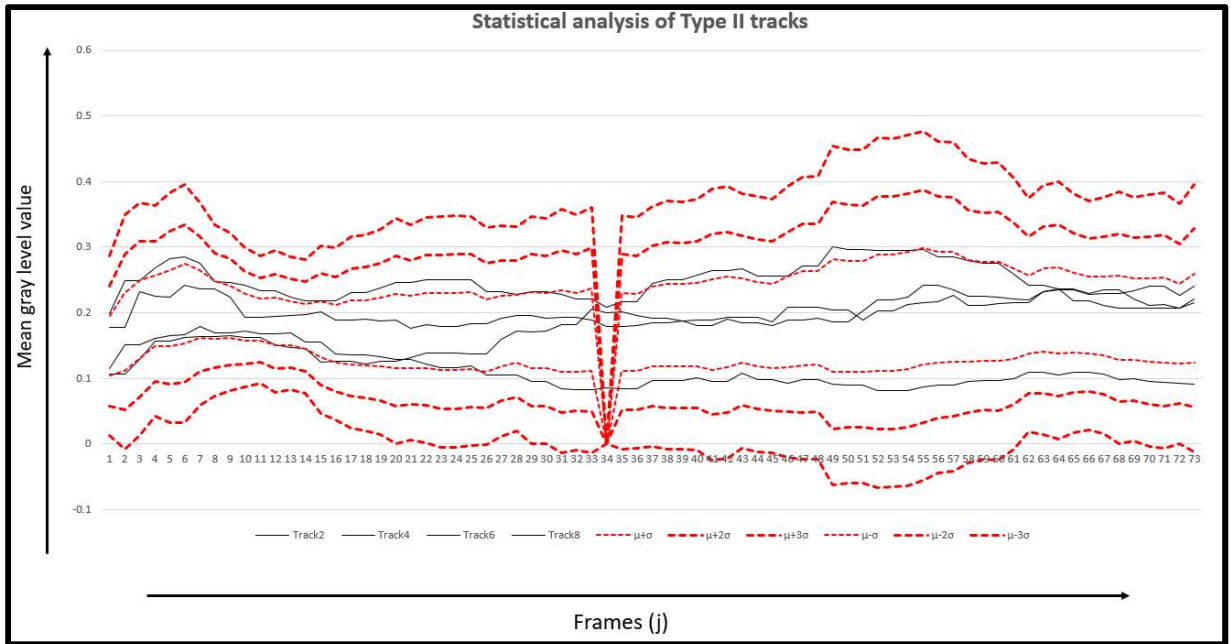


Figure 34: Statistical analysis of Type-II track.

7.2 Meltpool Area Analysis

In this section, we present results from meltpool area analysis. The pixels with values exceeding the specified threshold value are counted to represent the meltpool area that also includes spattered pixels. These graphs are presented as number of pixels versus frames (in other words versus the time).

The first set of results are for Video #1 that consisted of 2232 frames and 0.2232 seconds in length (10000 fps, 512 pixels x 128 pixels resolution, with no zoom).

Case 1: When frames where laser was off during the process have been included

Case 2: When frames where laser was off during the process were not included

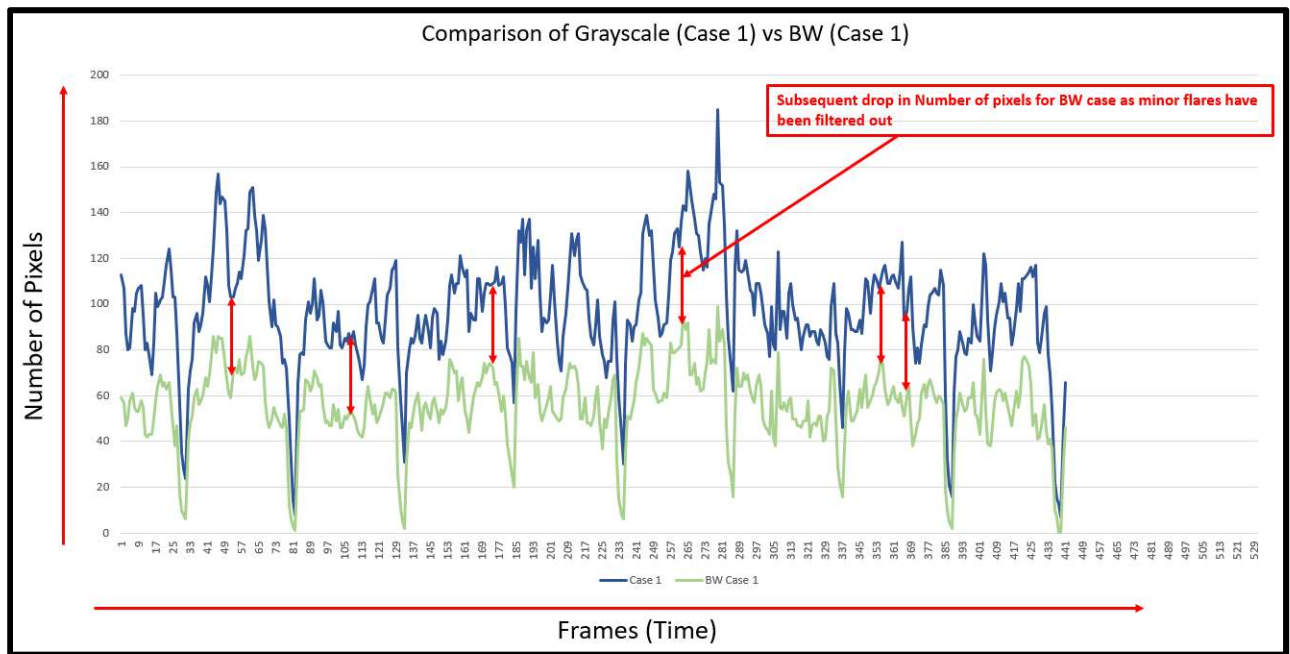


Figure 35: Comparison of Case 1 when RGB images were converted to gray images and BW images.

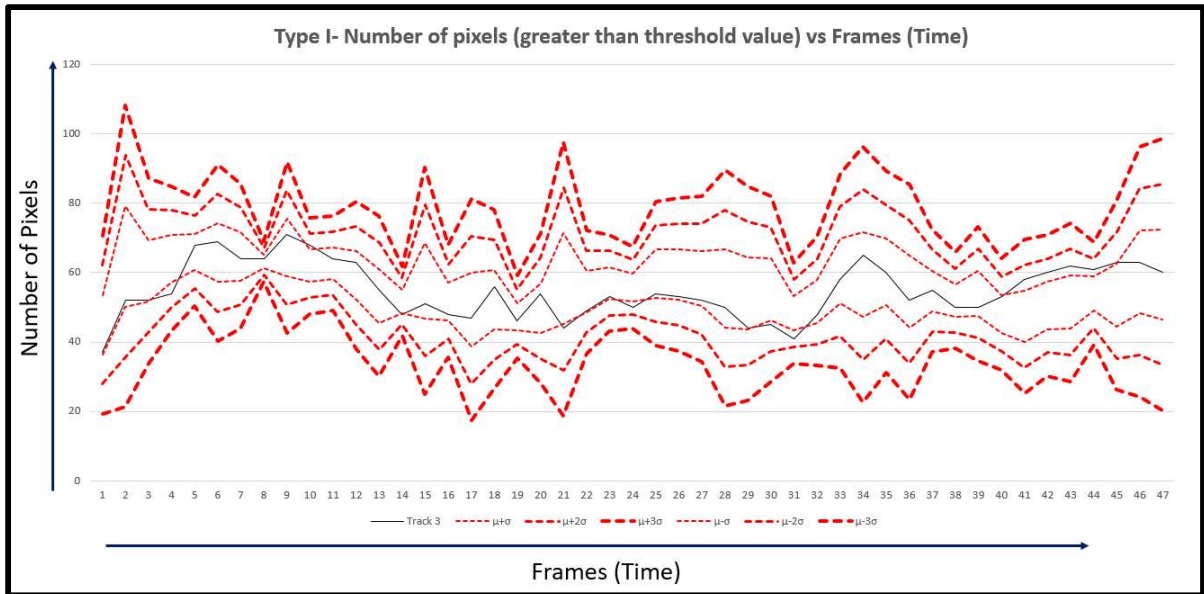


Figure 36: Statistical analysis of Melpool area in terms of # of pixels of Type-I Track 3.

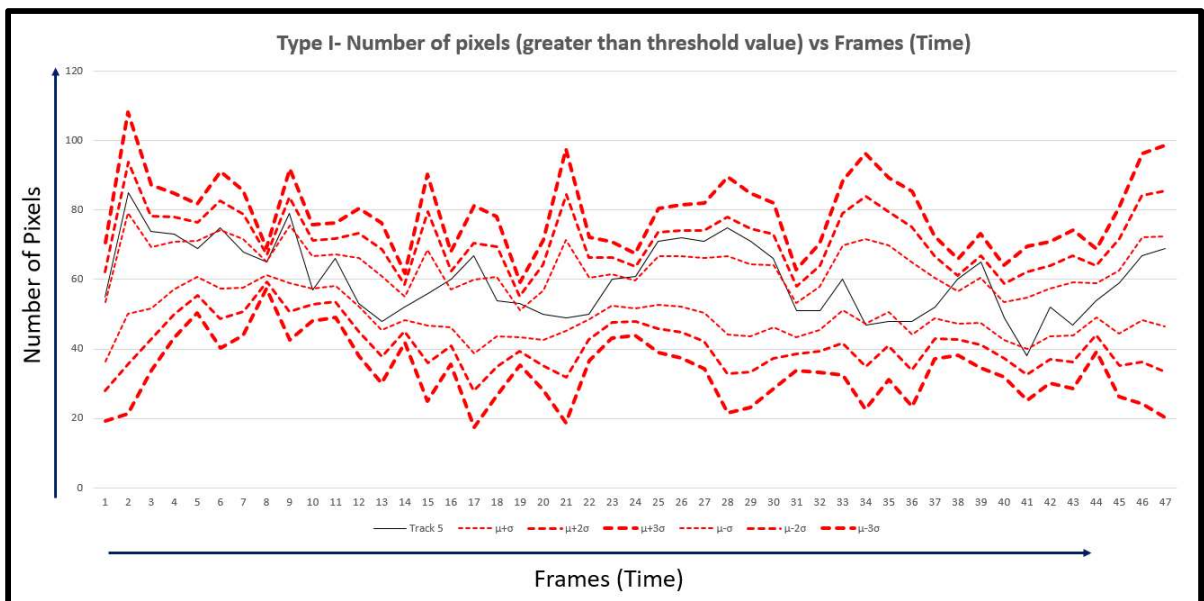


Figure 37: Statistical analysis of Melpool area in terms of # of pixels of Type-I Track 5.

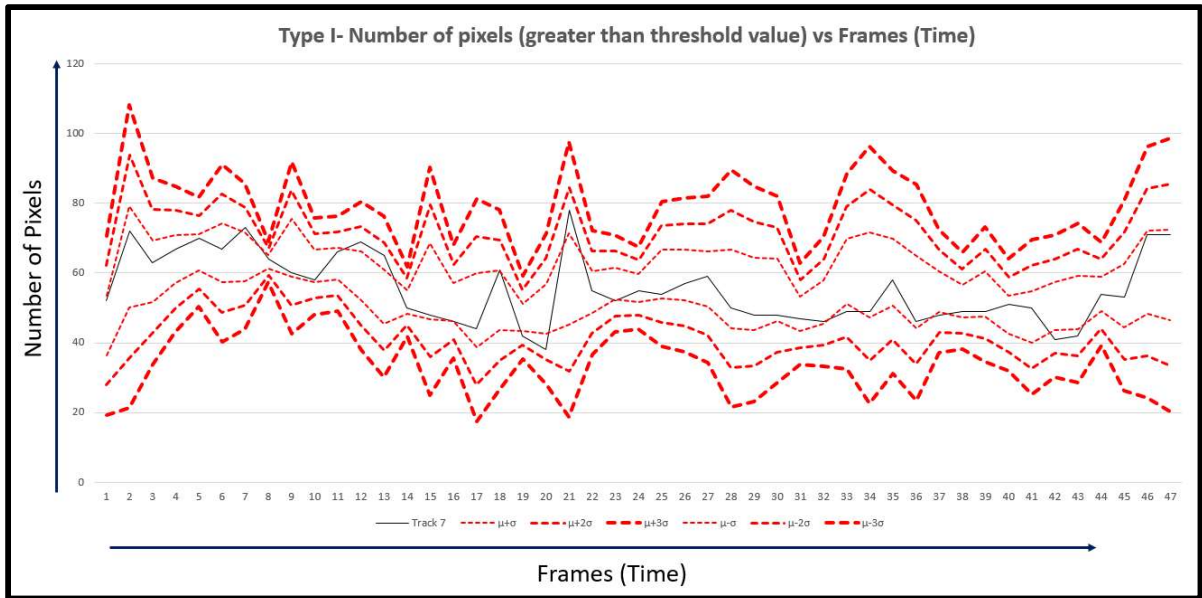


Figure 38: Statistical analysis of Melpool area in terms of # of pixels of Type-I Track 7.

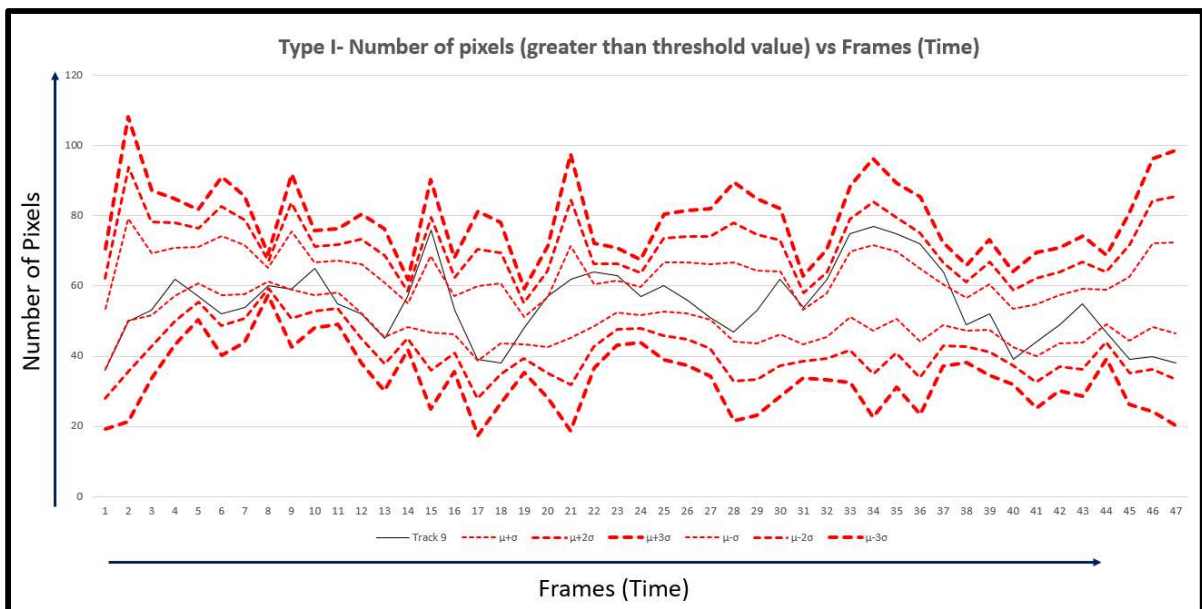


Figure 39: Statistical analysis of Melpool area in terms of # of pixels of Type-I Track 9.

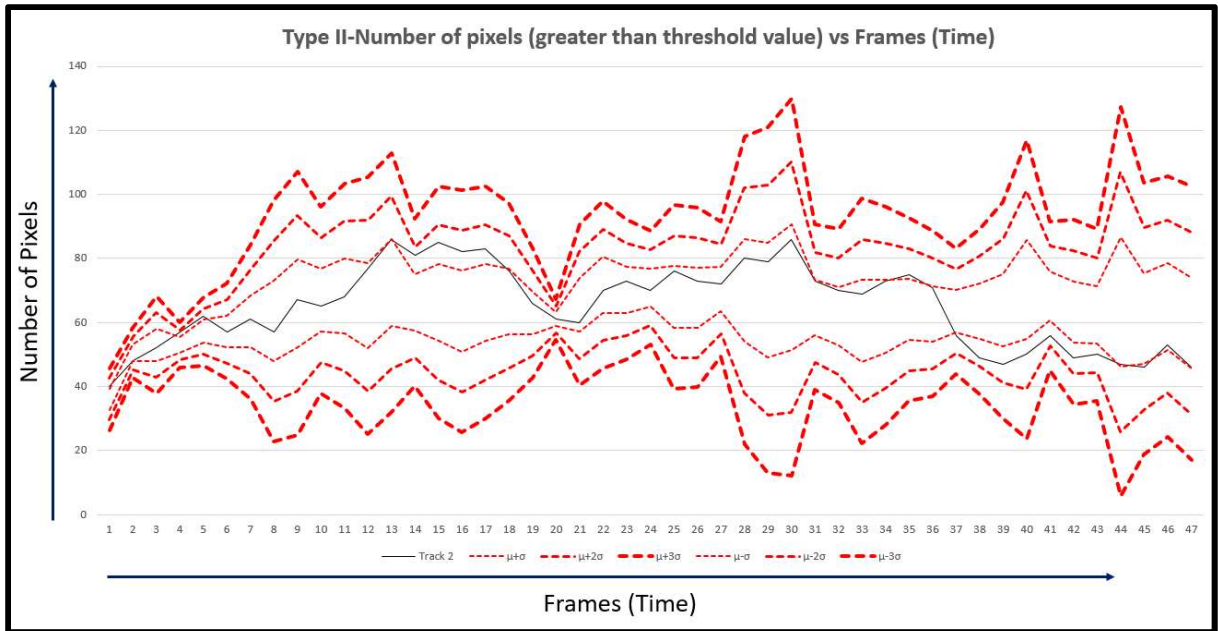


Figure 40: Statistical analysis of Melpool area in terms of # of pixels of Type-II Track 2.

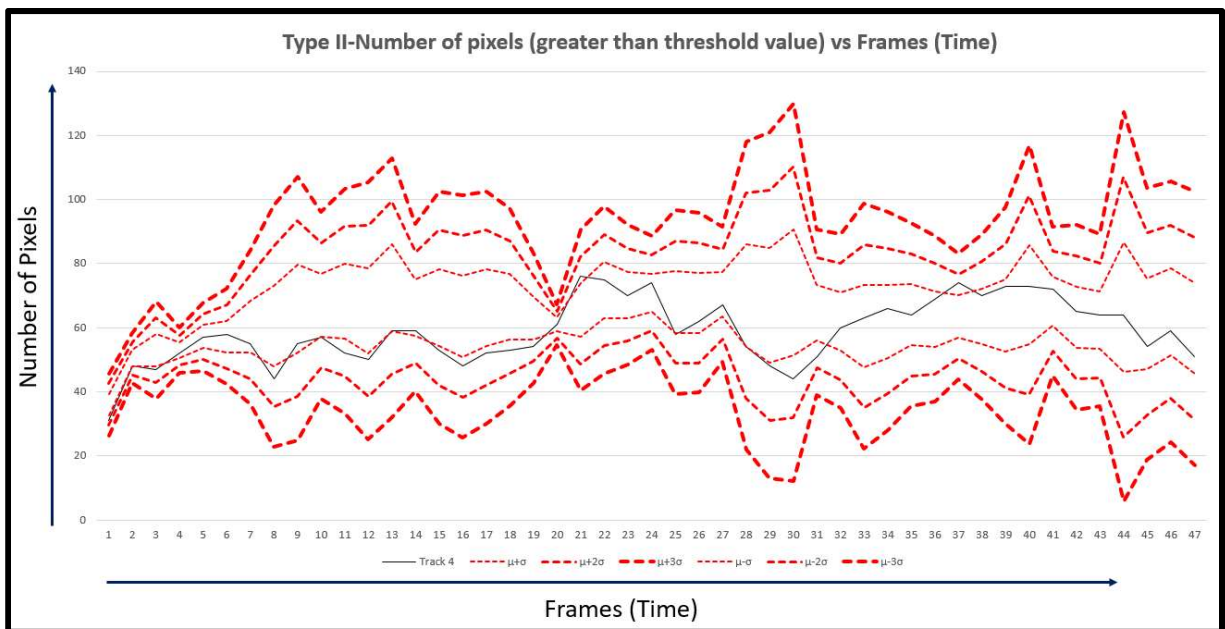


Figure 41: Statistical analysis of Melpool area in terms of # of pixels of Type-II Track 4.

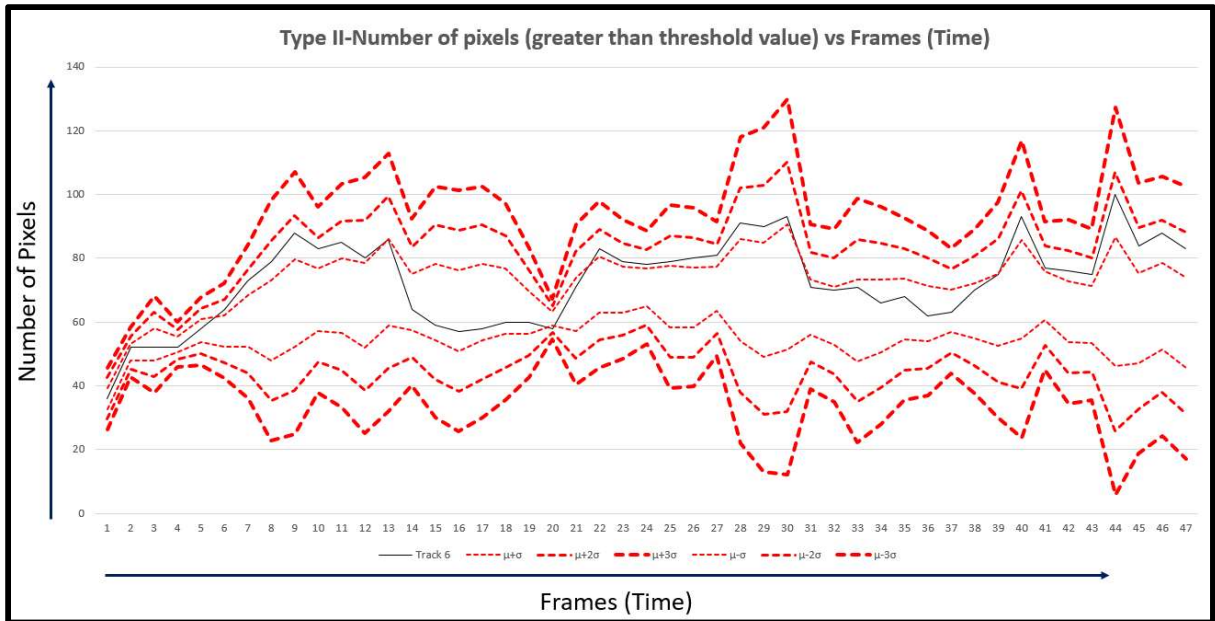


Figure 42: Statistical analysis of Melpool area in terms of # of pixels of Type-II Track 6.

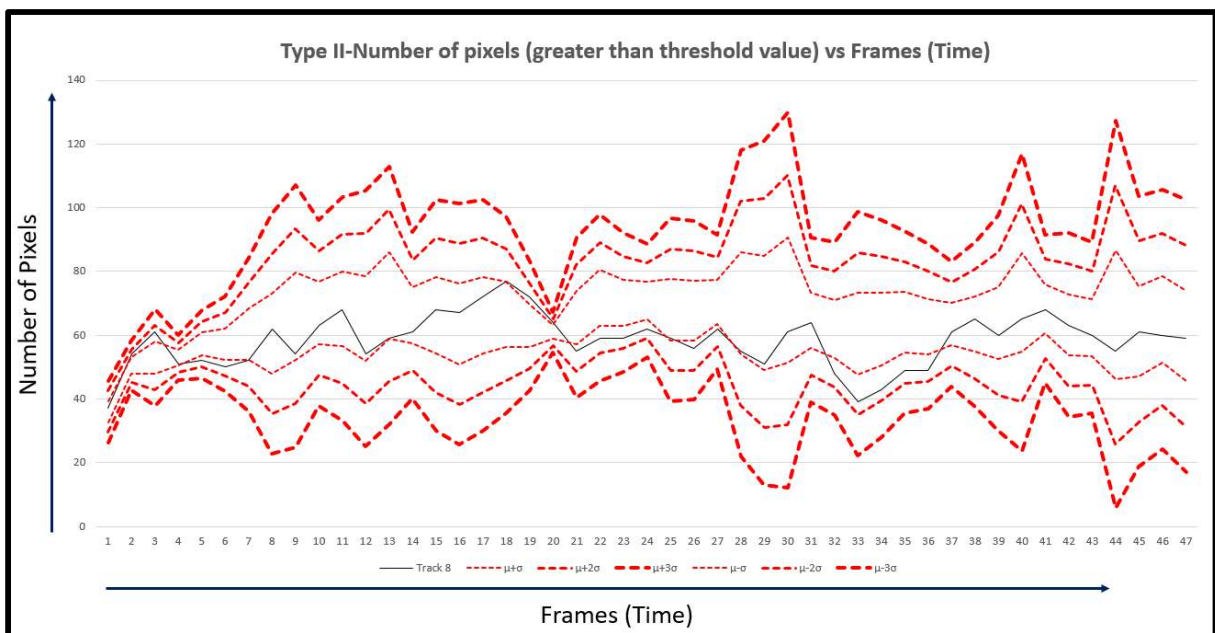


Figure 43: Statistical analysis of Melpool area in terms of # of pixels of Type-II Track 8.

The second set of results are for Video #2 that consisted of 2408 frames and 0.1003 seconds in length (24000 fps, 512 pixels x 128 pixels resolution, with no zoom).

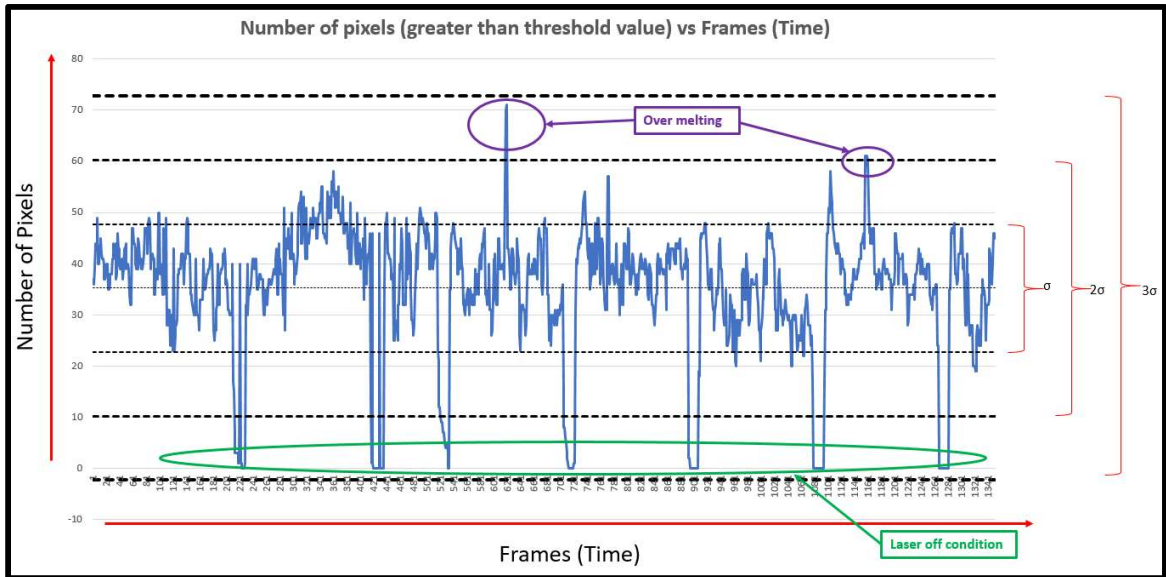


Figure 44: Statistical analysis of Meltpool area in terms of # of pixels when frames having laser off time included.

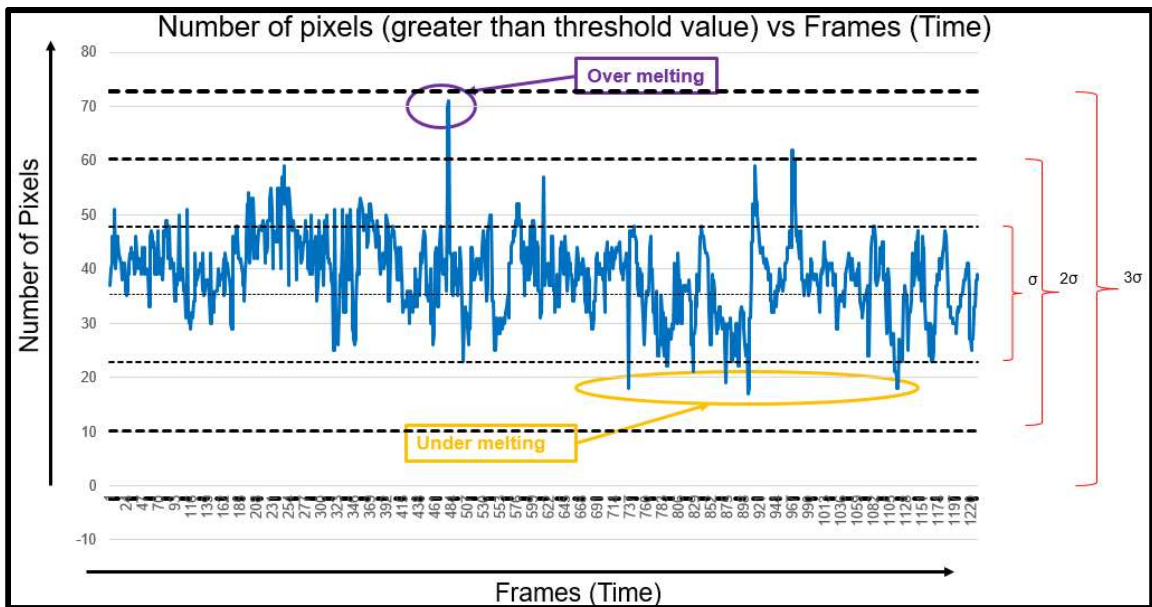


Figure 45: Statistical analysis of Meltpool area in terms of # of pixels when frames having laser off time not included.

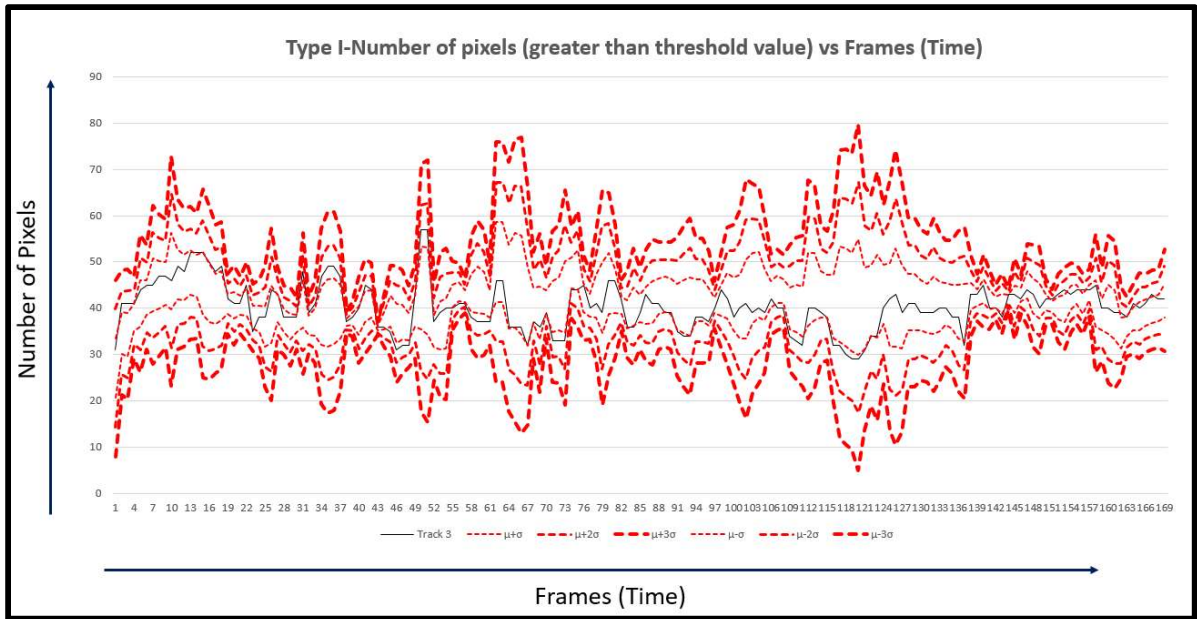


Figure 46: Statistical analysis of Melpool area in terms of # of pixels of Type-I Track 3.

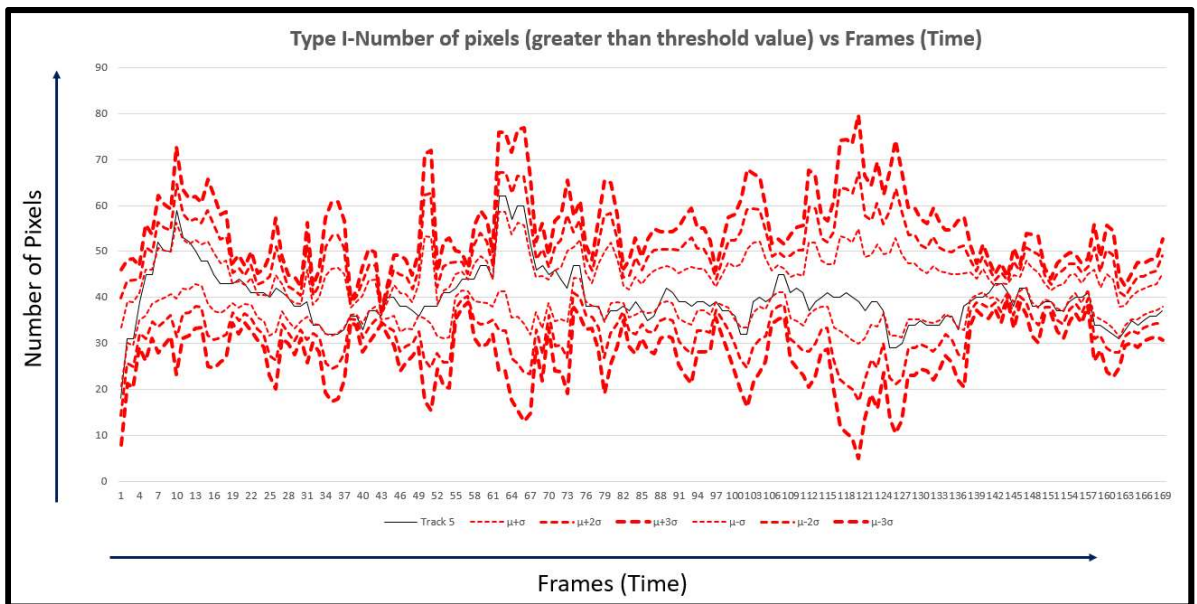


Figure 47: Statistical analysis of Melpool area in terms of # of pixels of Type-I Track 5.

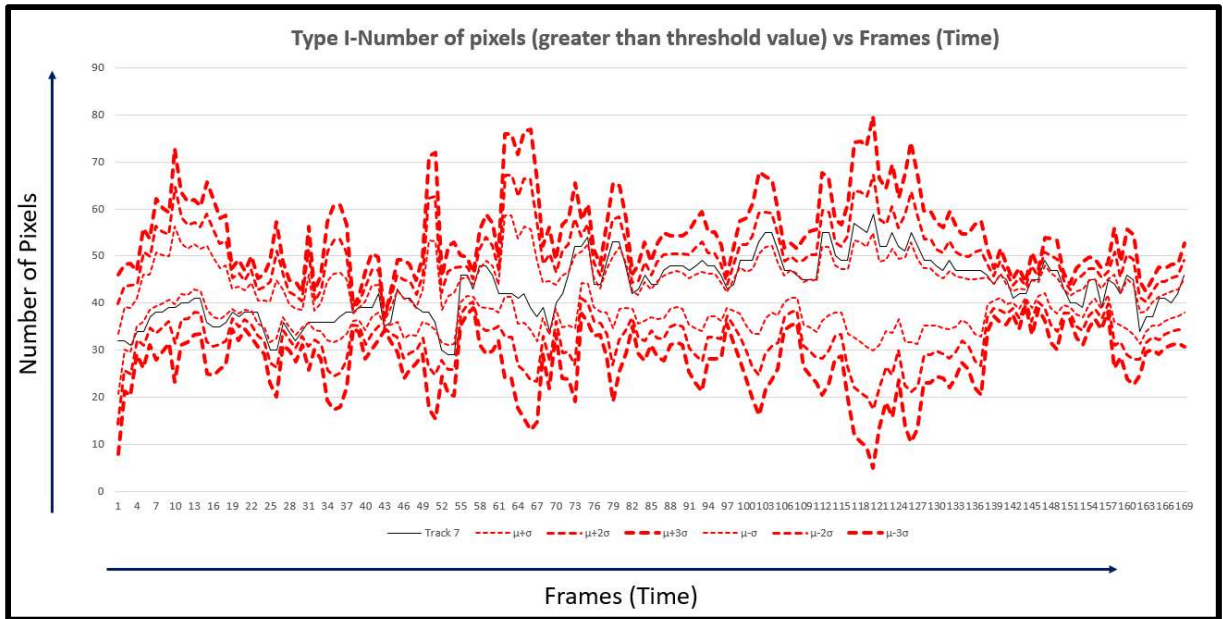


Figure 48: Statistical analysis of Melpool area in terms of # of pixels of Type-I Track 7.

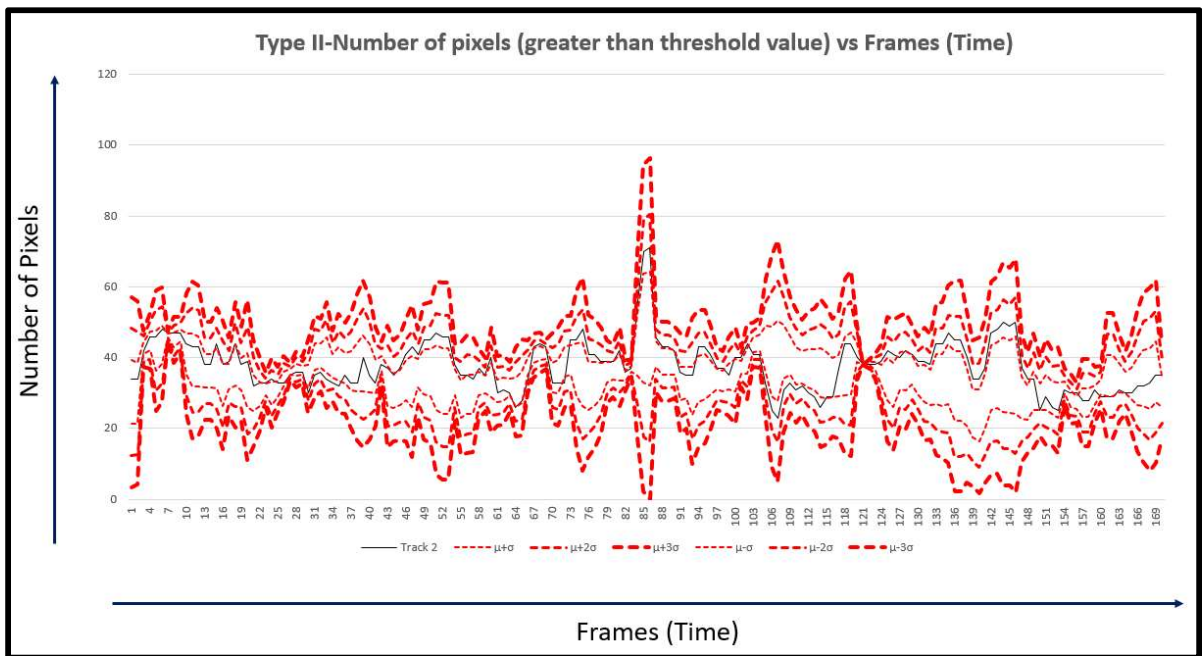


Figure 49: Statistical analysis of Melpool area in terms of # of pixels of Type-II Track 2.

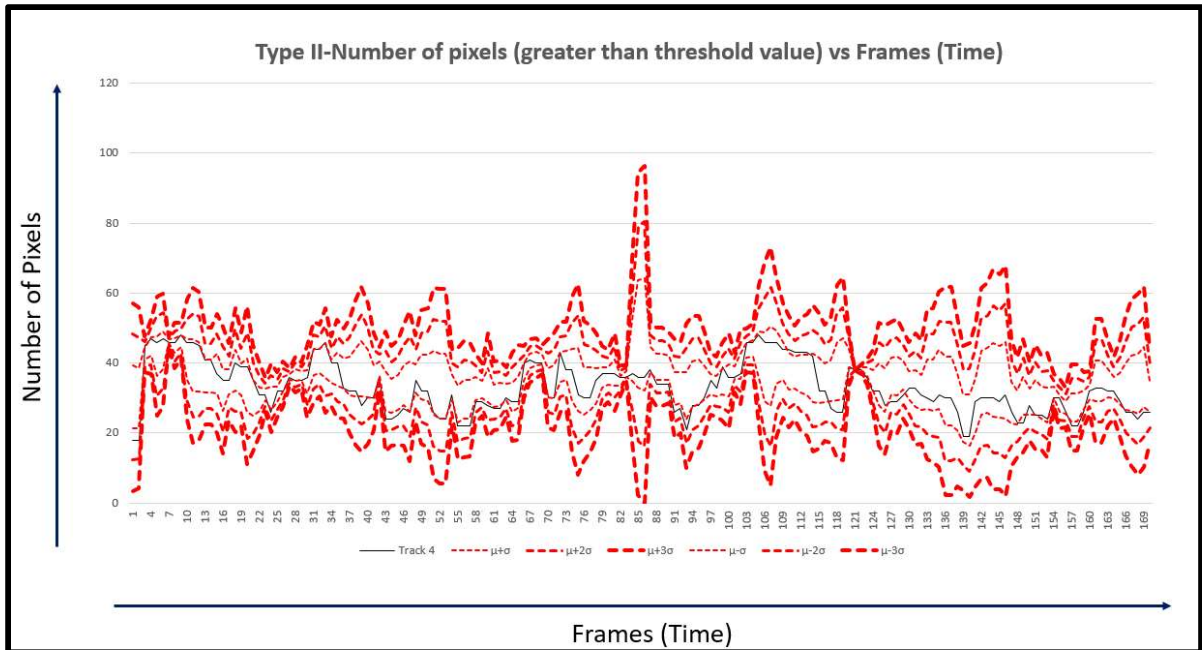


Figure 50: Statistical analysis of Melpool area in terms of # of pixels of Type-II Track 4.

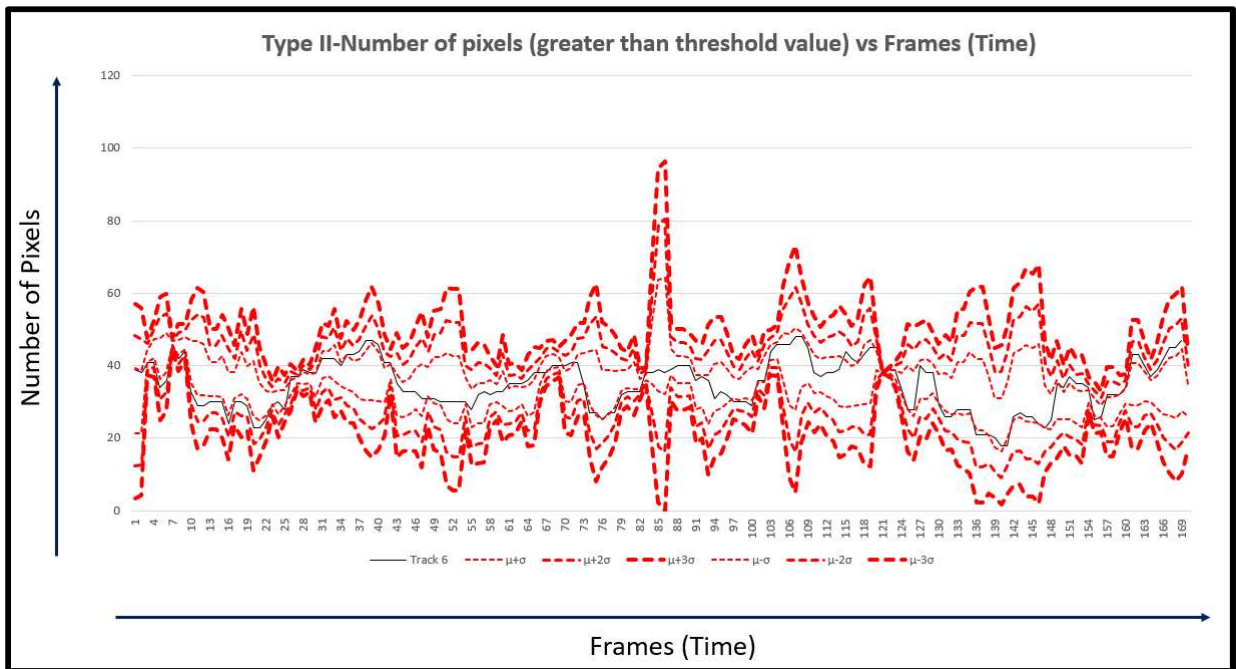


Figure 51: Statistical analysis of Melpool area in terms of # of pixels of Type-II Track 6.

The third set of results are for Video #4 that consisted of 49869 frames and 2.0779 seconds in length (24000 fps, 512 pixels x 128 pixels resolution, with X1 zoom).

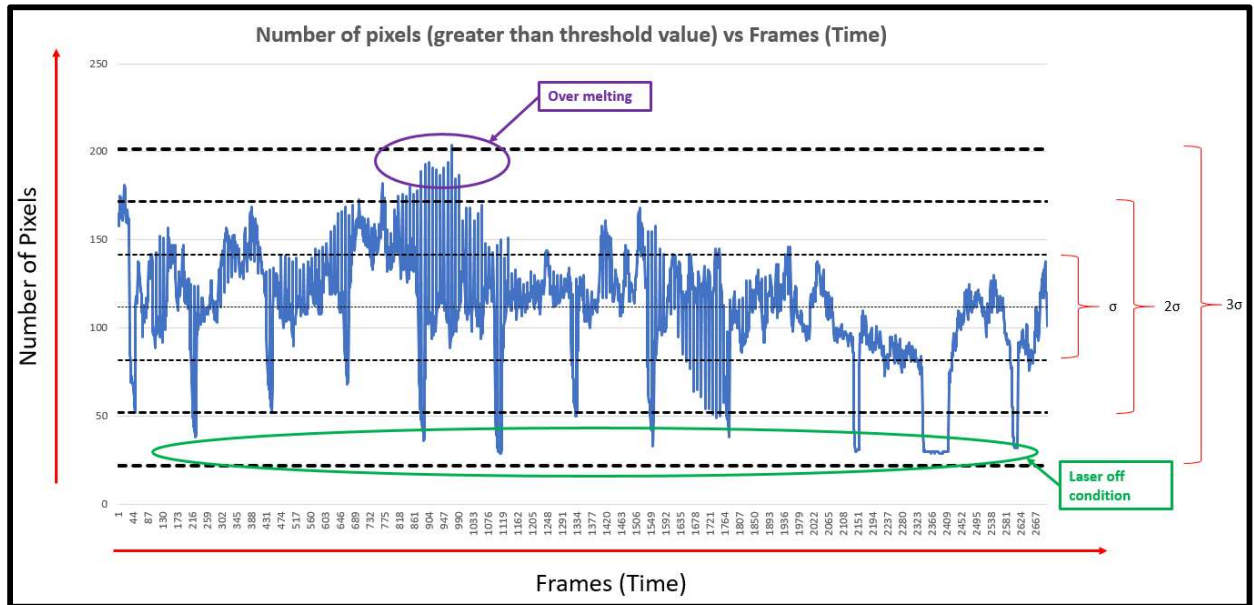


Figure 52: Statistical analysis of Meltpool area in terms of # of pixels when frames having laser off time included.

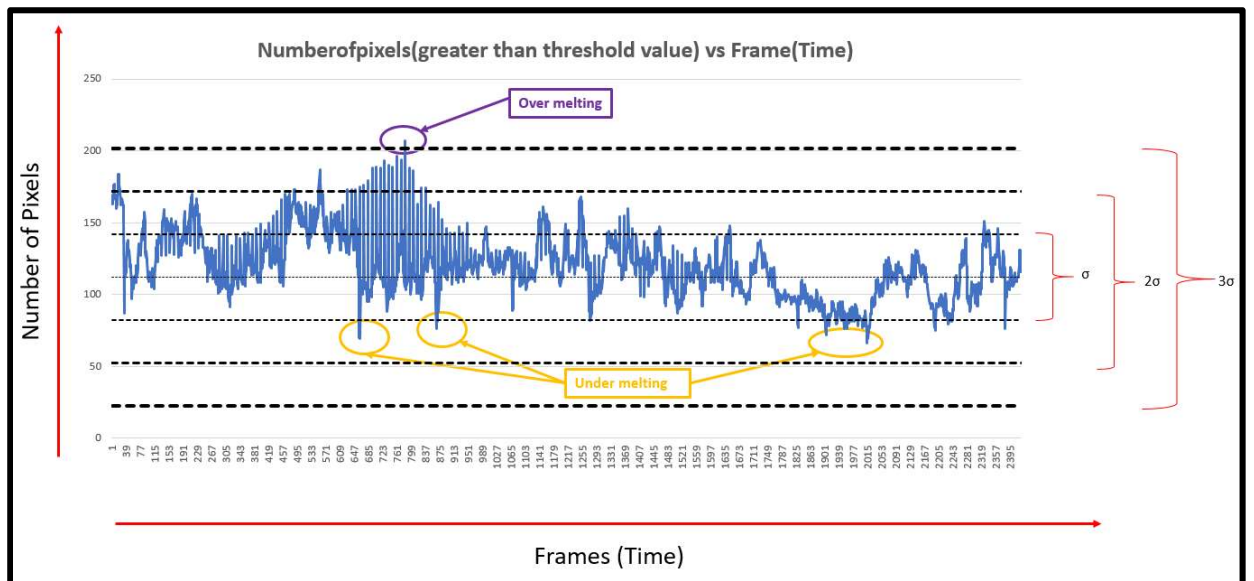


Figure 53: Statistical analysis of Meltpool area in terms of # of pixels when frames having laser off time not included.

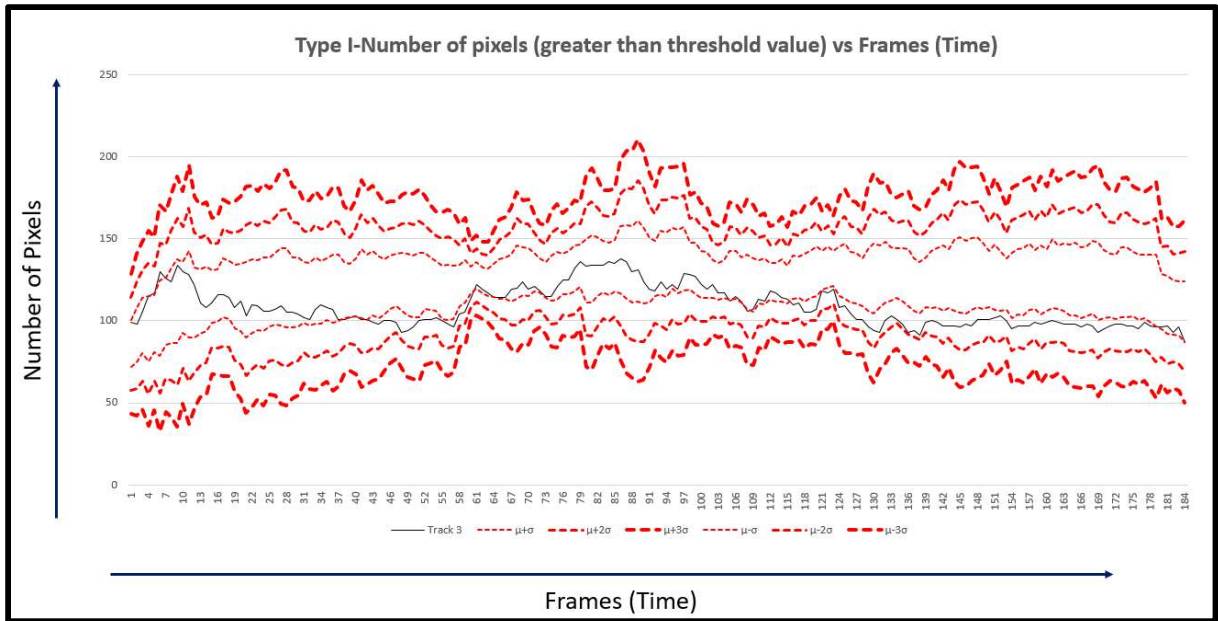


Figure 54: Statistical analysis of Meltpool area in terms of # of pixels of Type-I Track 3.

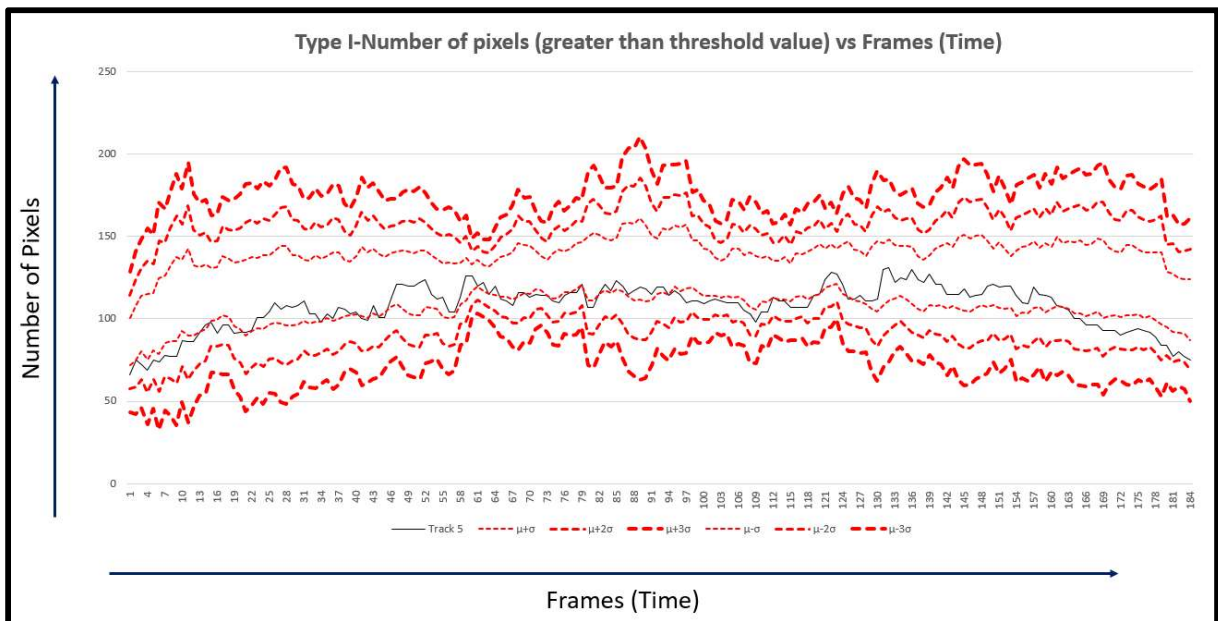


Figure 55: Statistical analysis of Meltpool area in terms of # of pixels of Type-I Track 5.

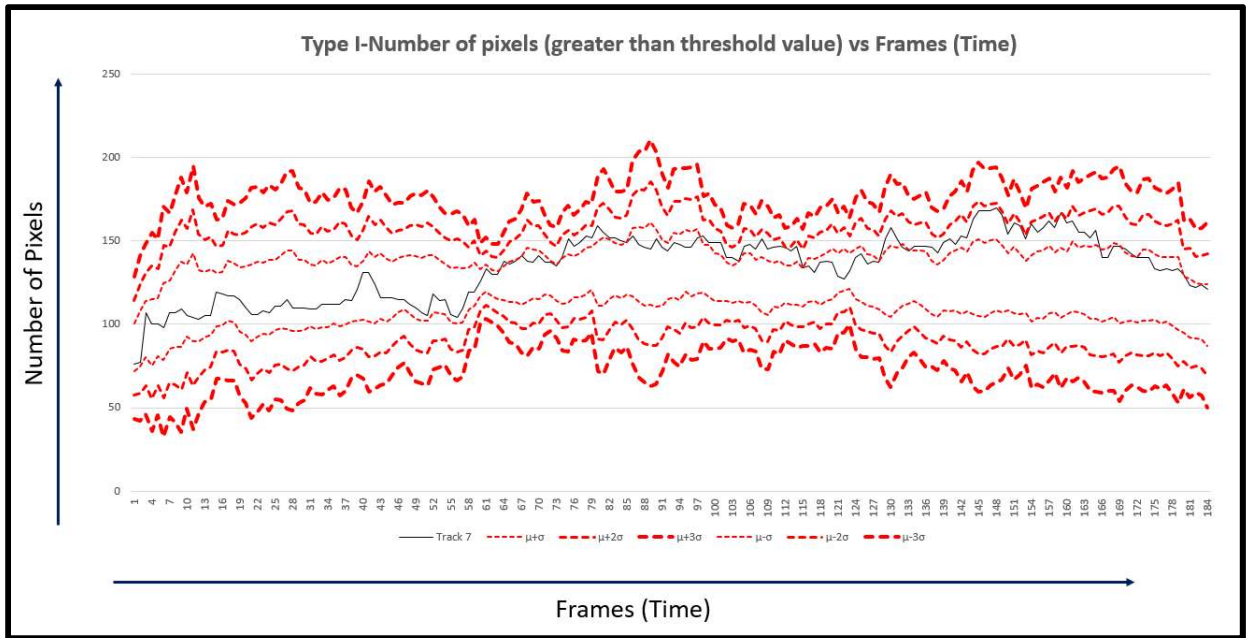


Figure 56: Statistical analysis of Melpool area in terms of # of pixels of Type-I Track 7.

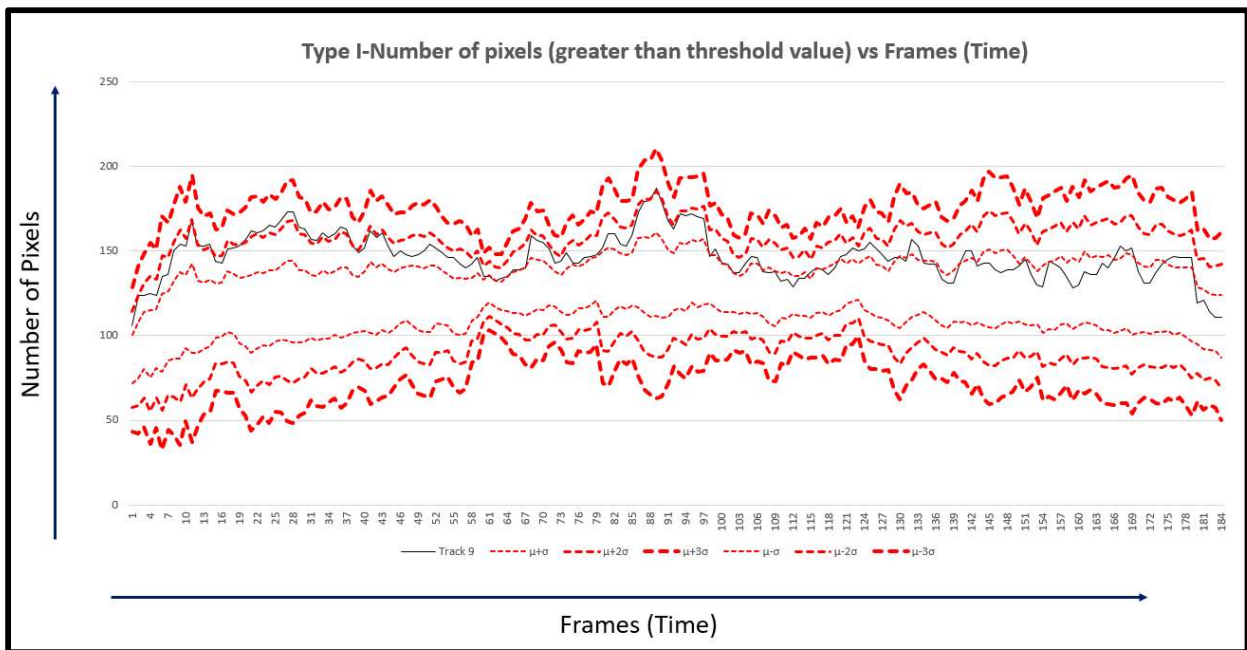


Figure 57: Statistical analysis of Melpool area in terms of # of pixels of Type-I Track 9.

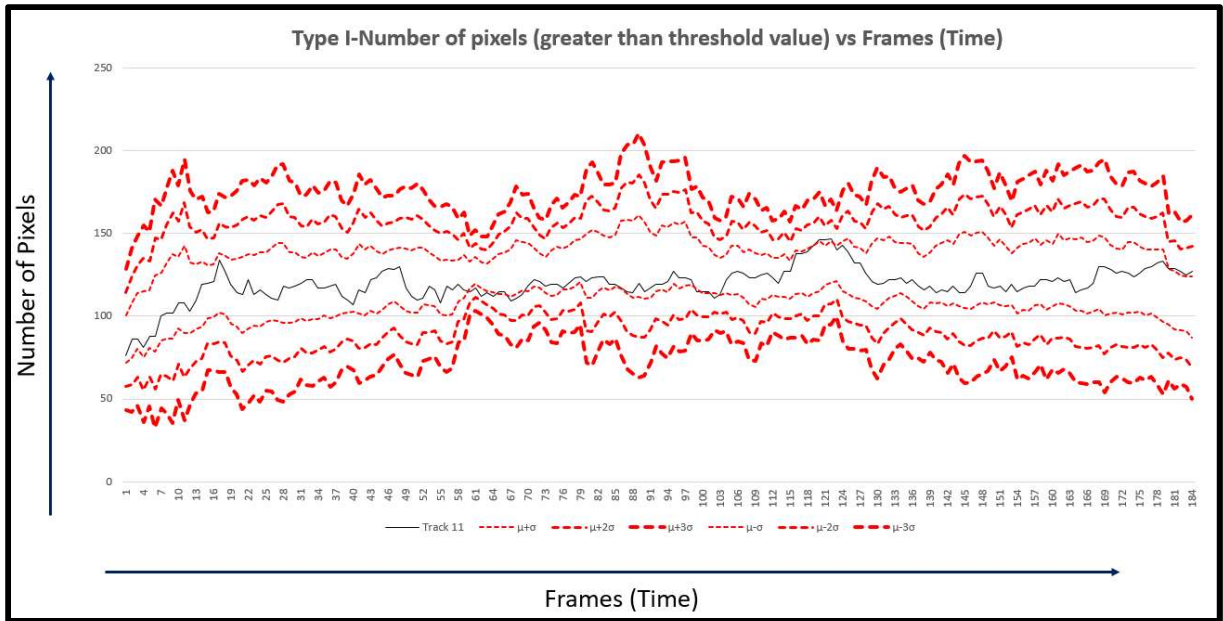


Figure 58: Statistical analysis of Melpool area in terms of # of pixels of Type-I Track 11.

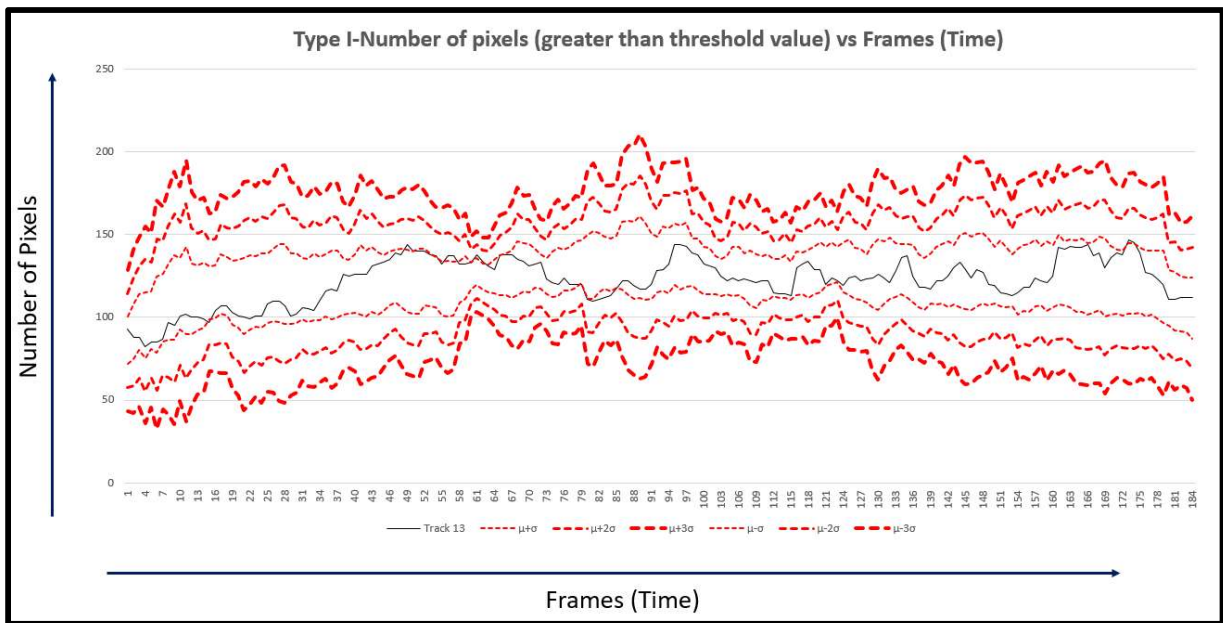


Figure 59: Statistical analysis of Melpool area in terms of # of pixels of Type-I Track 13.

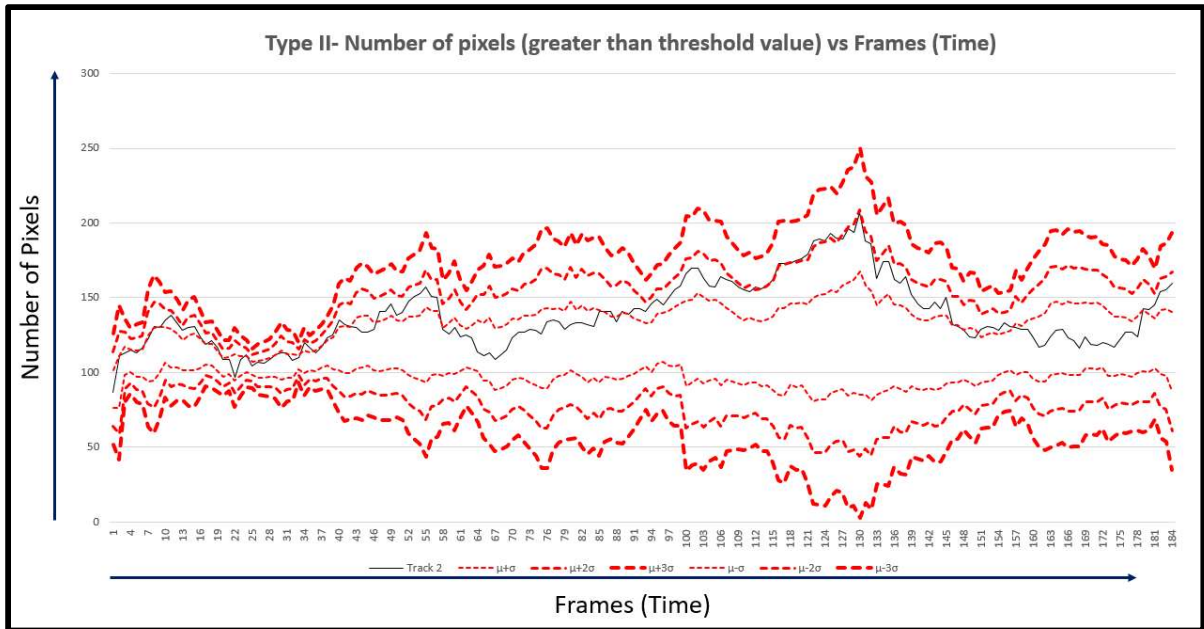


Figure 60: Statistical analysis of Melpool area in terms of # of pixels of Type-II Track 2.

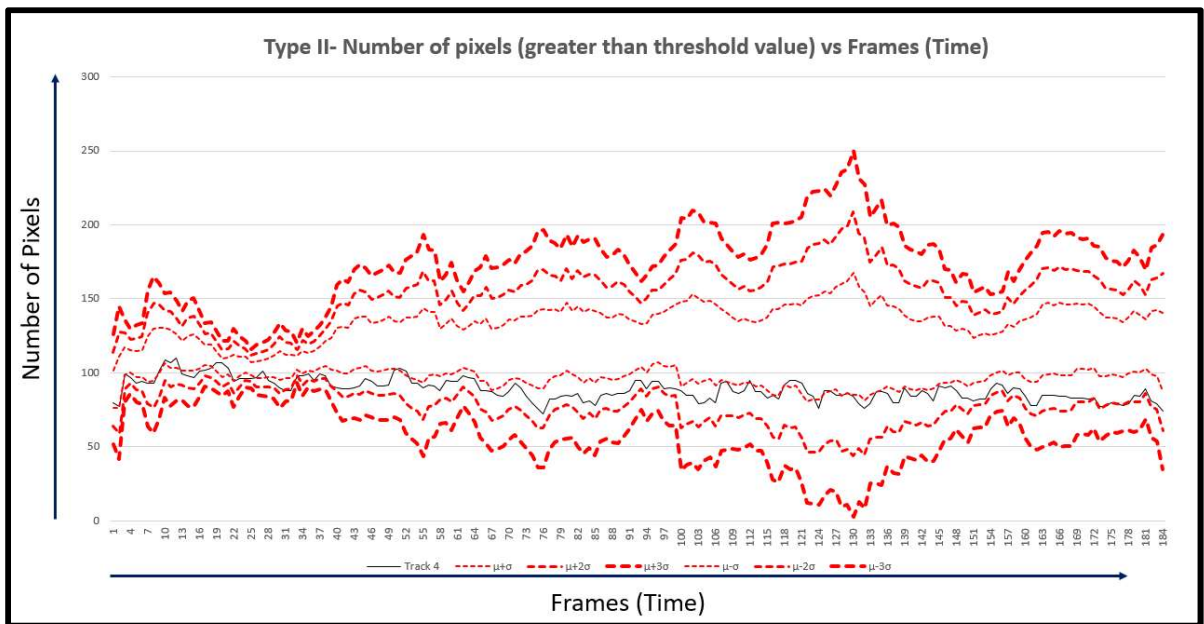


Figure 61: Statistical analysis of Melpool area in terms of # of pixels of Type-II Track 4.

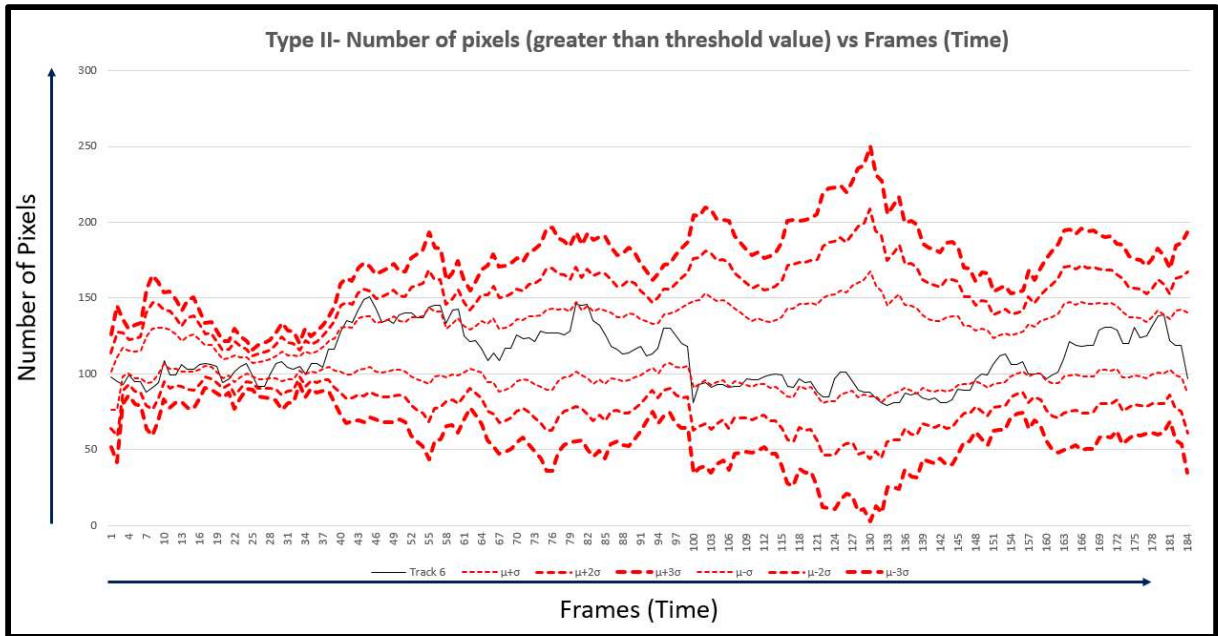


Figure 62: Statistical analysis of Melpool area in terms of # of pixels of Type-II Track 6.

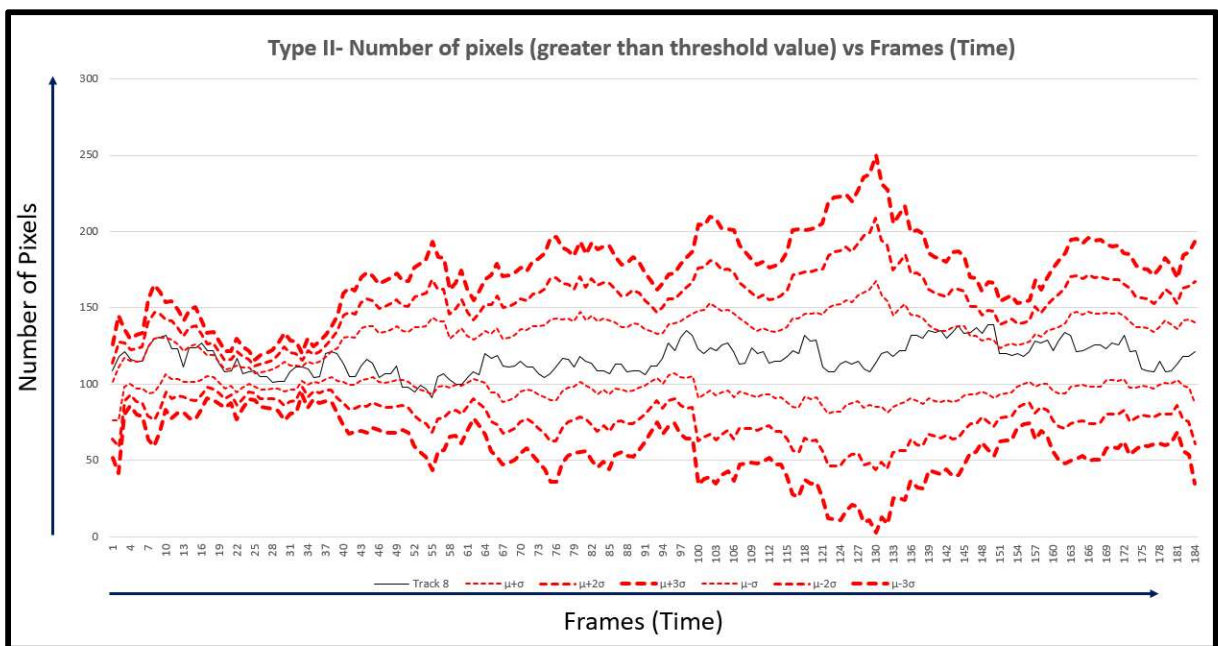


Figure 63: Statistical analysis of Melpool area in terms of # of pixels of Type-II Track 8.

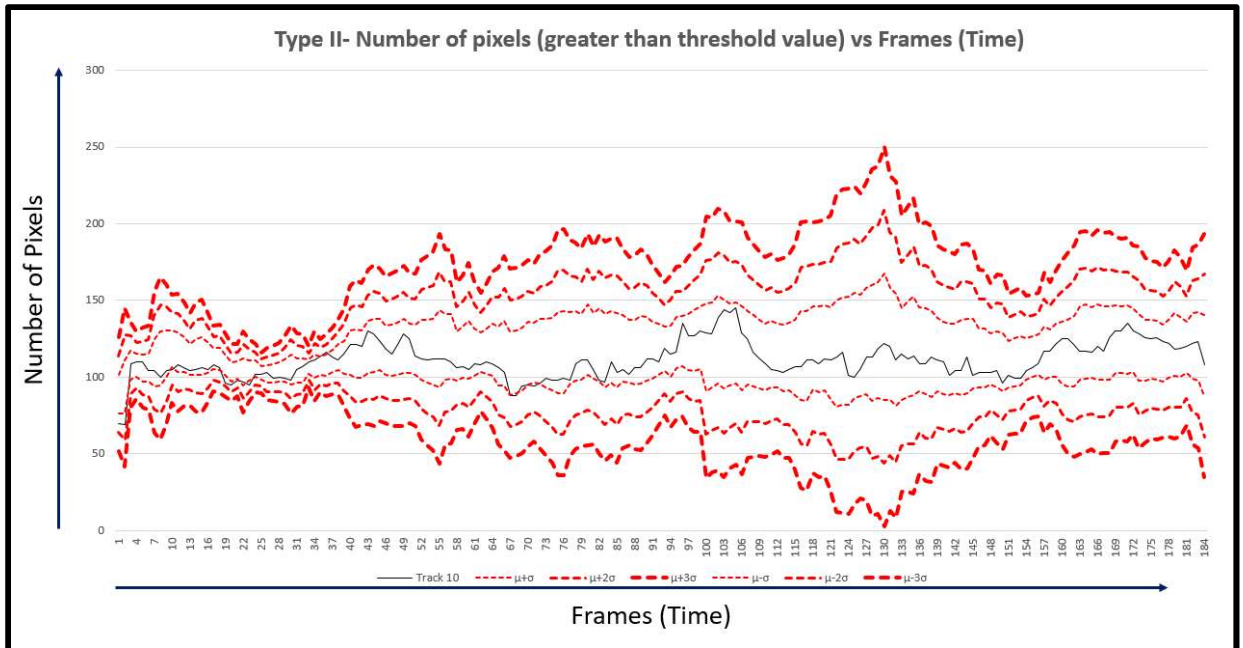


Figure 64: Statistical analysis of Melpool area in terms of # of pixels of Type-II Track 10.

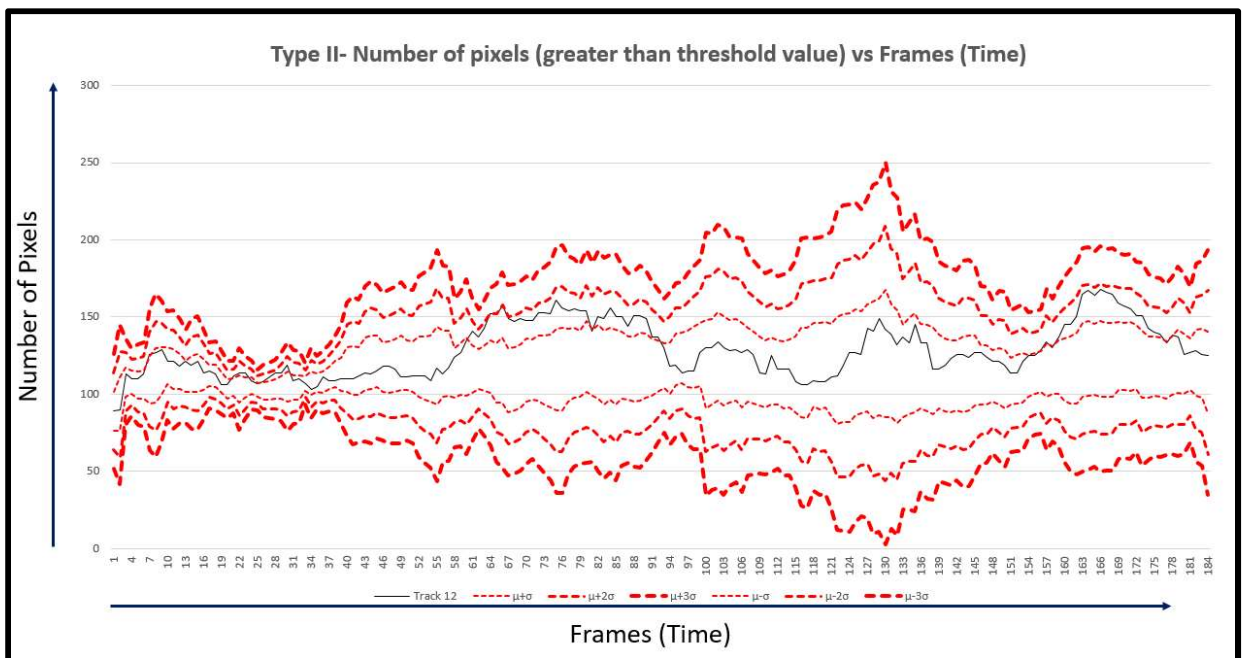


Figure 65: Statistical analysis of Melpool area in terms of # of pixels of Type-II Track 12.

7.3 Spatial Principal Component Analysis

The results of Spatial principal component analysis show that the T^2 descriptor can be represented in the similar domain of image stream i.e. $T^2(X, Y)$, where X and Y denote the pixel location of the individual image. The spatial distribution is performed as VPCA (Vectorized PCA) is applied to the entire image stream of the video files. In our study we considered all principal components contributing to the video to restrict any loss of information but as an alternative it can be limited to only few principal components which contribute most to the video file.

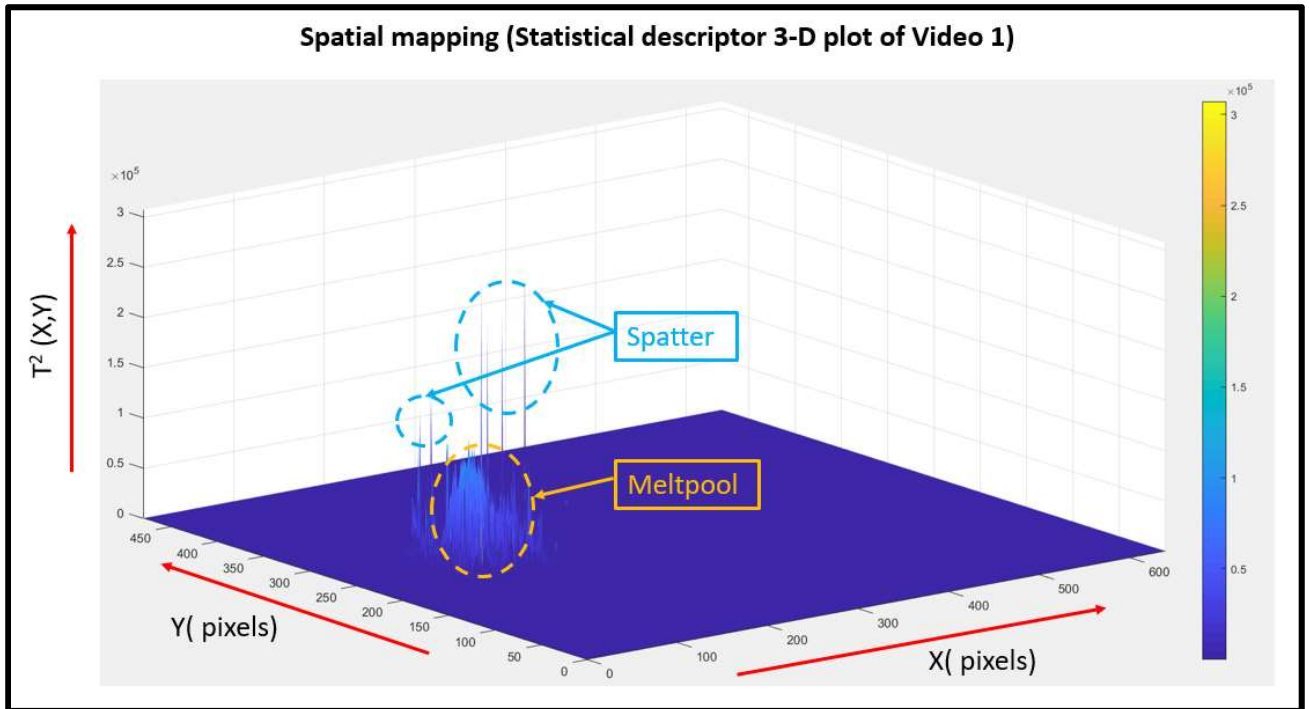


Figure 66: The plot of T^2 values against the pixel location obtained from Video#1.

According to Grasso et al. (2017) higher T^2 statistic value represents over melting phenomenon happening during the L-PBF process. The magnitude of T^2 statistic for Type-I tracks (Fig 67) ranges from 0 to 2.5 whereas for Type-II tracks (Fig 68) it ranges from 0 to 2, which states the fact that over-melting occurs more frequently while processing of Type-I tracks compared to Type-II tracks. Such high values are usually occurring since pixel in these areas are characterized by an intensity profile that is mainly different from the underlying pattern that describes the image stream. The knowledge of spatial localization of these spikes is important from an in-situ perspective, because they can provide information about local anomalies that may result to defects happening in products. In Fig 66 it can be noticed that there are more than one spikes getting formed as the laser moves on from one track to another. These different types of spikes formed during the spatial distribution of $T^2(X, Y)$ can be categorized into 1. Primary spikes and 2. Secondary spikes. Occurrence of more number of secondary spikes along with the primary spikes represents spatter phenomenon happening during the processing. In Fig 67, Type-I tracks show higher number of secondary spikes formed in the spatial distribution of $T^2(X, Y)$ compared to Type-II tracks in Fig 68. This states the fact that spattering defects are more consistent during processing of Type-I tracks rather than Type-II tracks.

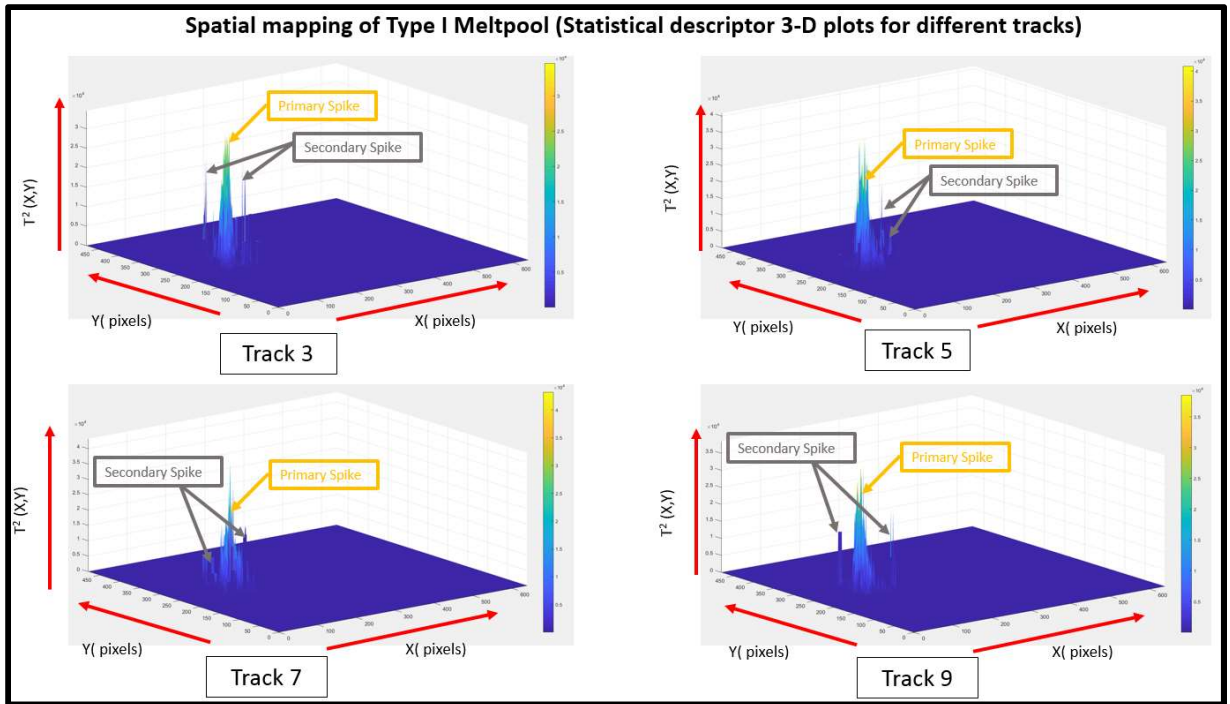


Figure 67: The plot of T^2 values against the pixel location obtained from Type-I melpool for Video #1.

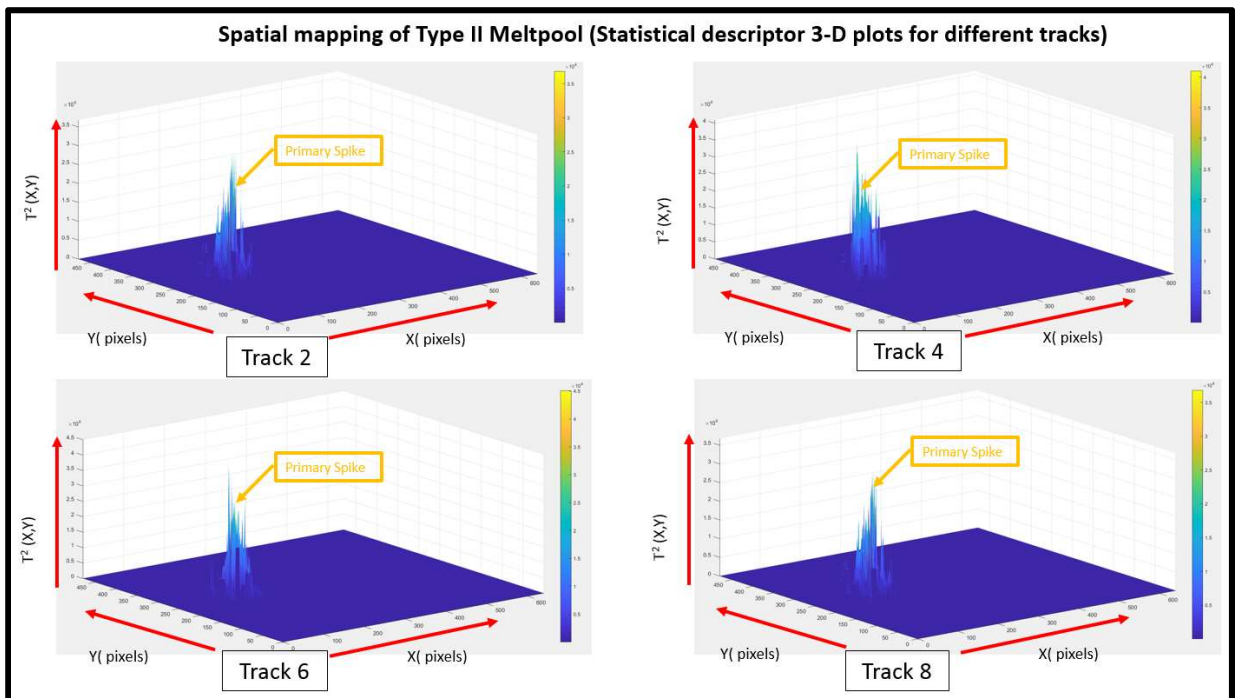


Figure 68: The plot of T^2 values against the pixel location obtained from Type-II melpool for Video #1.

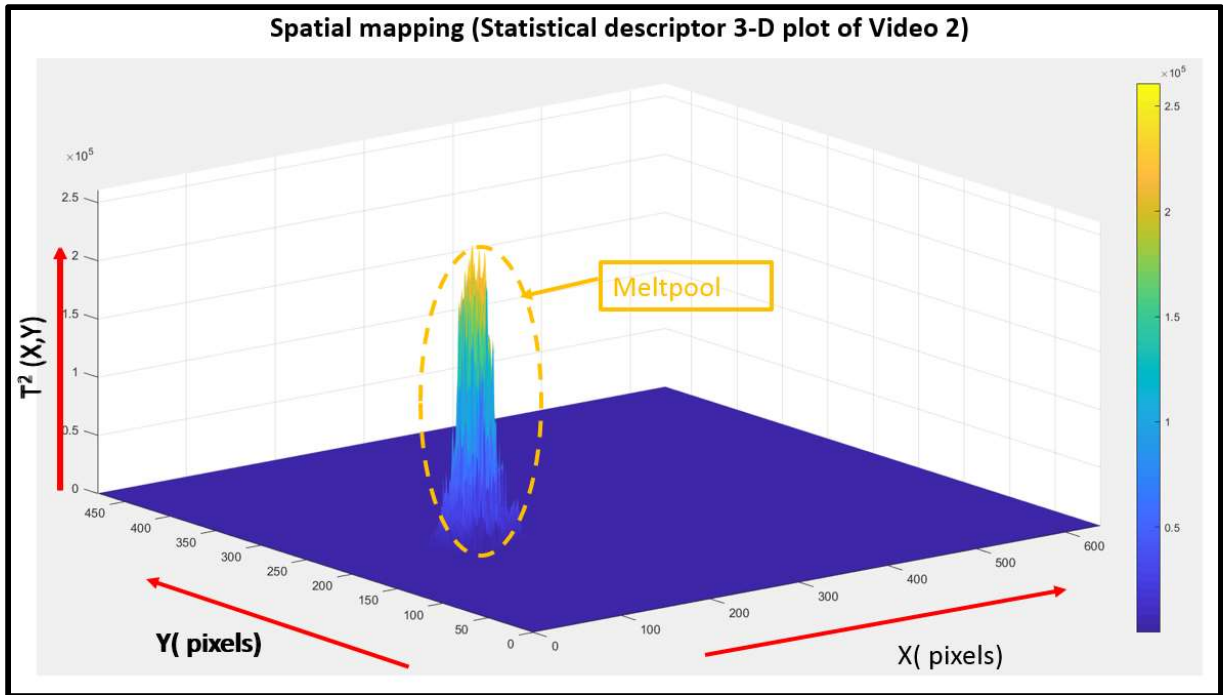


Figure 69: The plot of T^2 values against the pixel location obtained from Video #2.

The results for video #2 follows the same trend as of video #1. Since this video was captured at a higher frame rate per seconds therefore it helps in gathering more data about the in-situ process of laser moving from one track to another. The spatial distribution of $T^2(X, Y)$ in this case gives more detailed 3-D representation of data. The magnitude of T^2 statistic for Type-I tracks in Fig 70 ranges from 0 to 6 and in some cases, e.g. track 8 it goes till 8 also whereas for Type-II tracks Fig 71 it ranges from 0 to 5, which states the fact that over-melting occurs more frequently while processing of Type-I tracks compared to Type-II tracks.

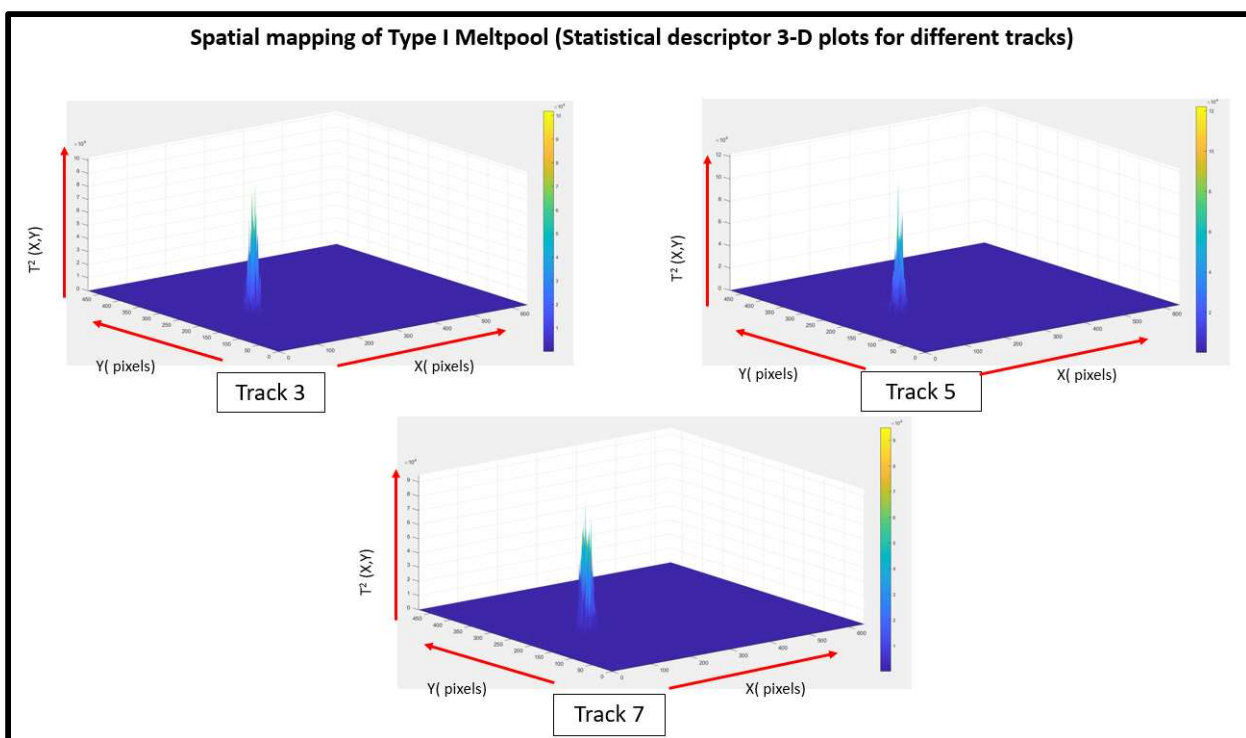


Figure 70: The plot of T^2 values against the pixel location obtained from Type-I melpool for Video #2.

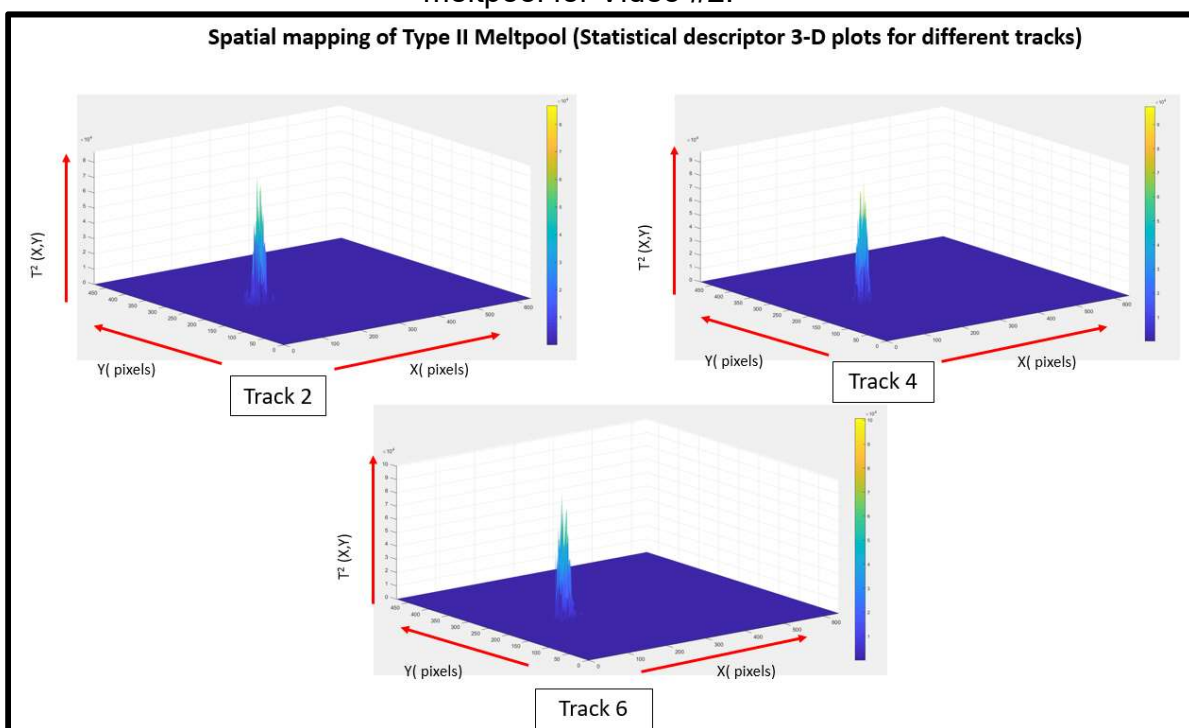


Figure 71: The plot of T^2 values against the pixel location obtained from Type-II melpool for Video #2.

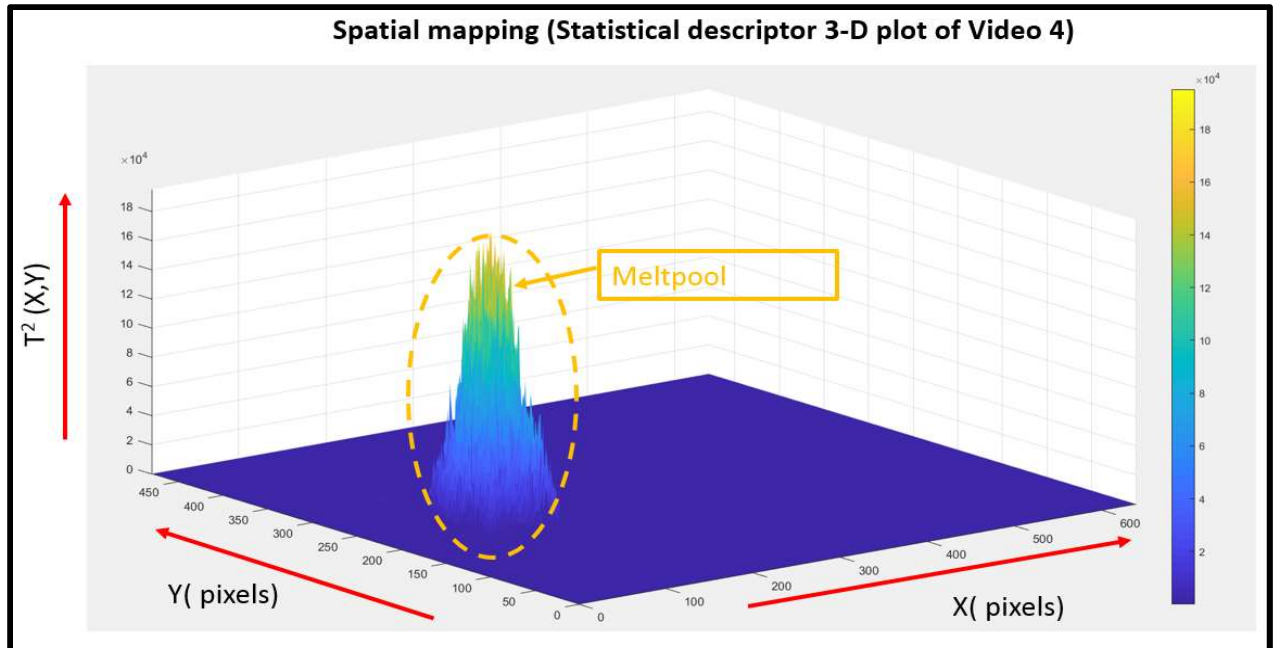


Figure 72: The plot of T^2 values against the pixel location obtained from Video #4.

Video #4 was captured at a zoom condition (X1) and results obtained from its spatial analysis were quite resourceful to identify over melting and spattering phenomenon occurring during the process. The magnitude of T^2 statistic for Type-I tracks Fig 73 ranges from 0 to 4 and in some cases, e.g. track 11 it goes till 5 also whereas for Type-II tracks Fig 74 it ranges from 0 to 3, which states the fact that over-melting occurs more frequently while processing of Type-I tracks compared to Type-II tracks. The number of secondary spikes formed (which are an indicator of spattering phenomenon) are more in Type-I tracks rather than Type-II. The spatial distribution of $T^2(X, Y)$ also states that a higher rate of Frames Per Second and a zoom condition gives more detailed 3-D representation of the process.

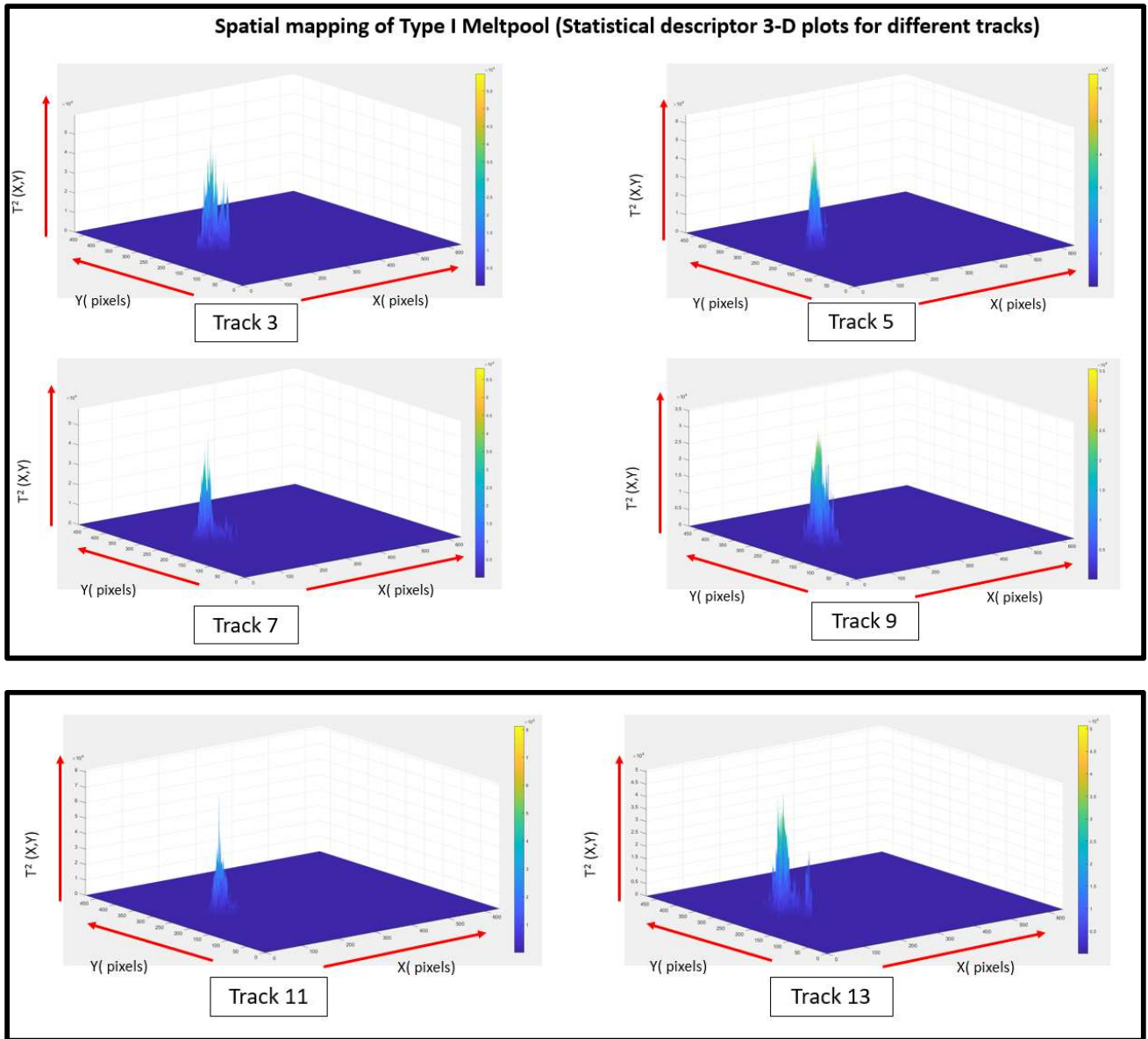


Figure 73: The plot of T^2 values against the pixel location obtained from Type-I meltpool for Video #4.

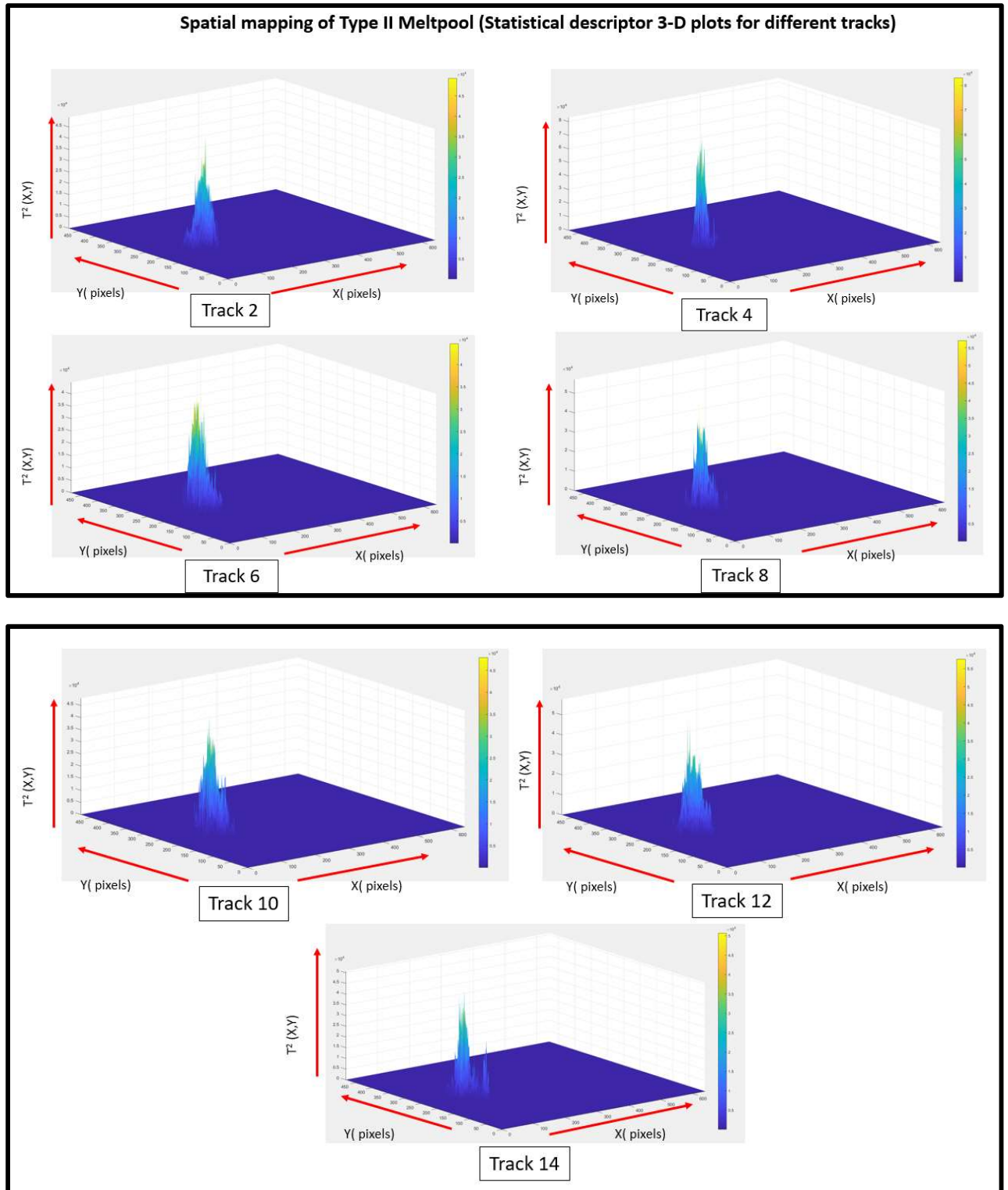


Figure 74: The plot of T^2 values against the pixel location obtained from Type-II meltpool for Video #4.

CHAPTER 8

CONCLUSIONS AND FUTURE SCOPE

8.1 Conclusion

Metal additive manufacturing using L-PBF process and its application fields are tremendously increasing nowadays, and to fulfil its true potential knowledge about process parameters and process signatures and their effects on product quality needs to be researched and studied in detail. Otherwise defects may carry on from initial layers to subsequent affecting the overall quality of the product. The aim and purpose of this study is to capture in-situ videos using a high frame rate camera and to study them to improve process control capability. This study is based upon initial experimental investigation proposed by Criales et al. (2017) in which test coupons were manufactured at National Institute for Standards & Technology (NIST) facility located in Gaithersburg, Maryland, USA.

This thesis presents a method for in-situ monitoring of L-PBF process via using image and video analysis with help of statistical monitoring tools which allows both detection and spatial localization of meltpool and spatter occurring during the process. Also, it includes the study of change in mean gray scale values against time i.e. frames to give an overview of regions categorized on this basis of melting zones.

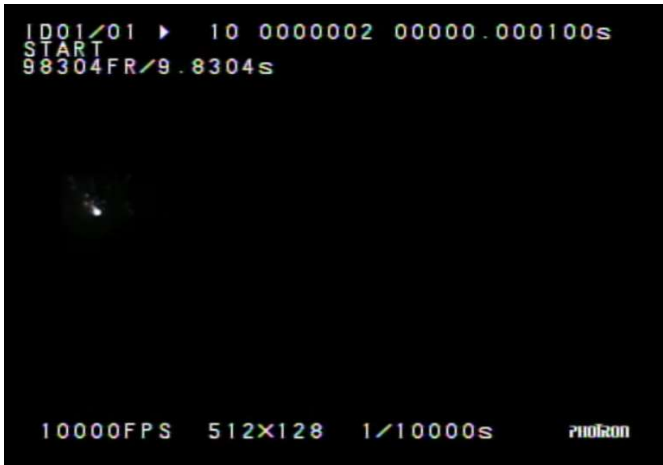


The results obtained from this study proves that the method is more than suitable in developing a self-learning assistance system which can help in detecting spatter as the product is being made layer by layer. Also, the robustness of PCA methodology used in this study can be easily verified by associating it with a statistical descriptor called Hotelling's T^2 distance which gives a spatial mapping against the pixel location using principal components which contribute most towards the video file and restricting loss of the information too.

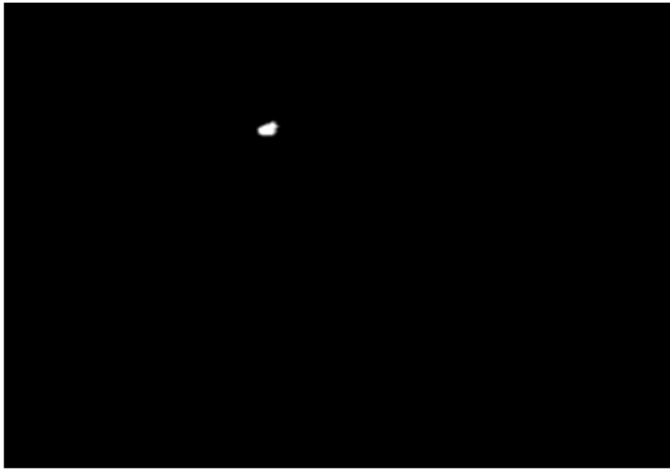


8.2 Future Scope

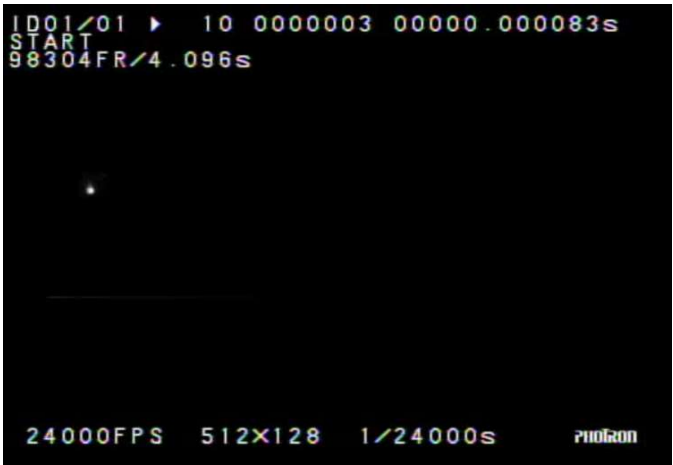

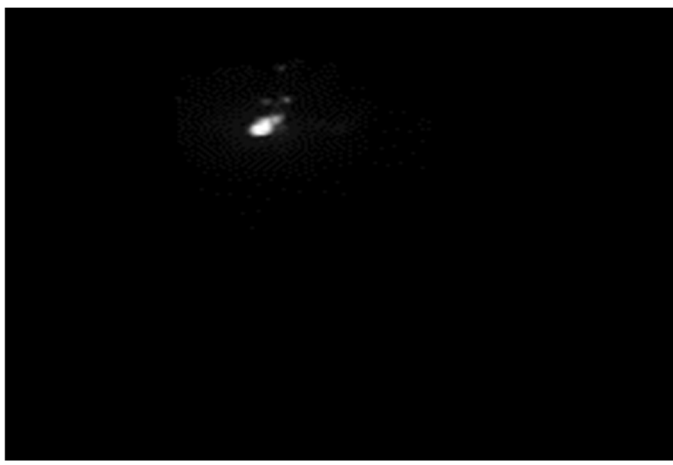
Additional development and research work in future can be directed in field of use of machine learning techniques to run algorithms of spatial mapping automatically as the product is being additively fabricated. It can be equipped with spatial clustering alarm rule which detects defect such as high amount of spatter and over melting phenomenon occurring during the process and alerting the user to reconfigure and change process parameters of the machine to get product without any defects. This technique will also solve the quality related problems which cannot be addressed once the product is completed such as surface finish, relative part density etc. Another important area where research can be conducted is big data stream management to study large video files with higher resolution at a time rather than splitting it smaller files. This way we can easily study all layers being made during L-PBF process at once without any loss of information. In addition to

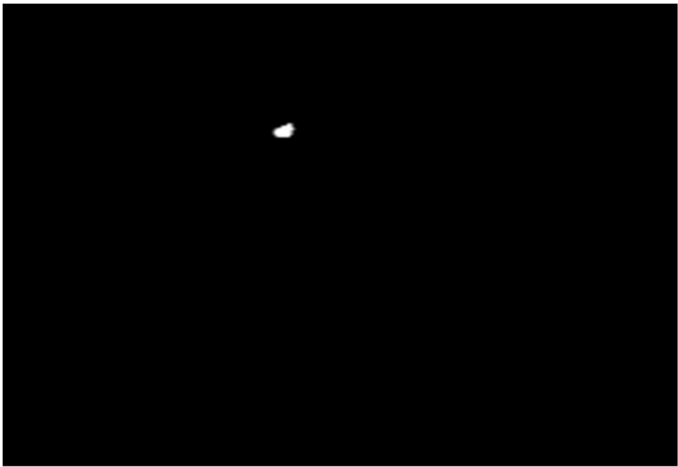
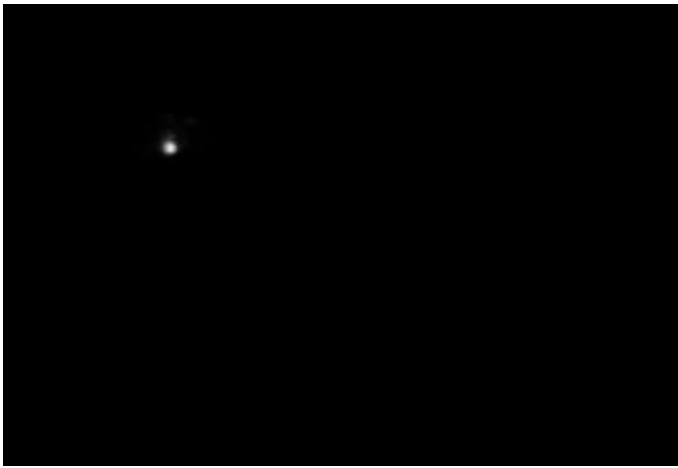
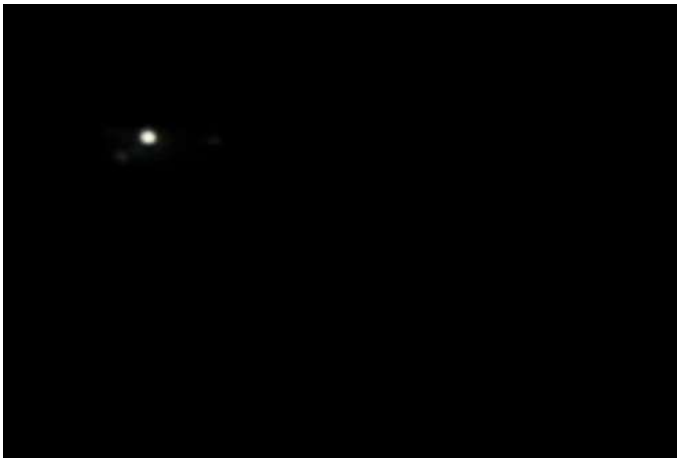
this, research work can be done to study meltpools and their types which are being generated during over melting, normal melting and under melting phenomenon. Meltpool measurements can be obtained using filtering and denoising techniques incorporated with studies done by Criales et al. (2017) and others.

APPENDIX

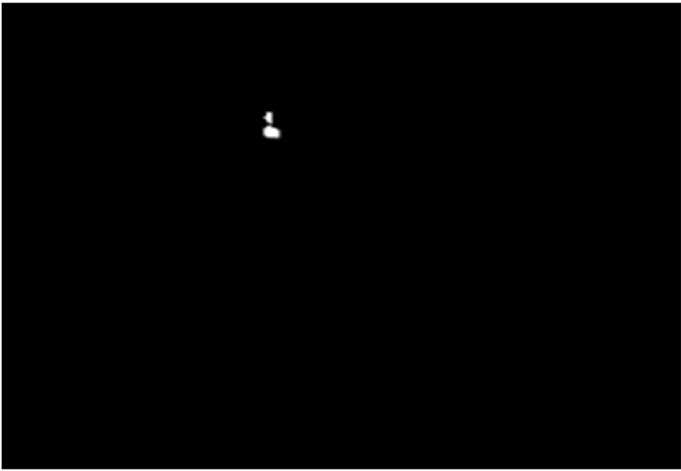

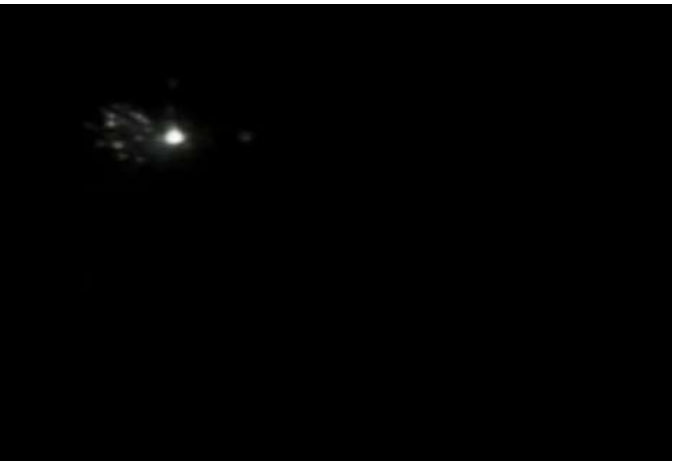
Properties	Image	Status
Video Number: 1. Avi File Size: 2.196 GB Frame rate(FPS): 10000 Resolution: 512 pixels X 128 pixels Integration time: 1/10,000 s Number of Frames: 2232 Duration: 0.2231s Total Frames/Total time: 98304 FR		Unprocessed RGB Image with inbuilt text
		Unprocessed RGB Image without inbuilt text
		Processed Gray Image

		Processed BW Image
		Processed Image of Type I track
		Processed Image of Type II track

Video Number: 2. Avi File Size: 2.32 GB Frame rate(FPS): 24000 Resolution: 512 pixels X 128 pixels Integration time: 1/10,000 s Number of Frames: 2408 Duration: 0.1000292 Total Frames/Total time: 98304 FR		Unprocessed RGB Image with inbuilt text
		Unprocessed RGB Image without inbuilt text
		Processed Gray Image

		Processed BW Image
		Processed Image of Type I track
		Processed Image of Type II track

Video Number: 4. Avi File Size: 3.19 GB Frame rate(FPS): 24000 Resolution: 512 pixels X 128 pixels Integration time: 1/24,000 s Number of Frames: 49869 Duration: 2.077833s Total Frames/Total time: 98304 FR Zoom: X1		Unprocessed RGB Image with inbuilt text
		Unprocessed RGB Image without inbuilt text
		Processed Gray Image

		Processed BW Image
		Processed Image of Type I track
		Processed Image of Type II track

REFERENCES

- Akandea, S.O., Dalgarno, K.W., Munguia, J., Pallari, J. (2016) Statistical Process Control Application to Polymer based SLS process, *Proceedings of the 26th Annual International Solid Freeform Fabrication Symposium*, August 2016, Austin, Texas.
- Colosimo, B. M., Cicorella, P., Pacella, M., Blanco, M. (2014) From profile to surface monitoring: SPC for cylindrical surfaces via Gaussian Processes. *Journal of Quality Technology*, 46 (2): 95.
- Colosimo, B. M., Pacella, M., Senin, N. (2015) Multi sensor data fusion via Gaussian process models for dimensional and geometric verification. *Precision Engineering*, 40: 199-213.
- Colosimo, B.M., Semeraro, Q., Pacella, M. (2008) Statistical process control for geometric specifications: on the monitoring of roundness profiles. *Journal of Quality Technology*, 40 (1): 1-18.
- Criales, L.E., Arisoy, Y.M., Lane, B., Moylan, S., Donmez, A., Özel, T. (2017) Laser Powder Bed Fusion of Nickel Alloy 625: Experimental Investigations of Effects of Process Parameters on Melt Pool Size and Shape with Spatter Analysis, *International Journal of Machine Tools and Manufacture*, 121: 22-36.
- Grasso, M., Colosimo, B. M. (2017) Process defects and in situ monitoring methods in metal powder bed fusion: a review. *Measurement Science and Technology*, 28 (4), 044005.
- Grasso, M., Demir, A. G., Previtali, B., Colosimo, B.M. (2018) In situ monitoring of selective laser melting of zinc powder via infrared imaging of the process plume *Robotics and Computer-Integrated Manufacturing*, 49: 229-239.
- Grasso, M., Laguzza, V., Semeraro, Q., Colosimo, B. M. (2017) In-Process Monitoring of Selective Laser Melting: Spatial Detection of Defects Via Image Data Analysis. *Journal of Manufacturing Science and Engineering*, 139 (5), 051001.
- Kamath, C. (2016) Data mining and statistical inference in selective laser melting, *International. Journal of. Advanced. Manufacturing. Technology*. 85 (5): (2016) 1659–1677.
- Khairallah, S. A., Anderson, A. (2014) Mesoscopic simulation model of selective laser melting of stainless steel powder. *Journal of Materials Processing Technology* 214: 2627–2636, doi:10.1016/j.jmatprotec.2014.06.001 (2014).

Repossini, G., Laguzza, V., Grasso, M., Colosimo, B.M., (2017) On the use of spatter signature for in-situ monitoring of Laser Powder Bed Fusion, *Additive Manufacturing* 16: 35–48.

Özel, T., Altay, A., Donmez, A., Leach, R. (2018) Surface topography investigations on nickel alloy 625 fabricated via laser powder bed fusion. *International Journal of Advanced Manufacturing Technology*, 94 (9–12): 4451–4458.